UiO : Department of Geosciences
University of Oslo

Variability of Lagrangian Coherent Structures in an Ocean Ensemble Prediction System

Mateusz Matuszak

Master's Thesis, Spring 2023

Abstract

Hyperbolic Lagrangian Coherent Structures (LCS) are time-dependent manifolds that organize tracer patterns in chaotic flow systems. In two-dimensional flow systems, LCSs take the shape of one-dimensional curves which act as the locally most attracting or repelling structures over a finite time interval. LCSs yield a description of the flow field itself by defining transport barriers which attract or repel material, without allowing for propagation through them.

Generally, Lagrangian descriptions are prone to large errors and uncertainty due to nonlinear and turbulent oceanic and atmospheric flow fields. Although extensive studies on LCSs have previously been conducted, few studies investigate the implications of this inherent uncertainty in chaotic flow fields on LCSs.

This study investigates the sensitivity of LCSs to uncertainty in the flow field of realistic Oceanic General Circulation Models. Two flow systems are considered: 1) A simplified controlled analytical double-gyre and 2) turbulent velocity data from the Barents-2.5 EPS model, simulating realistic ocean conditions in the Barents Sea and off the coast of northern Norway. The coastal region around the Lofoten-Vesterålen islands in northern Norway is chosen as the study region due to its ecological importance. The Barents-2.5 EPS includes 24 realizations of the same scenario, each with either perturbed initial conditions or forcing that can lead to large differences in the flow field. An ensemble of the double-gyre system is also produced by perturbing the dependent variables.

I develop an LCS detection software utilizing the Finite-Time Lyapunov Exponent approach. The software and resulting LCSs are verified by computing LCSs in both flow systems. I then investigate whether these correspond to independently simulated particle trajectories to study their effect on material transport. Then, LCSs are computed in all ensemble members of the double-gyre ensemble and Barents-2.5 EPS. Following variations in the velocity fields between ensemble members, LCSs vary between ensemble members. Robust LCSs are LCSs predicted by the majority of ensemble members for a particular time. Averaging over ensemble members smooths out the LCSs, but a few clearly distinguishable LCSs are detected in the average, thus these are considered to be highly robust. These are most commonly formed in regions where the current is steered by geomorphological features, which are constant between ensemble members. For the double-gyre system, these include the system boundaries and the separation between the two gyres. For the Barents-2.5 EPS, these features include coastlines and bathymetry.

LCSs are time-dependent and only valid for the time interval they are computed over. Flow structures in the real ocean can form and dissipate quickly, thus LCSs can do so just as quickly. Their persistence, i.e. existence over time, is therefore investigated to study whether LCSs exist long enough to have an influence on nearby material transport. Persistence can change depending on time-scales and has been studied over three time periods in the Barents-2.5 EPS: i) daily, ii) monthly and iii) seasonal.

Daily variations in LCSs are investigated in the straits between islands in the domain. It is known that strong periodic currents form in these straits due to tidal flow. LCSs are revealed to form around these straits and swap east-west positions periodically. This periodicity is shown to be connected to the tidal phase, thus a daily periodic persistence dominated by tides is uncovered.

Monthly persistence has been investigated for April 2022. I find that averaging over time heavily smooths out the LCS field, more than when averaging over ensemble members. This most likely happens because LCSs emerge, drift and decay. As a result, no distinguishable individual curves representing LCSs are detected in the time average. Instead, large high-value regions in the smoothed average reveals locations where LCSs frequently form over the time period. Similarly to robustness, these locations are also primarily dominated by geomorphology. It is also shown that there exists examples of robust features which are not persistent.

To investigate seasonal variations, LCSs from April 2022 were compared to LCSs from October 2022. LCSs are shown to regularly form at different locations in the domain in the two seasons. In April, LCSs are frequently formed along the continental slope and northern and southern tips of Lofoten-Vesterålen. In October, LCSs tend to form along the coastline, whereas few LCSs form on top of the continental slope. This is most likely due to stronger and less topographically-steered currents in October. Furthermore, the main current flows closer to the coast in October, whereas there is an indication of more frequent small-scale flow structures forming and breaking off from the main current in April. Annual variability requires further investigation.

Acknowledgements

I would like to express my deepest appreciation to my supervisor Johannes Röhrs and co-supervisors Pål Erik Isachsen and Martina Idžanović who throughout the years have inspired my interest in oceanography. Thank you for providing me with a topic that I have enjoyed, as well as your guidance, support, expertise and for always being available. This thesis would not have been possible without you and I very much hope I get the opportunity to work with all of you again in the future.

I would also like to extend my sincere thanks to my parents, without whom I would not be the person I am today. Thank you for always supporting and believing in me, as well as for all the dinners you have brought me during my studies. Most importantly, I would like to thank Sunniva for always being there for me.

Contents

List of Figures

1 Introduction

Oceanic and atmospheric flows transport various tracers, such as heat, salt, nutrients, plankton, pollution, volcanic ash and aerosols. The range of dynamical motions can span from centimeters to thousands of kilometers. As water and air moves, these tracers are transported through the Earth system, affecting the climate and ecosystem. Therefore, a good theoretical understanding of the underlying dynamical processes governing fluid transport is important for understanding the role of tracers in the ocean and atmosphere. In addition to process studies, day-to-day forecasting is also dependent on this fluid motion. Thus an improved understanding of dynamical processes will contribute to more accurate forecasts.

Narrowing our focus point to the ocean, there are two common methods used to predict how material propagates through oceanic flow fields. The first method uses a concentration field of a tracer, e.g. heat content, to serve as a "dye" which follows the ocean circulation. The transport and spreading can be studied using an advection-diffusion model, where the velocity field and tracer concentration is discretized on a grid. The time evolution of the tracer concentration is tracked in fixed points in space by solving stochastic differential equations, to e.g. study tracer concentrations in the vertical water column (Roy-Barman and Jeandel, 2016; Nordam et al., 2019). This is the Eulerian method.

The second method is to compute Lagrangian particle trajectories. Material is represented by massless and infinitesimal particles which are placed into a velocity field. Their trajectories are computed by numerically solving ordinary differential equations. These simulate particle propagation and future state based on the particles' initial state, position and the underlying velocity field (van Sebille et al., 2018). This is the Lagrangian method, which described the properties of a specific fluid parcel as it moves and evolves with the flow.

Both the Eulerian and Lagrangian methods require velocity field data. This is commonly obtained from an Oceanic General Circulation Models (OGCM), where the velocity field itself is calculated using the Navier-Stokes equations. Observational-based velocities, such as products of geostrophic currents from satellite altimetry, can be used as well (van Sebille et al., 2018).

Lagrangian particle trajectory integrations have seen a wide use in forecasting drifting material, such as pollution. Furthermore, multiple studies are conducted each year with the intent of tracking natural tracers and particles in ocean water, e.g. larva, jellyfish, fish eggs, icebergs, nutrients and many more (Paris et al., 2005; Dawson et al., 2005; Röhrs et al., 2014; Marsh et al., 2015; Chenillat et al., 2015). Lagrangian analysis of oceanic flow fields is therefore well studied, and is a powerful tool for analyzing ocean velocity data (van Sebille et al., 2018).

However, the ocean and atmosphere are complex dynamical systems, governed by non-linear equations of motion. Calculated velocity fields in OGCMs and Lagrangian trajectory forecasts are therefore highly sensitive to small variations in initial conditions. Small errors in the underlying flow field or initial position of the material of interest can cause large errors in the trajectories over time. An example of the effect uncertainties have on Lagrangian trajectories are shown in Figure 1. If the material of interest is a person or pollutant, quick and accurate transport predictions are imperative to save life or prevent further environmental contamination, but uncertainties can have drastic implications on forecasts. In most extreme cases, the combination of multiple uncertainties can lead to completely different directions of propagation.

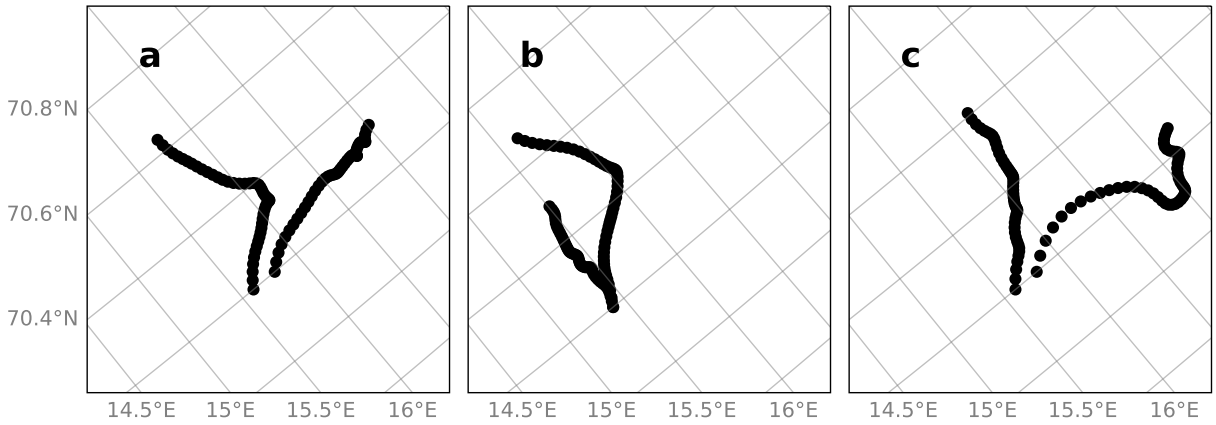

Figure 1: Example of differences in Lagrangian particle trajectories due to a) uncertain release point, b) uncertain velocity field and c) both uncertain release point and velocity field. Particles have been integrated 48 hours forward in time from 2022.11.25 00:00. Velocity data provided by MET Norways Barents-2.5 EPS model, where two ensemble members have been used for the uncertain velocity field. These particles are infinitesimal and massless, so uncertainties in particle properties are excluded. When release point is uncertain, the initial distance between particles is ≈ 7500 m, which corresponds to three grid cells in the model data.

In some cases, the particles initial position and timing of release is known, such as during volcanic eruptions (e.g. the eruption of Eyjafjallajökull located in Iceland in 2010), or spill from oil rigs (e.g. the Deepwater Horizon oil rig accident in the Gulf of Mexico in 2010 (US EPA, 2013)). As the release point is known, errors in initial position and timing can be excluded. Then, only uncertainties in the velocity field and particle properties, such as shape, buoyancy and size, need to be considered. On the contrary, sometimes the initial position and time of material release is unknown. E.g. if a person or shipping containers fall over board from a moving ship, the accidents exact time and location can be uncertain if it is not immediately noticed by the ships crew. Another example is tracking pollution transport, for which origin is unknown.

Uncertainties in the ocean flow fields arise from the fact that OGCMs are inherently limited by a number of factors. Such factors can be grid spacing, unresolved dynamics, parametrizations and computational limitations, although OGCMs are constantly being improved upon (Fox-Kemper et al., 2019). In-situ measurements can provide high quality ocean data, but it is realistically impossible to conduct these measurements on a large enough spatial and temporal scale for it to be applicable in particle trajectory modelling. On the other hand, satellite provide good spatial (although low resolution) and temporal coverage, but they only measure the oceans surface layer due to opaqueness, and cloud coverage can disrupt measurements. Additionally, satellites do not measure velocities directly, so velocities must be inferred from altimetry (Davis et al., 2019), i.e. sea surface tilt, yielding large scale geostrophic currents. Instead, observations provide validation and initial conditions for OGCMs. Even then, observations can include uncertainty due to e.g. human errors during in-situ measurements, missing or limited data, errors instrument calibration or too low instrument accuracy (Parker, 2016). These factors combined lead to uncertainties in oceanic conditions outputted by OGCMs.

A typical method for quantifying uncertainty in ocean flow field and errors in produced forecasts due to their high sensitivity to initial conditions is to run multiple numerical simulations for the same scenario. This is a so called Ensemble Prediction System (EPS), where a group of ocean circulation models are used to account for ocean state uncertainty. Each model in the EPS is referred to as an *ensemble member*. Ensemble members can differ from each other by e.g. having perturbed initial conditions, different atmospheric forcing, methods for resolving ocean dynamics or including different parameterizations. Data from each ensemble member is non-identical, which affects the resulting forecasts for each model (Peacock and Haller, 2013). Relying on results from any single ensemble member is imprecise, as that member might be statistically unlikely (Idžanović et al., 2023). Therefore, predictions are inherently probabilistic.

Even if the chaotic velocity field yields uncertainties in long particle trajectories, it is still common to compute these when analyzing the Lagrangian transport problem. Particularly if we are interested in forecasting where material will end up or where it came from, as well as yielding information about possible propagation paths. However, Lagrangian methods are not restricted to long particle integrations. In recent years a new Lagrangian method has emerged. This method focuses on computing so-called Lagrangian Coherent Structures (LCS). Instead of focusing on material transport over long times, LCSs yield a description of the velocity field and its properties itself.

LCS thus provide a diagnostic tool for analyzing and understanding fluid transport in complex dynamical systems. Proposed by Haller and Yuan (2000), the method aims to identify special time-evolving *manifolds* in unsteady and chaotic flow fields, such as eddies or jets, which shape trajectory patterns around them. Manifolds are geometric shapes in space and take the form of e.g. a curve in one-dimensions (1D) and surfaces in two-dimensions (2D). This study focuses on *hyperbolic* LCSs, where the special manifold tend to *attract* or *repel* nearby fluid elements, thus shaping their trajectories. A central property of hyperbolic LCSs with regards to real life application is that material will converge towards or diverge away from the LCSs, but will never propagate through them. As such, hyperbolic LCSs effectively act as transport barriers. (Haller and Yuan, 2000). See figure 2 for a visualization of attracting or repelling hyperbolic LCSs. Henceforth, "LCSs" refer to *hyperbolic* LCSs.

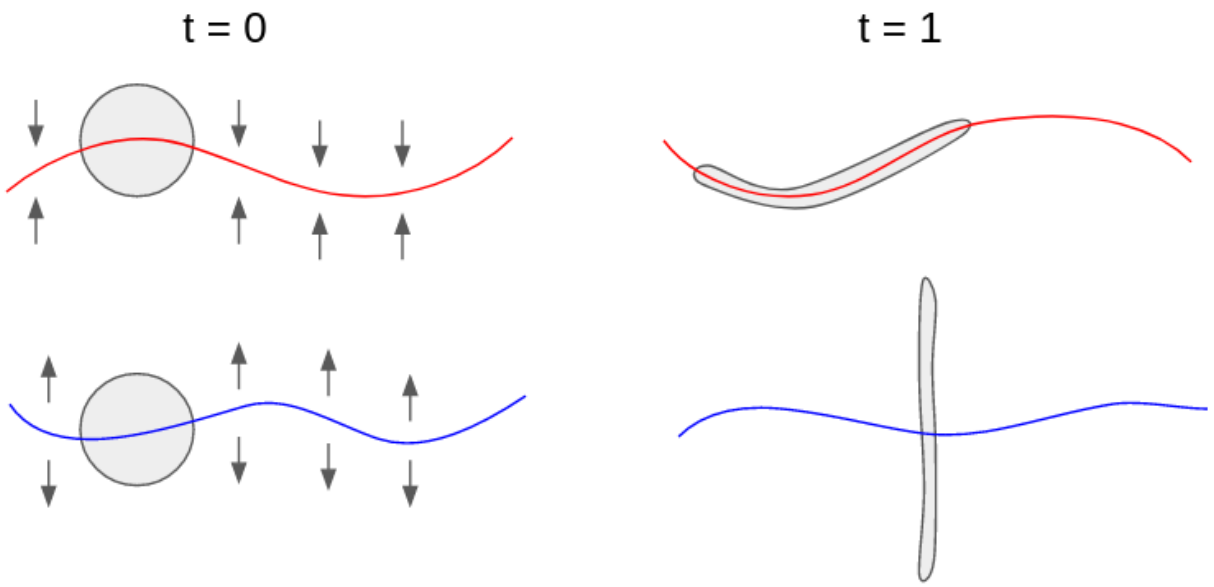

Figure 2: Schematic of attracting (red) and repelling (blue) hyperbolic LCSs. At $t = 0$ a circular blob is placed on each type of flow field. The flow fields are assumed to be 2D and divergentless. Over the time interval $[0, 1]$, the fluid parcel will converge towards the attracting 1D manifold, and diverge away from the repelling 1D manifold. As the fluid elements either converge towards or diverge away from the LCSs, fluid parcel are unable to cross them.

Comprehensive studies on methods to detect LCSs have been conducted, e.g. (Joseph and Legras, 2002; Shadden et al., 2005; Haller, 2011; Karrasch and Haller, 2013), and on the methods sensitivity to factors such as model grid resolution and interpolation schemes (Ghosh et al., 2021). Methods for detecting LCSs typically revolve around integrating a grid of particles over a short time interval and quantifying the separation rate between neighbouring particles. This grid covers the region of interest uniformly, and LCSs are therefore independent of initial particle position (Peacock and Haller, 2013).

Because of the short integrations required, LCSs can be computed using only a small amount of velocity field data. E.g. if only a few satellite snapshots of the velocity field are available, it is possible to compute LCSs to obtain a description of the velocity field for these times. On the other hand, a longer flow field history is necessary to compute long particle trajectories.

However, the LCS description of a velocity field obtained from a few satellite snapshots is only valid for that particular time. LCSs are time-dependent and can only be considered valid for the time interval they are computed over. There is no reason for an LCS computed at one time to exists at a different time (Farazmand and Haller, 2012). As such, LCSs only contain information about potential material accumulation regions in the flow field, as well as transport barriers which shape fluid transport, at a specific time. Information about previous or future states of the velocity field is not directly contained in an LCS. Sometimes, we are only interested in the immediate most probable position of a tracer element, thus its previous or future positions are irrelevant. The tracer elements immediate most probable position can be obtained through LCSs. But if the trajectory is of interest, a long Lagrangian particle integration have to be conducted. Studies of LCSs are studies of flow processes which can affect long trajectories.

In terms of practical applications, LCSs have primarily been used to understand fluid transport. Previous practical studies include Shadden and Taylor (2008) where LCSs are used to

understand blood flow, Dawoodian et al. (2021) where the authors analyze paddling motion of jellyfish, Lekien et al. (2005) that investigates the recirculation of harmful contamination in the ocean released from coastal factories in Florida, and Dong et al. (2021) where the authors investigate a transport barrier defined by LCSs and its effect on nutrient transport near the Lofoten-Vesterålen islands off northern Norway. The studies conducted by Lekien et al. (2005) and Dong et al. (2021) both use LCSs to investigate ocean processes that impact the local ecosystem.

Although LCSs themselves are well studied and have been successful in describing flow characteristics, one important aspect of the topic is yet to be touched upon, namely the *uncertainty* in estimates of LCS. Knowing that the velocity field is uncertain and governed by non-linear dynamics, and that LCSs are inherently dependent on the underlying velocity field, it stands to reason that errors and uncertainties should emerge in LCSs as well. As such, EPSs should be used to quantify LCS uncertainty.

There exist permanent geomorphological features which affect ocean flow, such as boundaries in form of coastlines and bathymetry. Coastlines act as barriers for the currents, and flow has to go along coastlines instead of through them. Large-scale bathymetry steers bottom ocean currents. At higher latitudes, surface and deep waters tend to have similar densities, so the water column is approximately barotropic. As such, large-scale surface currents at high latitudes tend to flow in approximately the same direction as deep water currents, thus surface currents are also steered by large-scale bathymetry (Gille et al., 2004). Such permanent features give rise to more certain and permanent ocean flows which could be reflected in LCSs.

Although velocity fields in an EPS are specifically tailored to vary between ensemble members, the aforementioned geomorphological features impact all model simulations equally. Some similarities in the flow field should therefore arise between ensemble members. Thus, it stands to reason that some LCS features should exists over multiple ensemble members, as well as over time. I use two concepts which will be discussed in this study: *robustness* and *persistence*. Robust LCSs are structures which exists in multiple ensemble members at a certain time, thus giving an indication of the certainty of LCSs at this time. On the other hand, persistent LCSs are structures which exists over a longer time period. Subsequently, identifying if there are any robust or persistent LCSs in turbulent ocean flow, as well as identifying the dynamical causes for these occurrences is key to understanding whether LCSs can be utilized in forecasting.

In addition the geomorphological effects, there are some ocean flow features that are non-chaotic, i.e. very regular. Tides are very *deterministic*, i.e. certain, flow processes that play an important role on the ocean circulation. Tides are caused by the combined gravitational effect of the Moon and Sun on ocean water, for which positions in respect to Earth are known. Its periodicity is therefore highly deterministic and resulting flow features should be highly robust across ensemble members. If the tidal effect is truly similar across ensemble members, it should in turn result in robust LCSs, whereas the periodic nature should cause a periodic persistence in LCSs.

To my knowledge, only a recent study conducted by Badza et al. (2023) attempts to investigate the effect of this inherent uncertainty of the flow field on LCS computations outside of a very simple analytical velocity field. In addition to flow field uncertainty at a given time, new short-lived flow features constantly develop and dissipate in real life ocean flow (Chen and Han, 2019). Given the time-dependency of an LCS, this means that LCSs might

appear and disappear just as quickly. This brings up two important questions: given the velocity field uncertainty, how *confident* can we be in computed LCSs at a particular time? And given their time-dependency, how *persistent* are LCSs in forming transport barriers in ephemeral flows?

In this study, I will investigate LCS sensitivity to variations in velocity fields, and determine their robustness at any given time using an EPS. First, an ensemble of controlled analytical double-gyre systems with perturbed parameters will be used for testing implementations and studying LCSs in a simple system. Secondly, the Barents-2.5 EPS model developed by the Norwegian Meteorological Institute will be employed to study LCSs in turbulent ocean flow fields. The model has a 2.5 km $\times$ 2.5 km horizontal resolution and a hourly temporal resolution. An LCS must be found in multiple ensemble members to be considered robust, whereas persistence over time will be investigated for individual Barents-2.5 ensemble members.

A convergence or divergence of the flow will cause vertical velocities and mixing in the model, thus enabling further vertical transport. This complicates calculations substantially. For simplicity, massless and infinitesimal particles forced to be at the ocean surface will be considered, ignoring the possibility of vertical motion. The LCSs will thus be computed at the ocean surface level. Generally, material with higher buoyancy (or lower density) than ocean water, such as plastic, will stay at the ocean surface, but heavier material can move vertically.

The Lofoten-Vesterålen (LoVe) region has been selected for this study, depicted in Figure 3. This region exhibits a higher nutrient concentration than other regions along the Norwegian coast, resulting in a vast marine biodiversity. As such, this region is a central spot of interest for the Norwegian fishing industry (Sundby et al., 2013). Local LCSs will theoretically influence nutrient transport, given that they exist long enough for them to have an effect. There exists a steep continental slope in the LoVe region, which has large implications of surface currents (Sundby, 1984). Furthermore, the islands act as boundaries for the flow. Both of these geomorphological features are present in the Barents-2.5 EPS, which could yield robustness and persistence. Finding potential robust and persistent LCSs can broaden the understanding of why nutrients tend to gather in this particular region.

Dong et al. (2021) identifies a persistent LCS acting as a transport barrier over the steep continental slope in the LoVe region. This LCS emerged every April between the years 2010-2019 and was present for 49 days on average. The authors used a geostrophic surface current product with a $1/4° \times 1/4°$ horizontal resolution (roughly translating to 25 km $\times$ 25 km), and a six hour temporal resolution. This was produced from satellite altimetry data. Therefore, the interpolated geostrophic currents do no capture small-scale structures or short lived ocean features. Even so, the longevity of the LCS Dong et al. (2021) identified is interesting.

Following Dong et al. (2021), I will focus on the month of April and attempt to identify a similar persistent transport barrier as the authors did for the year 2022. Other possible persistent features will also be considered. Furthermore, I will investigate whether the detected LCSs are robust, given that I use a much more turbulent velocity field with a finer spatial and temporal resolution than Dong et al. (2021), therefore being able to model smaller and less persistent flow features. Additionally, LCSs will be computed for the month of October in the same year, when stratification is stronger and surface currents follow bottom topography to a lesser degree, to study whether there are any seasonal differences.

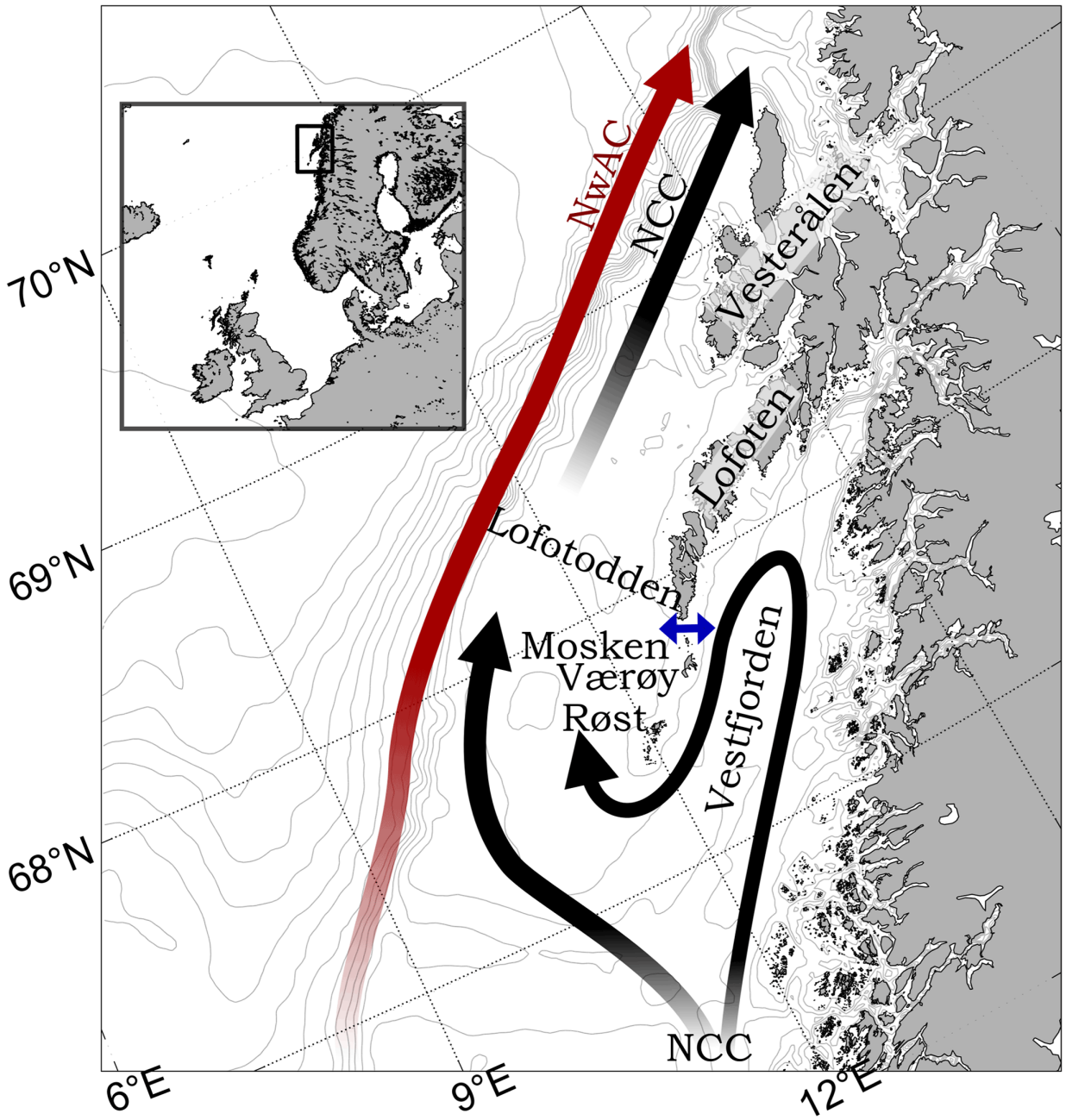

Figure 3: A map over the Lofoten-Vesterålen archipelago with main currents. Both currents come from the south and flow northwards. The Norwegian Atlantic Current is indicated by the red arrow, and flows along the continental slope. The Norwegian Coastal Currents, indicated by black arrows, splits into two south of Vestfjord, with on part flowing into Vestfjord, whereas the second part flows east and then north. Blue two sided arrow indicate the location of Moskstraumen, a strong tide-dependent current flowing through the strait between Lofotodden and Mosken. Figure 1 from Børve et al. (2021).

2 Theory of Lagrangian Coherent Structures and Ensemble Prediction Systems

2.1 Hyperbolic Lagrangian Coherent Structures

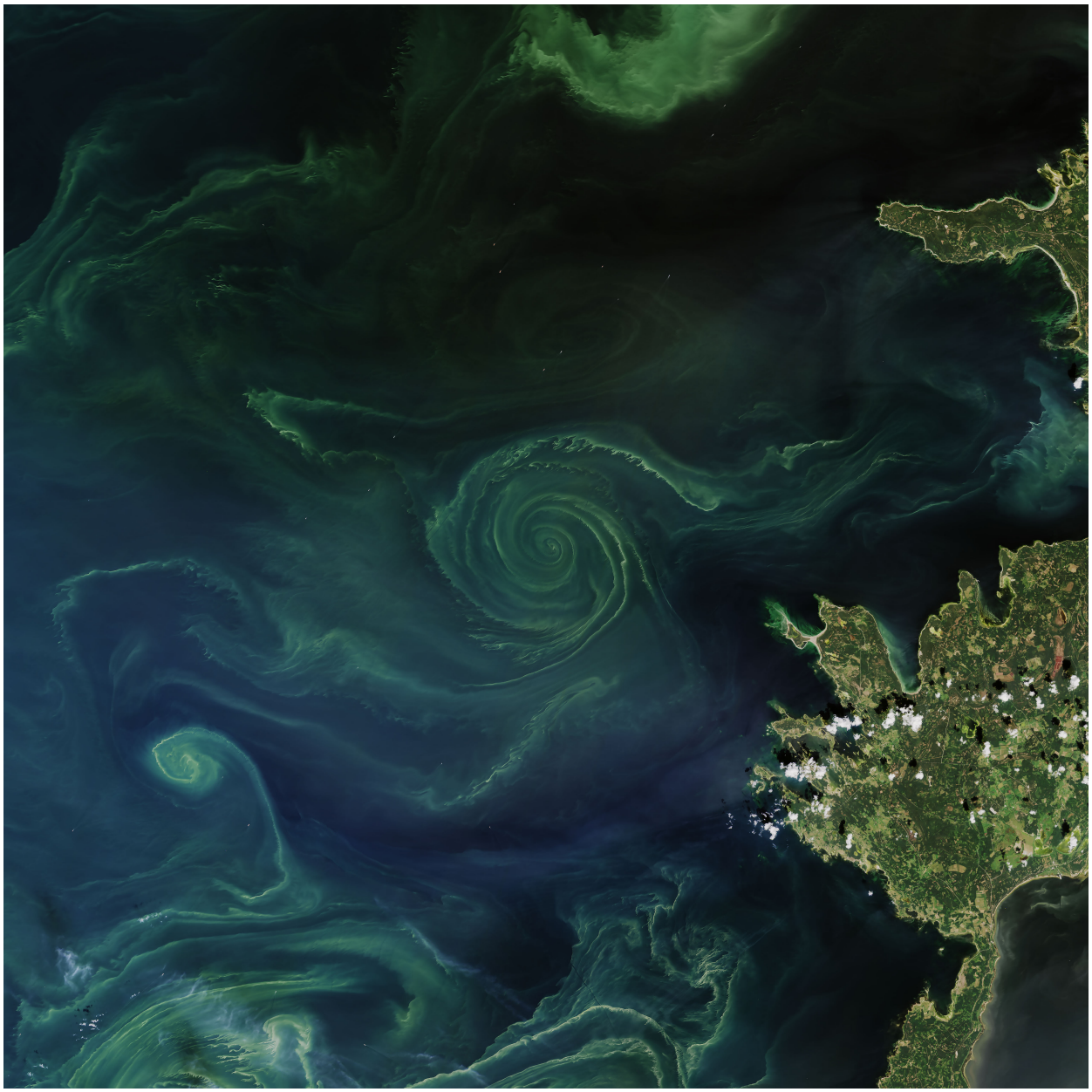

Figure 4: Satellite image of phytoplankton bloom in the Gulf of Finland, July 18, 2018. Image from Stevens and Dauphin (2018).

A satellite image of phytoplankton bloom in the Gulf of Finland is shown in Figure 4. Notice that the phytoplankton pattern takes on a vortex-like shape, with the root cause most likely being an underlying eddy, therefore tracing the edges of this eddy. However, the root cause for such tracer patterns can often be hard to determine. In recent year, the concept of LCS has emerged as a new and effective way to analyze the Lagrangian transport problem. The theory aims to uncover special time-evolving manifolds in such complex dynamical systems,

around which coherent trajectories are formed over a finite time interval (Haller and Yuan, 2000). In other words, the general idea behind LCS theory is to identify manifolds which shape the flow around them, and the impact these structures have on transport. Assuming that we have information about the velocity field at the time the satellite image in figure 4 is taken, LCSs can uncover the root cause for this organized tracer pattern.

2.1.1 Description and deformation of the flow field

The velocity field responsible for shaping tracer patters, such as the phytoplankton seen in Figure 4, can in some situations be approximated to a planar flow field. This is due to vertical velocities essentially being negligible compared to horizontal velocities at larger scales, e.g. for geostrophic flows. Following Haller (2011), this 2D dynamical system can then be defined as

$$\boldsymbol{v}\left(\boldsymbol{x},t\right), \quad \boldsymbol{x}\in U, \quad t\in\left[t_0,t_1\right], \tag{1}$$

where $\boldsymbol{v}\left(\boldsymbol{x},t\right)$ is a smooth, time dependent velocity field defined over a bounded, open domain $U\in\mathbb{R}^2$ over a time interval $[t_0,t_1]$. A velocity field is considered smooth if it is continuous and differentiable everywhere. Given a particles initial position $\boldsymbol{x}_0=(x_0,y_0)$, its trajectory through the dynamical system at time t is denoted by

$$\boldsymbol{x}\left(t,t_0,\boldsymbol{x}_0\right). \tag{2}$$

Using the above equation, a flow map is defined as

$$\boldsymbol{F}_{t_0}^{t}\left(\boldsymbol{x}_0\right)=\boldsymbol{x}\left(t,t_0,\boldsymbol{x_0}\right). \tag{3}$$

$\boldsymbol{F}_{t_0}^{t}\left(\boldsymbol{x}_0\right)$ maps out the flow of a fluid element initially positioned at $\boldsymbol{x}_0=(x_0,y_0)$ at t_0 into its position at a later time t. In other words, $\boldsymbol{F}_{t_0}^{t}\left(\boldsymbol{x}_0\right)$ describes a particles motion between two points in space over a set time interval.

As multiple particles are transported by $\boldsymbol{v}\left(\boldsymbol{x},t\right)$, the distance between neighbouring particles is likely to contract or expand over the time interval. At each point in space, this contraction and expansion of separation between particles can be described by the gradient of the flow map, i.e. the Jacobian of $\boldsymbol{F}_{t_0}^{t}\left(\boldsymbol{x}_0\right)$:

$$\boldsymbol{\nabla}\boldsymbol{F}_{t_0}^{t}\left(\boldsymbol{x}_0\right)=\begin{bmatrix}\frac{\partial x}{\partial x_0} & \frac{\partial x}{\partial y_0}\\ \frac{\partial y}{\partial x_0} & \frac{\partial y}{\partial y_0}\end{bmatrix}, \tag{4}$$

where x and y constitute a fluid elements position at t. Haller (2015) states that, given two neighbouring particles initially separated by an infinitesimal distance $\delta\left(t_0\right)$, the evolution of $\delta\left(t\right)$ over the time interval can be written in terms of Eq. 4:

$$\delta\left(t\right)=\boldsymbol{\nabla}\boldsymbol{F}_{t_0}^{t}\left(\boldsymbol{x}_0\right)\delta\left(t_0\right). \tag{5}$$

Furthermore, the square magnitude of the above equation at t_1 equals to

$$\left|\delta\left(t_1\right)\right|^2=\left\langle\boldsymbol{\nabla}\boldsymbol{F}_{t_0}^{t}\left(\boldsymbol{x}_0\right)\delta\left(t_0\right),\boldsymbol{\nabla}\boldsymbol{F}_{t_0}^{t}\left(\boldsymbol{x}_0\right)\delta\left(t_0\right)\right\rangle=\left\langle\delta\left(t_0\right),\left[\boldsymbol{\nabla}\boldsymbol{F}_{t_0}^{t}\left(\boldsymbol{x}_0\right)\right]^{*}\boldsymbol{\nabla}\boldsymbol{F}_{t_0}^{t}\left(\boldsymbol{x}_0\right)\delta\left(t_0\right)\right\rangle, \tag{6}$$

where $*$ denotes a matrix transposition and $\langle\quad.\quad\rangle$ denotes an inner product in an Euclidean space in $\mathbb{R}^2$, which is given by the dot product, so that

$$\langle\boldsymbol{\alpha},\boldsymbol{\beta}\rangle=\langle(\alpha_1,\alpha_2),(\beta_1,\beta_2)\rangle=\alpha_1\beta_1+\alpha_2\beta_2, \tag{7}$$

where $\boldsymbol{\alpha} = (\alpha_1, \alpha_2)$ and $\boldsymbol{\beta} = (\beta_1, \beta_2)$ are two vectors in $\mathbb{R}^2$. This allows us to employ the Cauchy-Green strain tensor, as defined by Truesdell and Noll (2004)

$$\boldsymbol{C}_{t_0}^{t}(\boldsymbol{x}_0) = \left[\boldsymbol{\nabla}\boldsymbol{F}_{t_0}^{t}(\boldsymbol{x}_0)\right]^{*} \boldsymbol{\nabla}\boldsymbol{F}_{t_0}^{t}(\boldsymbol{x}_0), \tag{8}$$

which describes the speed and direction of deformation. Thus, Eq. 6 can be rewritten as

$$|\delta(t_1)|^2 = \langle \delta(t_0), \boldsymbol{C}_{t_0}^{t}(\boldsymbol{x}_0)\, \delta(t_0) \rangle. \tag{9}$$

$\boldsymbol{C}_{t_0}^{t}(\boldsymbol{x}_0)$ is positive and symmetric. Therefore, two real positive eigenvalues and orthogonal eigenvectors are contained in the tensor, which are related by

$$\boldsymbol{C}_{t_0}^{t}(\boldsymbol{x}_0)\, \boldsymbol{\xi}_i(\boldsymbol{x}_0) = \lambda_i(\boldsymbol{x}_0)\, \boldsymbol{\xi}_i(\boldsymbol{x}_0), \quad |\boldsymbol{\xi}_i(\boldsymbol{x}_0)| = 1, \quad i = 1, 2, \quad 0 < \lambda_1(\boldsymbol{x}_0) \leq \lambda_2(\boldsymbol{x}_0), \tag{10}$$

where λ_i and $\boldsymbol{\xi}_i$ are eigenvalues and eigenvectors of $\boldsymbol{C}_{t_0}^{t}(\boldsymbol{x}_0)$ (Farazmand and Haller, 2012). These notations will be used to define LCSs in the next sections.

2.1.2 Definition of Hyperbolic Lagrangian Coherent Structures

There exist three main types of LCSs: hyperbolic, parabolic and elliptic. Hyperbolic LCSs describe the overall attraction and repulsion in the flow field, whereas parabolic and elliptic LCSs describe trajectories in jets and vortex boundaries, respectively (Haller, 2015). Videos visualizing elliptic and parabolic LCSs can be found in Appendix D. As previous studies regarding practical applications of LCSs primarily focus on hyperbolic LCSs, and the detection method described in 2.1.3 is primarily suited for LCSs, I will focus on these as well.

Hyperbolic LCSs take the shape of $N-1$-dimensional manifolds, where N is the dimension of the considered flow. Manifolds are therefore material lines in 2D flows and material surfaces in three-dimensional (3D) flows (Peacock and Haller, 2013). Focusing on 2D flows, hyperbolic LCSs are described by *material lines*. These are smooth, time-evolving curves, denoted as $\mathcal{M}(t_0)$, which act as locally the most attracting or repelling one-dimensional (1D) manifolds at time t_0. An example of the effect attracting and repelling LCSs have on a fluid parcel can be seen in Figure 2. $\mathcal{M}(t_0)$ evolves over the time interval $t = [t_0, t_1]$ as it is advected by the flow map $\boldsymbol{F}_{t_0}^{t}$, so that $\mathcal{M}(t_0) \rightarrow \mathcal{M}(t_1) = \boldsymbol{F}_{t_0}^{t}(\mathcal{M}(t_0))$ (Farazmand and Haller, 2012), defined in Eq. 3.

One can deduce whether $\mathcal{M}(t_0)$ acts as an attracting or repelling material line over t, as well as the strength of the attraction or repulsion by selecting a normal vector $\boldsymbol{n}_0$ of $\mathcal{M}(t_0)$ with length 1. Similarly to $\mathcal{M}(t_0)$, $\boldsymbol{n}_0$ will also evolve with $\boldsymbol{F}_{t_0}^{t}$. Specifically, we are interested in how the length of the normal component of $\boldsymbol{n}_0$, hereby denoted by $\rho_{t_0}^{t}(\boldsymbol{x}_0, \boldsymbol{n}_0)$, evolves over the time interval. $\rho_{t_0}^{t}(\boldsymbol{x}_0, \boldsymbol{n}_0)$ refers to a normal repulsion or attraction rate of $\mathcal{M}(t)$ along its trajectory. The normal component of $\boldsymbol{n}_0$ selected at any point of $\mathcal{M}(t_0)$ will always have the length of 1. If $\rho_{t_0}^{t}(\boldsymbol{x}_0, \boldsymbol{n}_0) < 1$, the length of the normal component has decreased, thus $\mathcal{M}(t)$ acts as an attracting material line over t. On the other hand, if $\rho_{t_0}^{t}(\boldsymbol{x}_0, \boldsymbol{n}_0) > 1$, the length of the normal component has increased, thus $\mathcal{M}(t)$ acts as a repelling material line (Farazmand and Haller, 2012). The evolution of $\mathcal{M}(t_0)$ and $\boldsymbol{n}_0$ is visualized in Figure 5.

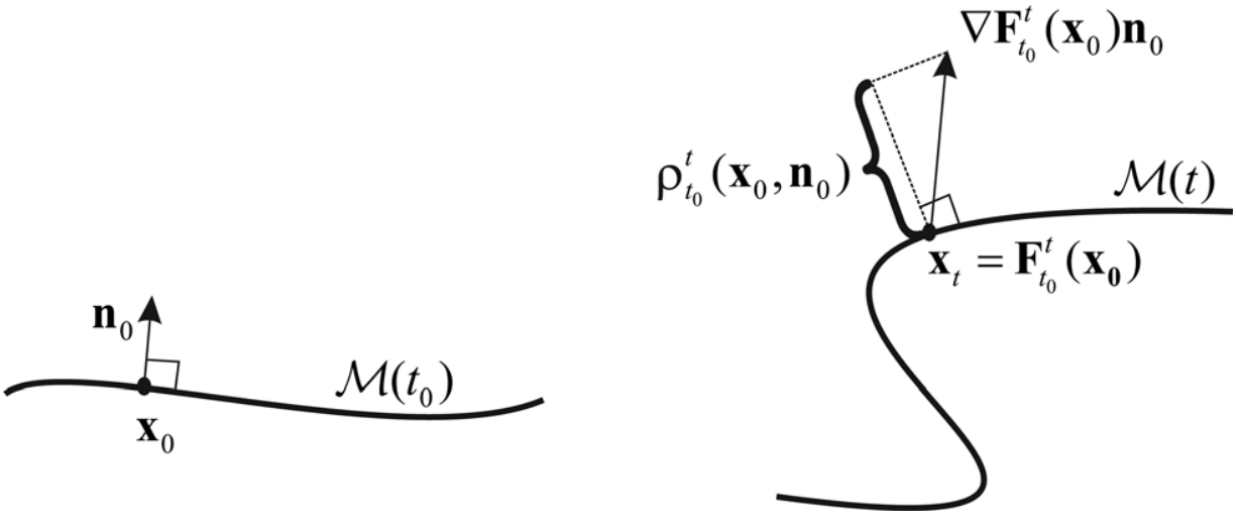

Figure 5: Visualization of the evolution of $\mathcal{M}(t_0)$ and $\boldsymbol{n}_0$ as the system is advected by the flow. A normal vector $\boldsymbol{n}_0$ has been selected at a point $\boldsymbol{x}_0$ on $\mathcal{M}(t_0)$ at time t_0. $\boldsymbol{\nabla} \boldsymbol{F}_{t_0}^{t}(\boldsymbol{x}_0)\,\boldsymbol{n}_0$ shows how $\boldsymbol{n}_0$ has evolved over the time interval, whereas $\rho_{t_0}^{t}(\boldsymbol{x}_0, \boldsymbol{n}_0)$ is the component of $\boldsymbol{\nabla} \boldsymbol{F}_{t_0}^{t}(\boldsymbol{x}_0)\,\boldsymbol{n}_0$ which is perpendicular to the evolved material line $\mathcal{M}(t)$. In this case, $\rho_{t_0}^{t}(\boldsymbol{x}_0, \boldsymbol{n}_0) > 1$, therefore $\mathcal{M}(t)$ is acting as a repelling material line over the time interval. Figure 1 from Farazmand and Haller (2012).

Using the normal repulsion rate $\rho_{t_0}^{t}(\boldsymbol{x}_0, \boldsymbol{n}_0)$, Haller (2011) defines central definitions for LCS. The relevant definitions are cited from their summary in Farazmand and Haller (2012):

"

1. A normally repelling material line over $[t_0, t_1]$ is a compact material line segment $M(t)$ on which normal repulsion rate satisfies

$$\rho_{t_0}^{t_1}(\boldsymbol{x}_0, \boldsymbol{n}_0) > 1, \quad \rho_{t_0}^{t_1}(\boldsymbol{x}_0, \boldsymbol{n}_0) > |\boldsymbol{\nabla} \boldsymbol{F}_{t_0}^{t_1}(\boldsymbol{x}_0)\boldsymbol{e}_0|$$

   for any initial point $\boldsymbol{x}_0 \in \mathcal{M}(t_0)$ and with unit tangent vector $\boldsymbol{e}_0$ to $\mathcal{M}(t_0)$ at $\boldsymbol{x}_0$. The second inequality here requires any possible tangential growth within $M(t)$ to be less than the growth normal to $\mathcal{M}(t)$ over the time interval $[t_0, t_1]$.

2. A repelling LCS over $[t_0, t_1]$ is a normally repelling material line $\mathcal{M}(t)$ whose normal repulsion rate admits pointwise non-degenerate maximum along $\mathcal{M}(t_0)$ among all locally C^{-1}-close material surfaces.

3. An attracting LCS over $[t_0, t_1]$ is defined as a repelling LCS over the backward time interval $[t_1, t_0]$.

4. Finally, a LCS over $[t_0, t_1]$ is a repelling or attracting LCS over the same time interval.

"

Note that the computed LCS is the locally most repelling or attracting LCS over the finite time interval T. However, LCSs are associated *only* with the finite time interval it was computed over. LCS computed for one time interval does not necessarily imply the same LCS over another time interval. This implies that LCSs calculated at one time interval with

known dynamical velocity fields are subject to change over time and can therefore not be used for reliable forecasting at a future or past time when the dynamical velocity fields are unknown. However, as the ocean velocity fields contain multiple features which are persistent over time, for example gyres and surface currents which follow bottom topography, there might exist LCSs which are persistent over time as well.

In 3D flows, computation of 2D material surfaces is required for LCS detection (Peacock and Haller, 2013). Advances have been made in detection of these, as well as their applications, see e.g. Bettencourt et al. (2012) and Blazevski and Haller (2014). However, 2D LCSs are conceptually simpler and I will not consider the 3D case here.

2.1.3 Approximating Lagrangian Coherent Structures with Finite-Time Lyapunov-Exponent

Various methods have been proposed for LCS detection in 2D flows, among which the Finite-Time Lyapunov-Exponent (FTLE) is the most widely used method (van Sebille et al., 2018). This is the method of choice for this study. Other methods include, but are not limited to, Finite-Size Lyapunov-Exponent (FSLE) (Aurell et al., 1997), where time required for the separation to reach a specified distance is considered, and variational LCS detection method (Haller, 2011). However, when it comes to the FSLE, Karrasch and Haller (2013) argue that although this method can give an indication of nearby LCSs, FSLE yield false positives under some conditions, as well as displaying multiple limitations and being less reliable. Therefore, FTLE is more suited for LCS detection. LCSs detected with FSLE and FTLE generally do not coincide (Karrasch and Haller, 2013).

The Lyapunov exponent quantifies the maximum average elongation rate between particles in a system, i.e. the maximum average exponential convergence or divergence of initially closely-located trajectories. This also estimates the instability in a chaotic system (Rosenstein et al., 1993; Dingwell, 2006). For a simple case, consider two points located close to each other in a chaotic system, initially separated by a small distance δ_0. Letting the two points be advected by the background flow will change the separation between them, so after a time t the separation is given by δ_t. In a chaotic system, separation between the two points is assumed to grow exponentially in time, thus δ_t can be approximated as

$$\delta_t \approx \delta_0 e^{\lambda t}, \tag{11}$$

where λ is the Lyapunov exponent, i.e. the separation rate. The reason we refer to the Lyapunov exponent as being the maximum average elongation rate between particles, is that for an n-dimensional system, there are n directions in which the separation evolves, thus also n average Lyapunov exponents. The largest Lyapunov exponent will have the most influence on the shape of the evolved n-dimensional system, therefore the largest Lyapunov exponent is of interest (Rosenstein et al., 1993; Strogatz, 2019).

FTLE is the maximum average expansion/contraction rate for a pair of particles *over a finite time interval*. Pierrehumbert and Yang (1993) considered FTLE as a powerful tool for determining flow properties in a chaotic system. The authors considered a 2D circular disk of tracers, with a small radius r_0 which would evolve in a chaotic flow field over the finite-time interval $t = [t_0, t_1]$. At time t_1, the disk has been compressed in one direction and stretched in another, thus transformed into an elliptic form with major axis $a\,(t)$ and minor axis $b\,(t)$. See Figure 6 for a visualization of the system. As the disk exists in a chaotic system, Pierrehumbert and Yang (1993) made the assumption that the axes will compress

or expand exponentially with time. The length of the major axis after time interval t is then given by

$$a(t) = re^{\lambda t}, \tag{12}$$

where λ is the elongation rate, i.e. the desired FTLE (Pierrehumbert and Yang, 1993). Solving for λ, the elongation rate is given by

$$\lambda = \frac{\ln\left(a(t)/r_0\right)}{t}. \tag{13}$$

Assuming that the fluid is incompressible, the area of the circular disk will not change as it transforms into an ellipse. The area of the circular disk at t_0 is given by $A(t_0) = \pi r_0^2$, whereas the area of the ellipse after time interval t is given by $A(t) = \pi a(t)b(t)$. By the incompressibility assumption, we have that $A(t_0) = A(t_n)$ for any given time t_n, thus $A(t_0) = A(t) = a(t)b(t) = r_0^2$. If Eq. 13 gives the elongation rate, the second exponent, which gives the rate of contraction of the minor axis, will not yield any additional information (Pierrehumbert and Yang, 1993).

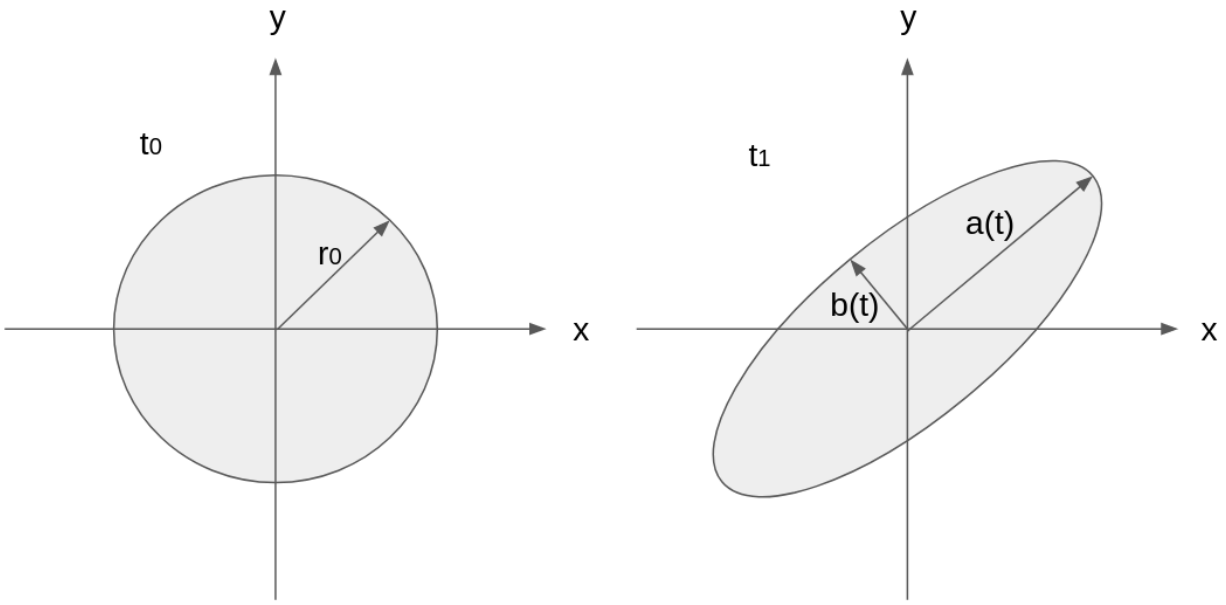

Figure 6: The evolution of an initially circular disk of tracers over the time interval $t = [t_0, t_1]$ located in a chaotic planar flow field. At t_0, the disk is circular with radius r_0. At t_1 the disk has become elongated in one direction and compressed in another, transforming into an elliptic disc. $a\,(t)$ and $b\,(t)$ denotes the major and minor axis respectively.

Using $\boldsymbol{C}_{t_0}^t$ from Eq. 8, FTLE was connected to LCS by Haller (2001), where the author proposed that the ridges of maxima in the FTLE field are LCSs. Further studies on the topic by Shadden et al. (2005) defined LCSs as the ridges of the FTLE field. Ridges refer to special gradient lines of the FTLE field which cross the minimum curvature.

To define LCSs as the ridges of the FTLE field, Shadden et al. (2005) consider again two points, $\boldsymbol{x} = (x, y)$ and $\boldsymbol{y} = (x, y) + \boldsymbol{\delta_0}$, separated by a small distance δ_0 and located in a chaotic flow field. Both of these points are advected by the flow field, where the flow map (Eq. 3) can be used to describe the separation between the two points after a time interval t as

$$\delta_t = \boldsymbol{F}_{t_0}^t(\boldsymbol{y}) - \boldsymbol{F}_{t_0}^t(\boldsymbol{x}) = \frac{d\boldsymbol{F}_{t_0}^t(\boldsymbol{x})}{d\boldsymbol{x}}\delta_0. \tag{14}$$

This also yields information about the stretching experienced by the points. By employing the standard Euclidean norm on the above equation, the size of the separation distance after time interval t can be written as

$$\|\delta_t\| = \sqrt{\langle \delta_0, \frac{d\boldsymbol{F}_{t_0}^t(\boldsymbol{x})^*}{d\boldsymbol{x}} \frac{d\boldsymbol{F}_{t_0}^t(\boldsymbol{x})}{d\boldsymbol{x}} \delta_0 \rangle}, \tag{15}$$

where $*$ denotes matrix transposition and $\langle \quad . \quad \rangle$ is an inner product. Now notice that

$$\frac{d\boldsymbol{F}_{t_0}^t(\boldsymbol{x})^*}{d\boldsymbol{x}} \frac{d\boldsymbol{F}_{t_0}^t(\boldsymbol{x})}{d\boldsymbol{x}} = \left[\boldsymbol{\nabla} \boldsymbol{F}_{t_0}^t(\boldsymbol{x})\right]^* \boldsymbol{\nabla} \boldsymbol{F}_{t_0}^t(\boldsymbol{x}) = \boldsymbol{C}_{t_0}^t(\boldsymbol{x}), \tag{16}$$

i.e. $\boldsymbol{C}_{t_0}^t$ from Eq. 8. Synonym to the previous argument that the largest Lyapunov exponent in an n-dimensional system will have the strongest influence on the stretching in the system, δ_0 is chosen such that it is in alignment with the eigenvector of $\boldsymbol{C}_{t_0}^t$ corresponding to the largest eigenvalues of $\boldsymbol{C}_{t_0}^t$ to find the maximum stretching, so

$$\max_{\delta_0} \|\delta_t\| = \sqrt{\lambda_{max}\left(\boldsymbol{C}_{t_0}^t\right)} \|\overline{\delta_0}\|, \tag{17}$$

where $\lambda_{max}\left(\boldsymbol{C}_{t_0}^t\right)$ is the largest eigenvalue of the $\boldsymbol{C}_{t_0}^t$, and $\overline{\delta_t}$ is in alignment with the eigenvector corresponding to this eigenvalue. Notice that Eq. 17 is similar to the notation for the growth of separation between two particles in a chaotic system from Eq. 11. With this in mind, Eq. 17 can be rewritten as

$$\max_{\delta_0} \|\delta_t\| = e^{\sigma_{t_0}^t(\boldsymbol{x})|t|} \|\overline{\delta_0}\|, \tag{18}$$

where

$$\sigma_{t_0}^t(\boldsymbol{x}) = \frac{1}{|t|} \ln \sqrt{\lambda_{max}\left(\boldsymbol{C}_{t_0}^t\right)} \tag{19}$$

has been substituted in so that Eq. 17 is on the same form as Eq. 11. Similarly to λ from Eq. 11, which was the Lyapunov exponent, $\sigma_{t_0}^t(\boldsymbol{x})$ is now the largest FTLE in the chaotic system over the time-interval t (Shadden et al., 2005). In summary, FTLE is a measure of the maximum average separation rate between two particles over a finite time. Therefore, the FTLE is a measure of repulsion and can thus be used to identify *repelling* LCSs.

The absolute value of the time-interval in Eq. 19 allows for integrations both forwards and backwards in time. Thus, by definitions 2 and 3, the FTLE method allows us to detect both *attracting* and *repelling* LCSs. However, FTLE is just a first approximation of LCSs. 2D LCSs take the form of infinitesimally thin 1D manifolds, whereas FTLE approximate these by regions around said 1D manifolds. Furthermore, Haller (2011) showed that this method can yield both false positives and false negatives, and Beron-Vera et al. (2010) argues that although FTLE has proved to be useful for hyperbolic LCS detection, it is uncertain whether this method can be used for parabolic and elliptic LCS detection.

Haller and Sapsis (2011) points out that attracting LCSs might also be computed from *forward in time* FTLE. The authors show that as ridges, i.e. local maximums, in forward in time FTLE yields an approximation to repelling LCSs, troughs, i.e. local minimums, in forward in time FTLE will yield attracting LCSs. Therefore, only a single integration is necessary to detect both repelling and attracting LCSs. However, this approach is less studied and as such I will use backward in time integrations for attracting LCS detection.

LCS theory is derived from the Lagrangian perspective, with the purpose of analyzing Lagrangian fluid transport. However, the FTLE method itself computes values for the separation rate between particles at each specific model grid cell. Therefore, although the theory originated from a Lagrangian perspective, there is a remapping of the Lagrangian information back to a fixed Eulerian grid. Thus, one could say that the resulting LCSs is a hybrid flow field description.

2.2 Forecasting with an Ensemble Prediction System

When forecasting, current state of the ocean and atmosphere are used as initial conditions, and future states are then simulated using numerical weather models. As the equations of motion governing the ocean (and atmosphere) are non-linear, small errors in initial conditions in this chaotic system can result in large errors in forecast. As we can never truly know the exact initial conditions of the ocean (and atmosphere), due to in-situ measurements not being able to catch every single detail in the oceanic state, as well as errors in observational data, forecasts accuracy and time is limited (Leutbecher, 2007).

The idea behind an ensemble prediction system (EPS) is to quantify the uncertainty caused by non-linearity in forecasts by running multiple numerical ocean and weather model simulations with slightly perturbed initial conditions, different atmospheric forcing, methods for resolving ocean dynamics or including different parameterizations. This results in multiple forecasts, as opposed to running a single simulation. Such a set of forecasts is called an *ensemble* and one forecast withing the ensemble set is called an *ensemble member*. Each ensemble member is initiated at t_0 with initial conditions based on a probabilistic spread, e.g. a Gaussian distribution. This initial spread should be consistent with uncertainty in the model data (Leutbecher, 2007). Idealistically, each ensemble member is equally likely. Assuming that the model is perfect, the ensemble will sample the uncertainty in the forecast.

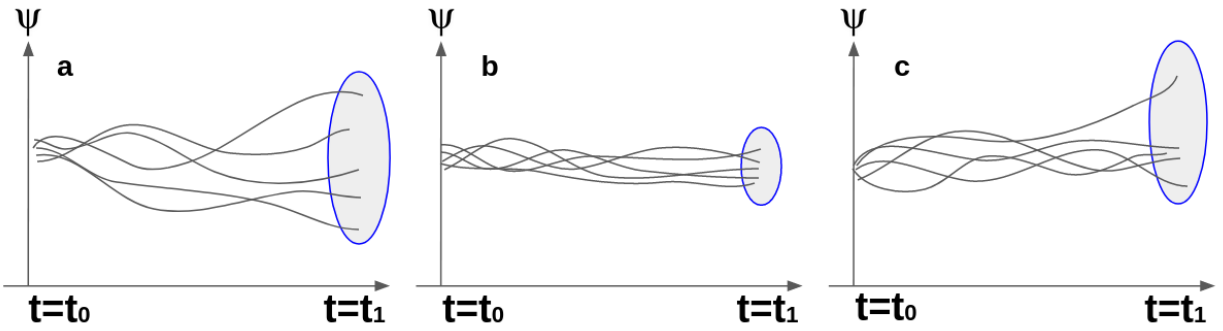

Figure 7: Schematics of the evolution of a deterministic variable ψ over the time interval $t = (t_0, t_1)$ as predicted by en ensemble forecast with 5 ensemble members. a) large spread in the forecast between ensemble members. b) small spread between ensemble members. c) all ensemble members except for 1 predict similar outcomes.

Three schematics of different ensemble forecasts for a deterministic variable ψ are shown in Figure 7. ψ can e.g. be temperature, precipitation or wind-speed. The initial condition of ψ at t_0 is slightly perturbed for the ensemble members and the three panels in the figure depict three different ensemble forecasts for ψ as time t progresses. When forecasting, one would run a statistical analysis of results outputted by the EPS. In Figure 7a, all ensemble

members evolve differently over time, resulting in a large uncertainty in ψ at t_1. In Figure 7b, each ensemble member evolves similarly, which results in a highly certain forecast of ψ. Finally, in Figure 7c, all ensemble members evolve similarly except for one. In situations where one ensemble member differ greatly from all the other, the outcome of that specific ensemble member is considered unlikely. In other words, weather and ocean predictions are inherently probabilistic.

3 Data and Methods

3.1 The Analytical Double-Gyre Model

3.1.1 Double-Gyre Setup

The analytical double-gyre system is commonly used in LCS literature (Shadden et al., 2005). The system will be used to validate my implementations of LCSs, as well as to illustrate the concept of EPS influence on LCSs in a fully controlled analytical system. The resulting LCSs of the system are well studied and known, making it a common testing ground for new theories and implementations. The analytical model for the time-dependent double-gyre system is described in Shadden et al. (2005). The closed system contains two gyres in a domain $x \in [0, 2] \times y \in [0, 1]$, one gyre rotating clockwise and the other counterclockwise. These two gyres then vary periodically, expanding and contracting in the x-direction. The flow in the system can be described as a stream-function

$$\psi(x, y, t) = A \sin(\pi f(x, t)) \sin(\pi y), \tag{20}$$

where

$$f(x, t) = a(t) x^2 + b(t) x, \tag{21}$$

$$a(t) = \epsilon \sin(\omega t), \tag{22}$$

$$b(t) = 1 - 2\epsilon \sin(\omega t). \tag{23}$$

Using the relation that the velocities, u, v are given by $u = -\frac{\partial \psi}{\partial y}$ and $v = \frac{\partial \psi}{\partial x}$, we can write the velocity field as

$$u = -\pi A \sin(\pi f(x)) \cos(\pi y), \tag{24}$$

$$v = \pi A \cos(\pi f(x)) \sin(\pi y) \frac{df}{dx}. \tag{25}$$

Here, ϵ describes the expansion and contraction of the gyres in the x-direction, A determines the rotational velocity, and $\omega/2\pi$ is the frequency of the oscillations (Shadden et al., 2005). Henceforth, the frequency of oscillations will just be noted as ω, dropping the $1/2\pi$ term in the notation, but keeping it in calculations. Note however, that if one would set $\epsilon = 0$, Eqs. 22 and 23 will lose their time-dependent term, i.e. the flow in the system becomes time-independent. An example of the velocity field in the double-gyre system can be seen in Figure 8.

This double-gyre setup is a simplification of double-gyre patterns that occur frequently in geophysical flows, and should not be considered as an approximation to real fluid flows (Coulliette and Wiggins, 2000). The most impactful simplification of the double-gyre setup is that in real fluid flows, flow structures tend to emerge and dissipate over different time-scales, whereas the two gyres in the setup will always be there and no new structures will emerge or disappear.

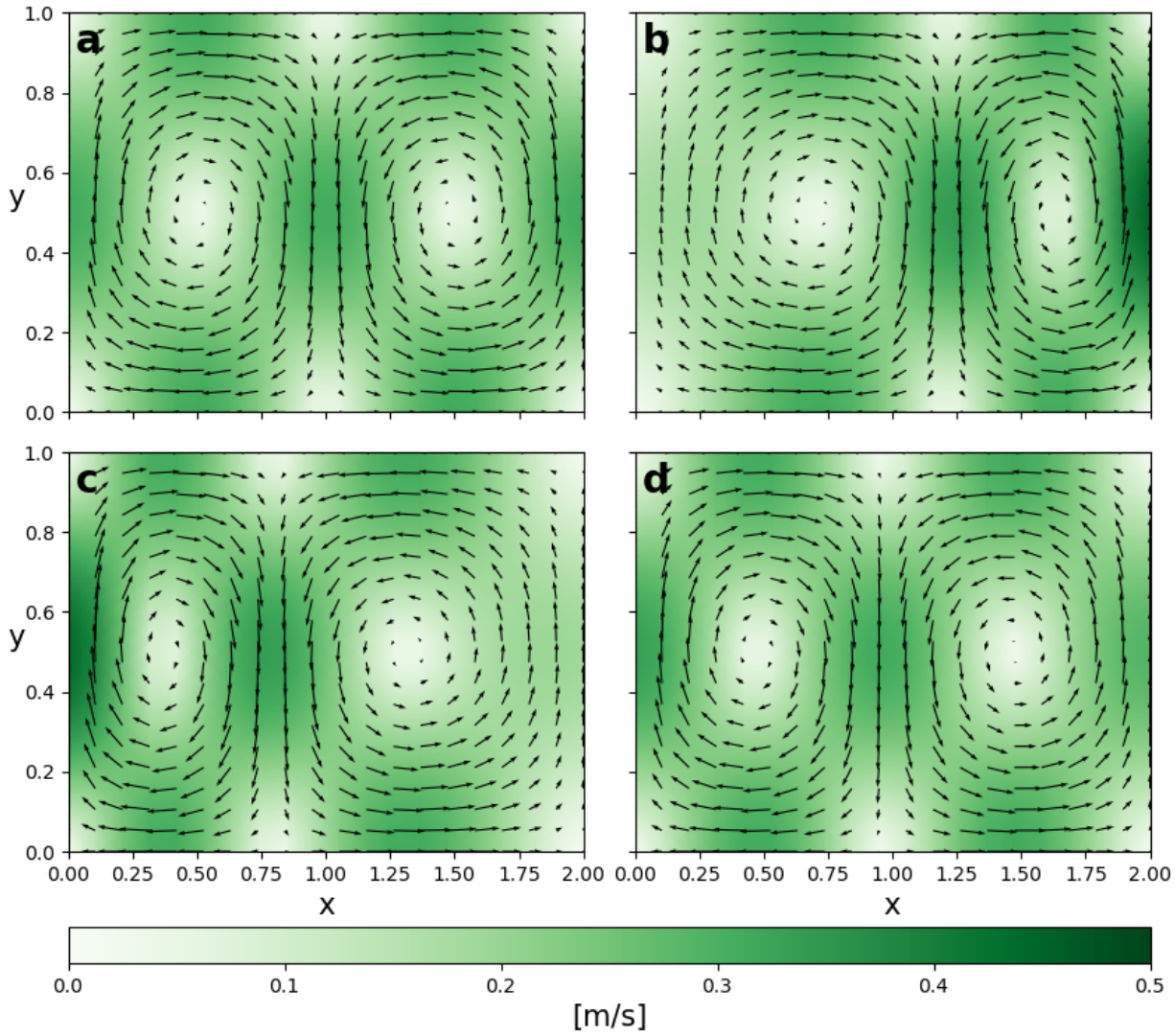

Figure 8: Velocity field in a double-gyre system with parameters $\epsilon = 0.25$, $\omega = 0.682$ and $A = 0.1$ at times: a) $t = 0$, b) $t = 3$, c) $t = 6$ and d) $t = 9$. Direction of flow indicated by black arrows. Strength of the flow indicated by with green.

3.1.2 Ensemble in a Controlled Analytical System

The parameters A, ω and ϵ in the analytical double-gyre system can be perturbed to create an simple analytical ensemble. I will produce a double-gyre ensemble, which will represent an idealized ensemble system. This double-gyre ensemble can then be used to study how LCSs vary depending on small perturbations in the flow, comparing LCS and velocity field sensitivity to parameter perturbations, before applying the LCS detection method to more turbulent velocity fields from a realistic ocean EPS.

The analytical double-gyre ensemble will be initialized with a simple random Gaussian distribution around a specified mean value and standard deviation for the parameters. In this case, the rotational velocity $A = 0.1$ will be kept constant, while the frequency of oscillations ω and the expansion/contraction ϵ will be spread around mean values of $\omega = 0.682$ and $\epsilon = 0.25$, with standard deviations being 0.15 and 0.1 respectively.

Velocity fields from the computed double-gyre ensemble can be compared to each other to get

an indication for how much these fields vary due to small perturbations in the parameters. By using the velocity fields to compute LCSs, we can also get a sense for how sensitive LCSs are to the variations in the flow. This sensitivity can then be compared to the variability of velocity fields between ensemble members, allowing us to investigate whether LCSs show a higher or lower sensitivity to perturbations in the parameters compared to the underlying velocity field. If there are large variations in the LCSs, this approach will also allow us to investigate where in the domain these variations take place, while also yielding information about which parts of the domain stay robust over ensemble members.

3.2 Region of Study

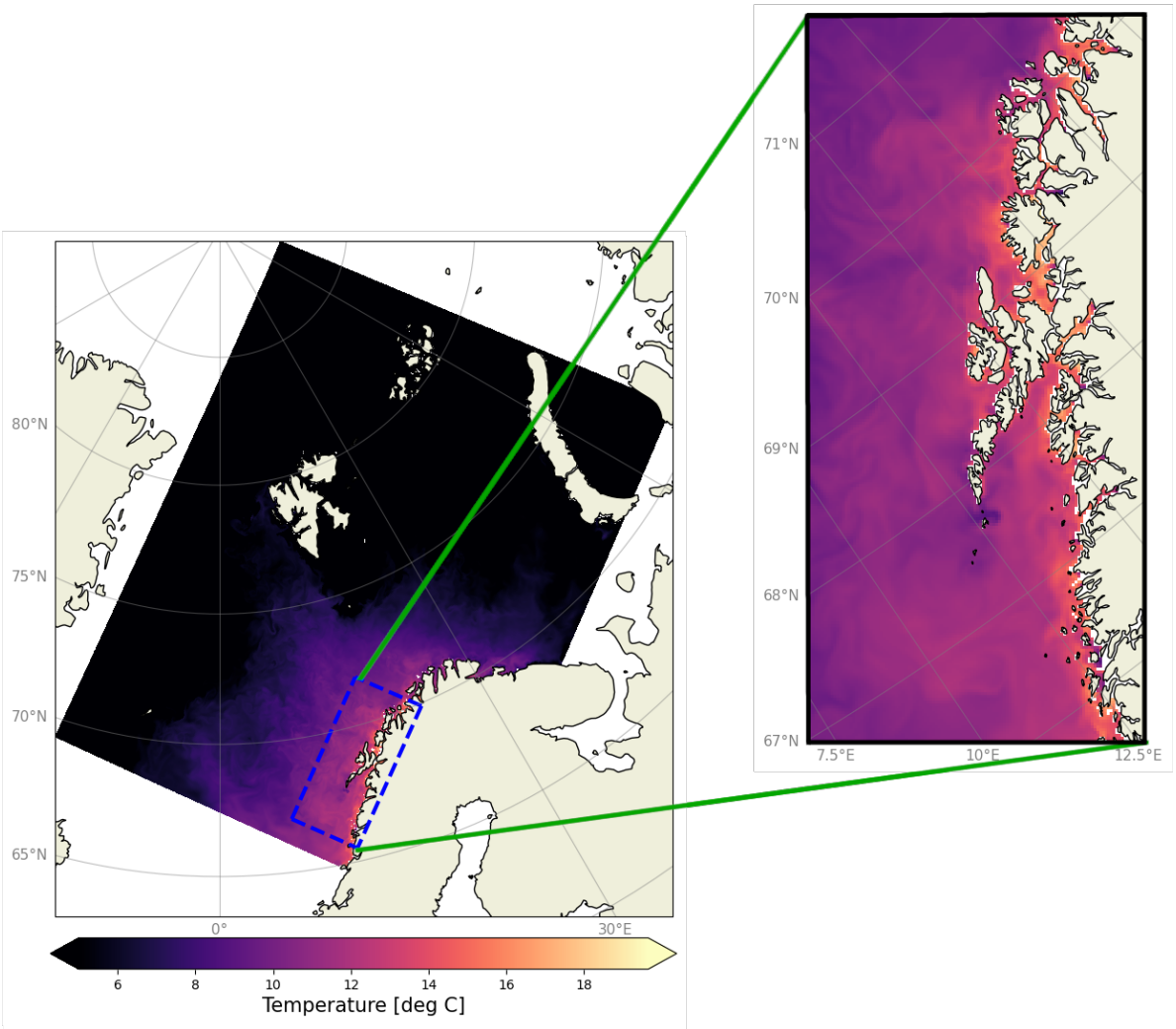

Figure 9: Sea surface temperature [deg C] over the whole Barents-2.5 model domain at time 2022-05-29 00:00. Dashed blue lines highlight the region of interest for this study, which is the oceanic part around the Lofoten-Vesterålen islands, and is enlarged on the right.

The region over which I will investigate LCSs is the coastal ocean around LoVe. This is an archipelago along the coast of northern Norway. In Figure 9, sea surface temperature is used as a proxy to show the Barents-2.5 model domain and the LoVe region is highlighted by

dashed blue lines. This region is well studied due to its vast marine biodiversity, as mentioned in Section 1, including the aforementioned study conducted by Dong et al. (2021).

The LoVe archipelago consist of six major islands: Austvågøy, Vestvågøy, Flakstadøy, Moskenesøy, Værøy, Røst. In addition to multiple smaller islands, these islands constitute a complex coastline which extends far away from the Norwegian mainland. A wide fjord named Vestfjorden is formed in between the LoVe archipelago and the mainland with a wide opening from the south, as seen in Figure 3. This fjord has large implications on the coastal current in the region, causing complex ocean flow features (Mitchelson-Jacob and Sundby, 2001).

There are two main surface currents in the region, the Norwegian Atlantic Slope Current (NwASC) and the Norwegian Coastal Current (NCC), both of which are flowing northwards. These currents are depicted in Figure 3. The NwASC flows along the continental slope, located some distance away from the coastline. This current is connected to the North Atlantic Ocean, from which the NwASC transports warm and saline water northwards (Rossby et al., 2009).

The NCC flows close to the Norwegian coast, and is a low-salinity current due to fresh-water accumulation from river-runoffs along the coast. These fresh water masses are transported by the NCC northwards towards the Arctic Ocean (Gascard et al., 2004). South of Vestfjorden, the NCC branches into two currents. One flows northward into Vestfjorden, whereas the other part flows westward, curving around the southern tip of LoVe, before flowing northward along the coastline again. In winter, southerly winds cause water mass accumulation along the coast. The geostrophic adjustment to the resulting sea surface tilt can lead to increased current velocities during winter (Mitchelson-Jacob and Sundby, 2001).

Large-scale surface currents, such as the NwASC and NCC are heavily influenced by the bottom topography, which is complex in this region (Sundby, 1984; Bosse et al., 2018). As is indicated in Figure 3, both these currents are steered by the bottom topography, which is steepest directly north-west of LoVe.

This particular region of the NwASC and NCC exhibits the most intense eddy-formation and heat-exchange region along the Norwegian coast. An unstable front between the two currents often emerges at the steepest part of the continental slope (Trodahl and Isachsen, 2018). This is caused by instability that emerges from the laterally and vertically sheared currents and steep continental slope (Koszalka et al., 2013; Isachsen, 2015). Eddies formed in the NwASC tend to break off from the current and drift westwards, merging with the Lofoten Basin Eddy (Søiland and Rossby, 2013).

The dynamic and highly deterministic tide generates regular and periodic tidal currents. Narrow straits formed by the archipelagos islands allow for water-mass exchanges between Vestfjorden and the shelf region. These water-mass exchanges are forced by tidal forces. The combination of these tidal forces with strong winds steered by mountains on the archipelago and mainland, as well as the narrowing of the current caused by the straits, can result in strong currents through the narrow straits (Moe et al., 2002). Moskstraumen, indicated in Figure 3 is one of the strongest strait-currents in this region.

3.3 Regional Ocean Ensemble Prediction System

To study the robustness of LCSs and their potential uncertainty due to inherently uncertain velocity fields, we look at the regional Barents-2.5 EPS. Barents-2.5 is a coupled numerical ocean and sea-ice model developed by the Norwegian Meteorological Institute (MET Norway). The model covers the Barents Sea, coast off northern Norway and the oceans around Svalbard (see Figure 9). Barents-2.5 is MET Norway's main ocean and sea-ice forecasting model in this region, used e.g. for tracking marine pollution, sea-ice drift and during search-and-rescue operations. The model is based on the METROMS framework, and incorporates a coupling between ROMS (Regional Ocean Modelling System) as the ocean component and CICE (Los Alamos Sea Ice Model) as the sea-ice component (Fritzner et al., 2018). The model's horizontal grid resolution is 2.5 km. The vertical grid consists of 42 vertical layers which follow bottom topography, a so called s-coordinate system, so that the thickness of each layer varies based on the bottom topography.

Recently, an EPS has been developed based on Barents-2.5. The system consists of 24 ensemble members, divided into 4 sets of 6 members. The sets are initiated with a 6 hour delay, at 00 UTC, 06 UTC, 12 UTC and 18 UTC, with a forecast period of 66 hours. Each ensemble member is initialized by its own state from the previous day in order to preserve sufficient spread in the ensemble. The EPS forecast is initialized with largely varying initial conditions in the mesoscale circulation, as to represent model uncertainties. This ensemble spread is further controlled by the Ensemble Kalman Filter data assimilation scheme, which reduces the spread of observed variables (Evensen, 1994; Röhrs et al., 2023). The first member in each set is forced by most recent atmospheric conditions from the AROME-Arctic model (four ensemble members) (Müller et al., 2017), also developed by MET Norway. AROME-Arctic has the same domain and horizontal resolution as Barents-2.5 EPS, making the two models compatible without the need for any interpolation between the grids (Duarte et al., 2022). The remaining Barents-2.5 ensemble members are forced by 20 ensemble members from the integrated forecast system developed by the European Centre for Medium Range Weather Forecasts (ECWF-ENS) (Röhrs et al., 2023).

Model data files are available on thredds.met.no. Model data from all ensemble members from April and October 2022 has been used in this study. For some days in these two months the EPS does not contain data for all members. A conscious choice has therefore been made to exclude days where some ensemble members are missing when computing LCSs. I will refer to the ensemble members as members 0-23.

3.4 Particle trajectory model

An open-source Python-based framework called OpenDrift (Dagestad et al., 2018), a tool for Lagrangian particle modelling, will be used to model particle advection. OpenDrift is developed by MET Norway, and integrates particle trajectories as the particles are advected by the underlying ocean flow-field:

$$\vec{x}(t) = \vec{x_0} + \int_0^t \vec{v}(x, y, z, t')dt'. \tag{26}$$

OpenDrift allows for the selection of either Euler-Cromer or fourth order Runge-Kutta (RK4) propagation scheme when solving the ordinary differential equations for the particle

positions (Dagestad et al., 2018). RK4 considers the change of flow during a time step, and is therefore more accurate than Euler-Cromer. As such, RK4 will be used for simulating particle propagation with OpenDrift.

Suppose a particle is positioned in the ocean at coordinate $\vec{x}_i$, and we are interested in how the particle propagates over time based on the underlying velocity field. RK4 can be used to numerically calculate the particles position at time t_{i+1}. To do this, a set of equations is used

$$\begin{aligned}
\vec{x}_{i+1} &= \vec{x}_i + \frac{1}{6}\left(k_1 + 2k_2 + 3k_3 + k_4\right) \\
k_1 &= hf\left(t_i, \vec{x}_i\right) \\
k_2 &= hf\left(t_i + \frac{h}{2}, \vec{x}_i + \frac{k_1}{2}\right) \\
k_3 &= hf\left(t_i + h/2, \vec{x}_i + \frac{k2}{2}\right) \\
k_4 &= hf + \left(t_i + h, \vec{x}_i + k_3\right)
\end{aligned} \tag{27}$$

Where h is the step size and f is an arbitrary function which calculates the set of derivatives of $\vec{x}$, so that

$$\frac{d\vec{x}}{dt} = f\left(t, \vec{x}\right) \tag{28}$$

The idea behind the RK4 algorithm is that intermediate steps are being considered. Calculating k_1 yields the slope at t_i, and if one would ignore the remaining k values, the result would be the same as Euler-Cromer. However, the remaining k values yield the slopes at the intermediate steps. The computation of k_2 yields the slope at the midpoint, $\vec{x}_{i+1/2}$, and then by computing k_3, the slope is at $\vec{x}_{i+1/2}$ is improved further. Finally, the slope at $\vec{x}_i$ can be computed using k_4. Due to these intermediate steps, RK4 will be more accurate, although slower, than Euler-Cromer (Hjorth-Jensen, 2015).

3.5 Method for detection of finite-time Lyapunov exponents in a flow field

I develop an LCS detection software utilizing the FTLE approach. A simple step-wise schematic of my software is shown in Figure 10. First, the software places particles in a uniform, equidistant grid in a velocity field. The grid resolution matter. Small-scale structures will not be detected with a low resolution. A high resolution will factor in chaos in small-scale structures which might affect the outcome, at the cost of increasing the computational time significantly. Furthermore, as the Barents-2.5 EPS model has a resolution of 2.5 km $\times$ 2.5 km, computing FTLE fields at a very high resolution, e.g. 100 m $\times$ 100 m, is not expedient. However, having a somewhat higher resolution than Barents-2.5 EPS is still possible by interpolating between the Barents-2.5 EPS grid cells. OpenDrift includes a function for linear interpolation between the grid cells (Dagestad et al., 2018). For this reason, I chose to have a resolution of 1000 m $\times$ 1000 m in the computed FTLE fields.

After placing a grid of particles into the velocity field, the next step is to integrate these particles backwards in time over a set time-interval as per definition 3 in Section 2.1.2. Step 1 in Figure 10 is a backward in time integration from $t = 1$ to $t = 0$, corresponding to

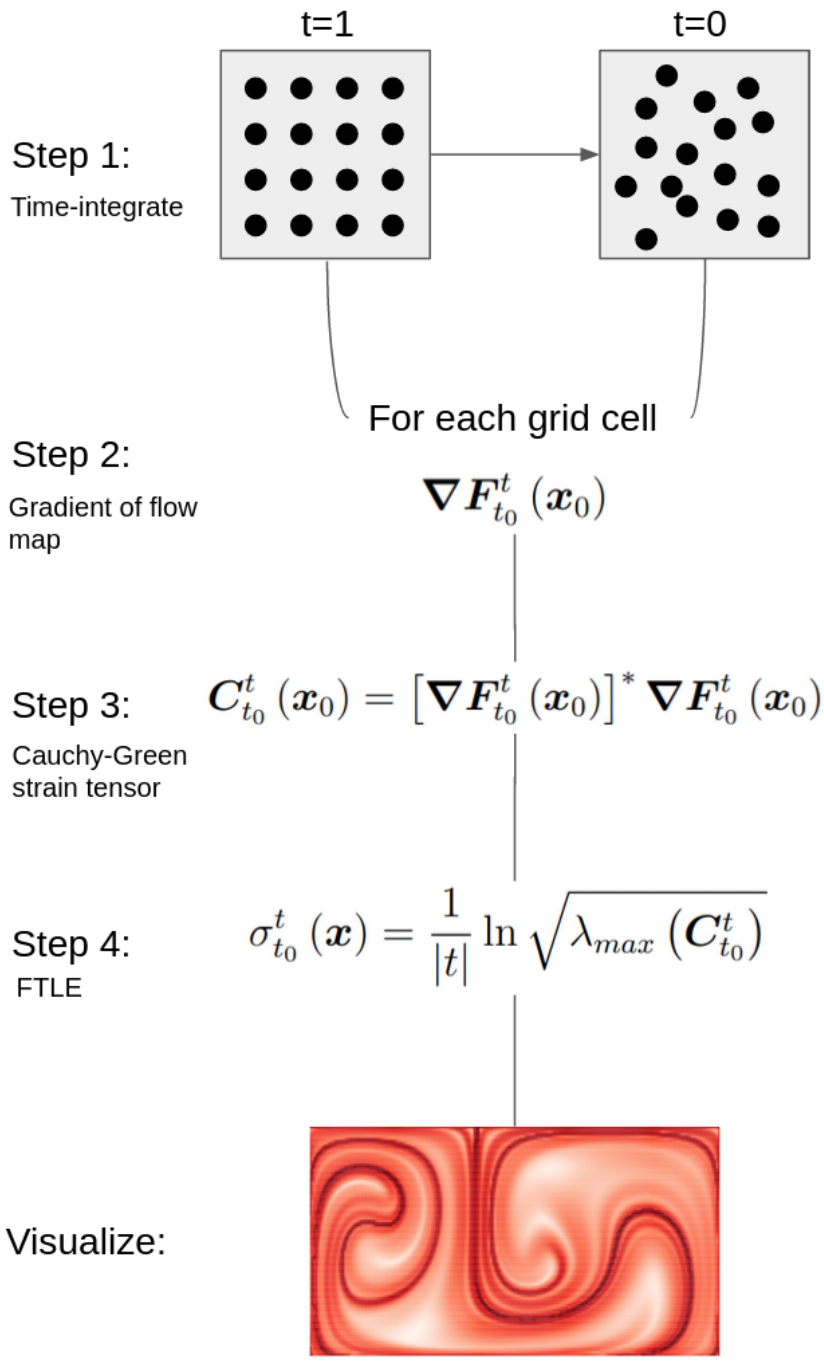

Figure 10: Schematic of my LCS detection software. Step 1) a grid of particles is integrated over a set time interval. Step 2) The Jacobian of the flow map is computed for each grid cell. Step 3) Cauchy-Green Strain tensor is computed. Step 4) Maximum eigenvalue of the Cauchy-Green strain tensor is used to compute FTLE. The FTLE values for each grid cell can then be visualized. An example of attracting hyperbolic LCSs is shown here for the double-gyre system.

attracting hyperbolic LCSs. Only initial and final particle positions are necessary for further computations, whereas intermediate positions are not needed. The integration time will be set to 24 hours when computing LCSs in the Barents-2.5 EPS, unless stated otherwise. The flow map from Eq. 3, which maps the flow of particles from their initial to final position, is now obtained, and the Jacobian of the flow map (Eq. 4) can be computed in step 2.

The Jacobian of the flow map has to be computed for each grid cell, and the central aim of this computation is elongation rate, i.e. the change in distance between particles. In Figure 11, the view is centered on particle $\boldsymbol{x}_{i,j}$. This particle corresponds to a single grid cell in the model, and the elongation between neighbouring particles over the time interval can be investigated. At $t = 1$, particles are positioned at their initial locations, and the distance between particles is the same in all directions. Therefore, the distance between particles $\boldsymbol{x}_{1,i-1,j}$ and $\boldsymbol{x}_{1,i+1,j}$ is given by $2\Delta x_1$, that is, twice the distance between particles in the x-direction. Likewise, the distance between $\boldsymbol{x}_{1,i,j-1}$ and $\boldsymbol{x}_{1,i,j+1}$ can be expressed by $2\Delta y_1 = 2\Delta x_1$.

At $t = 0$, particles have been advected backwards in time by the underlying velocity. As the velocity field is not homogeneous, particles have been advected differently during the integration time. The distance between particles at $t = 0$ is no longer equidistant, and the distance has to be calculated by taking the difference between their positions. Thus, for each grid cell $\boldsymbol{x}_{i,j} = (x_{i,j}, y_{i,j})$, the components of Eq. 4 can be expressed numerically as

$$\begin{aligned}
\frac{\partial x_0}{\partial x_1} &= \frac{x_{0,i+1,j} - x_{0,i-1,j}}{2\Delta x_1} \\
\frac{\partial x_0}{\partial y_1} &= \frac{x_{0,i,j+1} - x_{0,i,j-1}}{2\Delta y_1} \\
\frac{\partial y_0}{\partial x_1} &= \frac{y_{0,i+1,j} - y_{0,i-1,j}}{2\Delta x_1} \\
\frac{\partial y_0}{\partial y_1} &= \frac{y_{0,i,j+1} - y_{0,i,j-1}}{2\Delta y_1}
\end{aligned} \tag{29}$$

Next, the software computes $\boldsymbol{C}_{t_0}^t$ from Eq. 8 for each grid cell using the corresponding $\boldsymbol{\nabla F}_{t_0}^t$ for that grid cell. Following Eq. 19, the highest eigenvalue of $\boldsymbol{C}_{t_0}^t$ is selected using the *numpy.linalg.eigvals()* function from the numpy Python package (Harris et al., 2020), which is used to compute the largest FTLE value over the time interval at each grid point. Solving for the largest eigenvalue of $\boldsymbol{C}_{t_0}^t$ yields the strongest deformation rate, and the corresponding largest eigenvector yields the direction for which deformation is strongest. Finally, we have a grid of FTLE values, which can be visualized to approximate attracting hyperbolic LCSs.

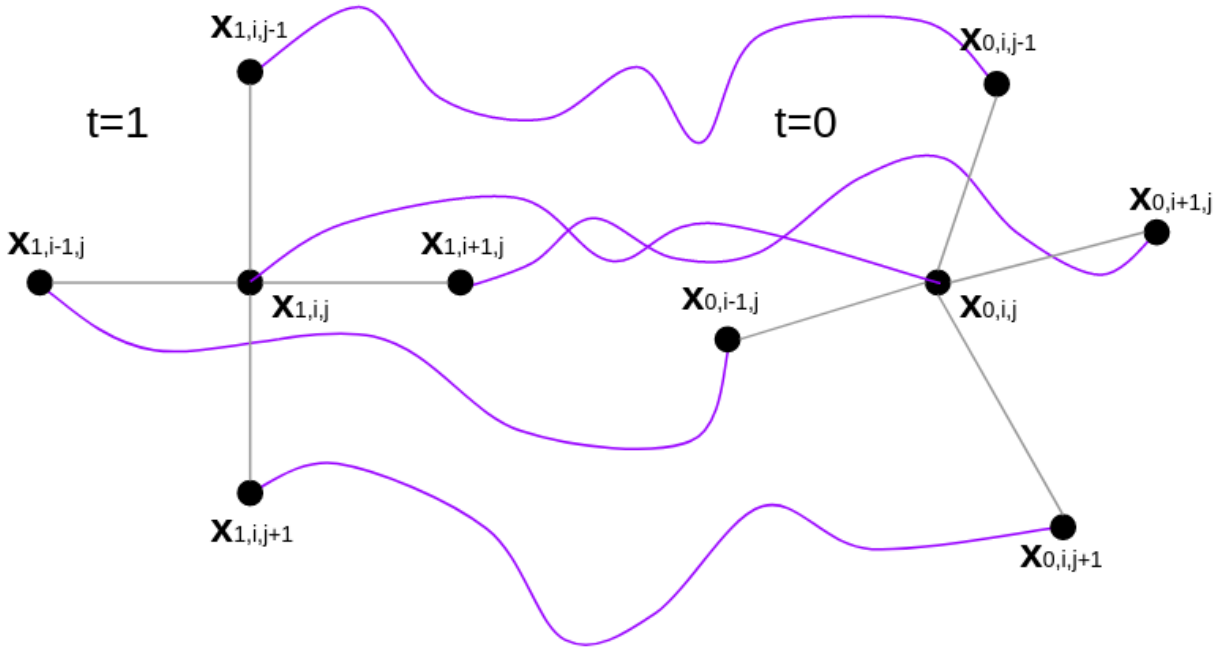

Figure 11: The flow of a particle $\boldsymbol{x}_{i,j} = (x_{i,j}, y_{i,j})$ and its neighbouring particles positioned in a velocity field. Particles are initially positioned in an equidistant grid at $t = 1$, so the distance between all particles is the same. Particles are advected by the underlying velocity field, and their positions at $t = 0$ are shown. At $t = 0$, the distance between particles is no longer equidistant. Purple lines show each particles' movement over the time interval, which is mapped out by the flow map.

3.6 Validation of Lagrangian Coherent Structure

I will conduct a simple experiment in the double-gyre system to verify whether particle trajectories are in fact shaped by LCSs computed using my LCS detection software. Here, I will compute attracting hyperbolic LCSs using short backwards integrations at different simulation times of the double-gyre system, with the expectation that LCSs at one time are independent of LCSs at other times. Separately from the LCS computations, I will release a cluster of particles at the double-gyre simulation start, and conduct a long forwards-in-time Lagrangian particle integration using the background velocity field. If the theory and my implementation are valid, advected particles should be attracted towards the locally strongest LCS, getting shaped by and spreading along the attracting LCSs, but never crossing through them. As mentioned in Sections 2.1.2 and 3.4, future particle states are dependent on their state history, whereas LCSs are independent of each other given that they are computed over different time intervals.

A similar experiment will be conducted for LCSs computed in the Barents-2.5 EPS velocity field. Instead of computing LCSs for different times, I will rather compute one attracting LCS field for a selected time. Then, particles will be placed in a grid seven days prior to the LCS field and advected forwards-in-time towards the time the LCS field is computed at. During this seven day integration time, particles are likely to have drifted long enough for their trajectories to be impacted by LCSs. A comparison between these two will yield information about whether particle trajectories are in fact affected by LCS. However, the Barents-2.5 EPS velocity field is more chaotic and uncontrolled than the analytical double-

gyre system. New flow structures constantly emerge and disappear in the model, meaning that particle trajectories can be affected by LCSs which existed prior to the LCSs computed at the final date. Thus it is expected that particle trajectories and LCSs will be more related in the double-gyre system than in Barents-2.5 EPS.

3.7 Detecting Robust and Persistent LCSs

To detect which, if any, LCSs are robust or persistent, an average of LCSs over ensemble members and time will be computed. It is expected that there will be differences in the LCSs predicted by ensemble members as the velocity fields are perturbed, as well as changes in LCSs over time in a single ensemble member following their time-dependency. However, the average might reveal any similarities over ensemble members and time. The average is defined as

$$\overline{F} = \frac{1}{N} \sum_{i=0}^{i=N} F_i, \tag{30}$$

where $\overline{F}$ is the average value, F_i is the i-th sample for F and N is the number of samples. To differentiate between averages, the notation $\overline{F}_m$ refers to an *average over ensemble members*, whereas $\overline{F}_t$ refers to an *average over time*.

The standard deviation (SD) then gives a measure of the spread in the sample distribution. A low SD signifies that individual samples are close to the average, and a high SD signifies that there is a large spread in the samples. SD is defined as

$$\sigma = \sqrt{\frac{\sum_{i=0}^{i=N} |F_i - \overline{F}|^2}{N}}, \tag{31}$$

where σ is the SD, and the other variables are the same as for the average. As with the average, σ_{F_m} signifies a *SD over ensemble members* and σ_{F_t} signifies a *SD over time*.

A conceptual example of two individual LCSs and their approximate average is shown in Figure 12. The two LCSs act as either repelling or attracting LCSs at two different locations. The resulting average field is a combination of these two LCSs, yielding an average region of attraction/repulsion. Assuming that both LCSs consist of the same homogeneous FTLE values, the average will have two times higher FTLE values in the location where the two LCS intersect than everywhere else. Therefore, the average smooths out the LCSs, transforming them from simple curves to a 2D field. In essence, resulting $\overline{F}_m$ and $\overline{F}_t$ will not directly yield regions of attraction/repulsion, but rather, regions where LCSs are statistically more likely to form over ensemble members or time.

Generally, the SD gives information about the spread of the field around the average. A high average and low SD in a part of the domain signifies that it is virtually certain that LCSs are formed here, whereas a high SD signifies that there is a low certainty. However, in this case the SD might not contain much information about certainty. Assuming that the LCSs in Figure 12 are only separated by a small distance, the average will cover a small region, thus yielding an accurate estimate for where LCSs can be found. Yet the SD will be large as the LCSs are perturbed and only overlap at a single point in space.

The extent of the average region and SD will be smaller if the LCSs overlap, whereas the FTLE values contained in the average region will be greater. This yields a high certainty

about the position of LCSs, hence there is a high robustness or persistence. If the average covers a larger region and the average FTLE values are smaller, then it can be assumed that the average has smoothed out the field to a larger degree because predicted LCSs are perturbed by some distance. The SD will likely be large in that case. In that sense, it can be assumed that LCSs are predicted inside the average region, but their exact position is variable. Hence it is highly certain that LCSs exist in this general region, but their exact position are uncertain across ensemble member or time.

Additionally, the ensemble average, $\overline{F}_m$, and time average, $\overline{F}_t$, should not be considered as definitive transport barriers. The reason for which is that it is unknown whether the LCSs which form this average are from the same model realization or exist at the same time. It is also impossible to deduce whether average consist of a few long LCSs or many short LCSs. The former is acting as transport barriers over a large region, whereas the latter only act as transport barriers over a short distance, so material can drift between them. Instead, $\overline{F}_t$ and $\overline{F}_m$ should be considered as average accumulation or dispersion regions for attracting and repelling LCSs respectively, with the *potential* of containing a transport barrier.

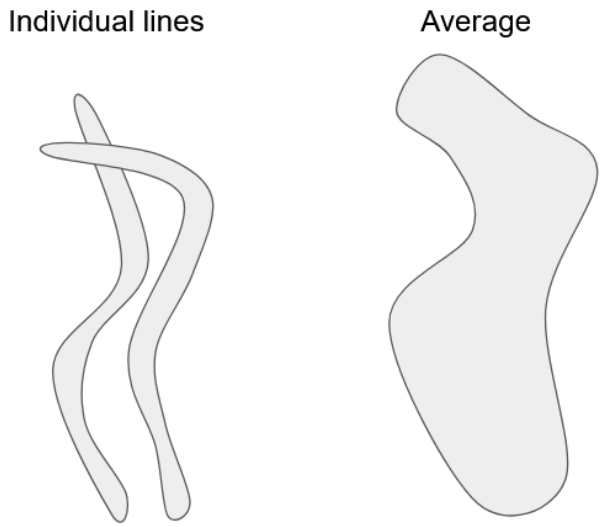

Figure 12: Example of two LCSs (left) and the average region covered by the LCSs (right).

A final note is that the FTLE given in Eq. 19 is a logarithmic value. This can cause complications in both the averages and SDs, as

$$\sum_{i=1}^{i=2} \ln\left(X_i\right) = \ln\left(X_1\right) + \ln\left(X_2\right) = \ln\left(X_1 \cdot X_2\right). \tag{32}$$

The average might therefore not necessarily be the best method for finding robust and persistent LCSs.

4 Results

In this section, presentation of results is divided into two parts: 1) LCSs in the double-gyre system and 2) LCSs in the Barents-2.5 EPS. As outlined in Section 3, the first part is meant as a testing environment for my implementation of the methods. Here, I study whether or not particle trajectories are influenced by LCSs in a simple system and how this system responds to small perturbations in parameters. In the second part, I apply the methods to an operational forecasting system which is modelling turbulent ocean velocity fields, representing realistic flow.

4.1 The Analytical Double-Gyre System

4.1.1 Verification of Lagrangian Coherent Structures in the Analytical System

LCSs in the analytical double-gyre at four different times can be seen in Figure 13. Corresponding velocity fields are present in Figure 8. Particles have been placed on top of a locally strong attracting LCS at time $t = 0$, located to the left of the separation between the two gyres, which will be referred to as the *conflux* from now on. For visualization, particles initially located to the left of this LCS are colored in blue, whereas particles on the right are colored in green. As the system evolves, the velocity field has advected and reshaped the cluster of particles. Snapshots of their positions are shown with the corresponding attracting LCSs for that time. The evolution of LCSs is not perfectly captured in these four images; therefore, a video of their evolution over time can be found here or go to the GitHub in Appendix C.

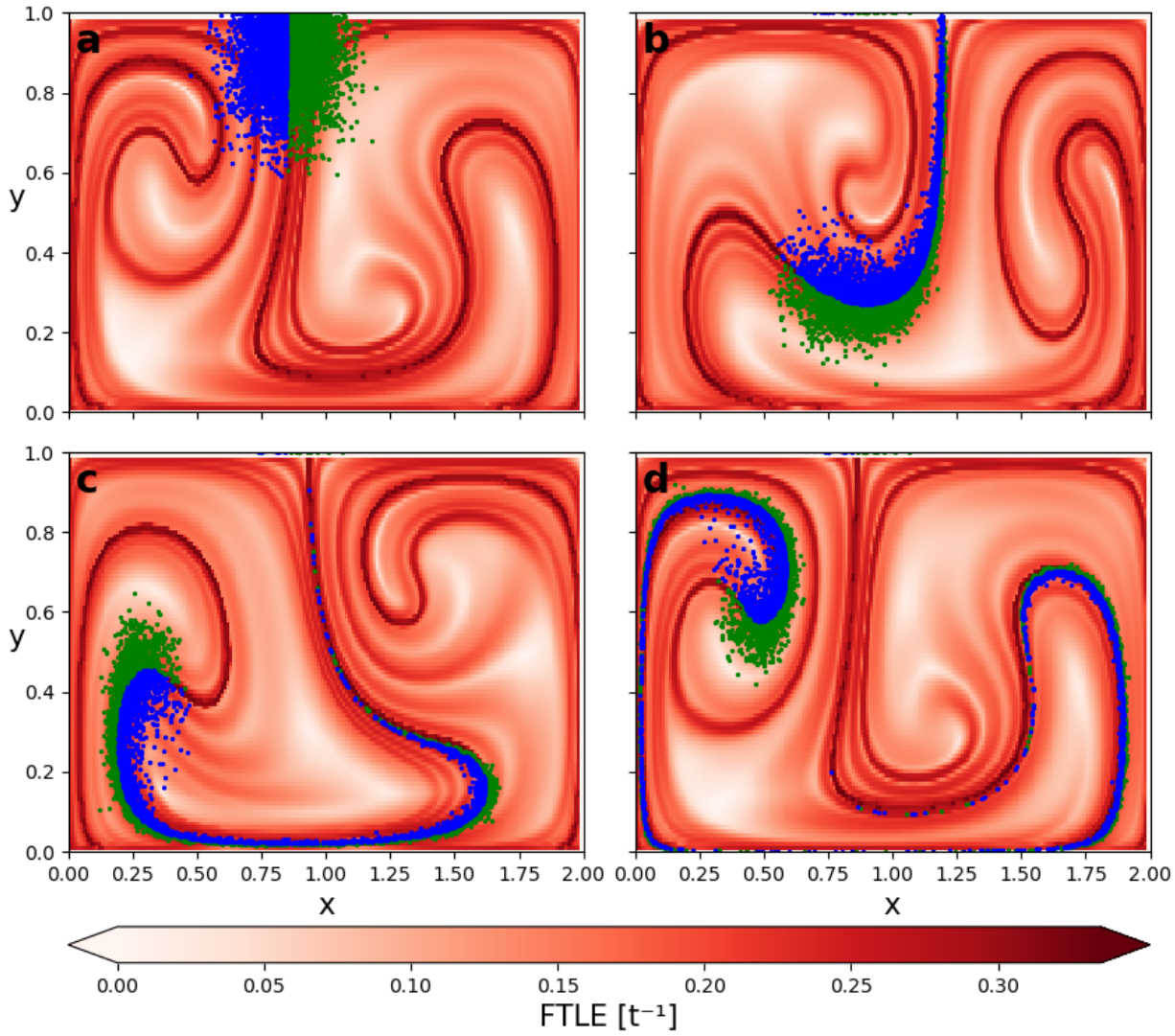

Figure 13: Approximation of attracting LCS (red) calculated with FTLE method for the analytical double-gyre at times: a) $t = 0$, b) $t = 3$, c) $t = 6$ and d) $t = 9$. Double-gyre parameters are with parameters $\epsilon = 0.25$, $\omega = 0.682$ and $A = 0.1$. Stronger red regions signify stronger attraction in the domain. Blue and green dots are advected particles which have been placed in the system at $t = 0$ and allowed to drift with the velocity field for the duration of the simulation. The particles have the same properties, and are colored based on which side of the underlying LCS they are initially located on.

As seen in Figure 8, the left gyre rotates clockwise, whereas the right gyre rotates counter-clockwise. As such, particles placed in the top-middle of the domain at $t = 0$ are expected to initially drift downwards, then drift either left or right, depending on which gyres' velocity field has the strongest influence, then upwards and finally towards the middle again.

Advected particles are seen to drift towards regions of high attraction in the figure, following these regions as the system evolves. The particle cluster in Figure 13a is seen to stretch along the locally strongest attracting LCS as the system evolves, similarly to what can be seen in the schematic in Figure 2, leaving a trail of particles behind. Particle trajectories are seen to follow the aforementioned expected drift from the previous paragraph, while also curving with the curvature of the underlying LCSs. Thus particle trajectories are seen to be shaped by the LCSs.

The LCS around which particles are initially positioned follows the conflux and both are seen to move left and right periodically. Particles located on top of this LCS are seen to follow this sideways shift while also drifting downwards along this LCS. Furthermore, the particles are seen to be advected towards the boundaries of the system, where they can be seen to spread along the bottom wall in Figure 13c and along the left and right walls in Figure 13d.

Notice that the LCSs have shaped particle trajectories in such a way that both green and blue particles can be found in both gyres at times $t = 6$ and $t = 9$. Even though particles were initially positioned in close proximity to one another, they have drifted in different directions. Furthermore, the particles initial positions with respect to the conflux LCS does not decide which gyre they end up in, as both colors of particles are found in both gyres at time $t = 9$. Rather, their position at $t = 9$ appears to be dependent on how the dominating LCS which shape their trajectories has developed.

As theory suggests, particles are supposed to be attracted towards the locally strongest attracting LCS and spread along it. However, particles should not be able to cross this LCS as it acts as a transport barrier. This can be seen to happen in all panels of Figure 13. The particles are clearly separated into green and blue particles at all times, with the LCS acting as the border of separation. There is no clear indication of particles crossing through this LCS, at least not drifting a meaningful distance through it. The simulation shows that the LCSs act as transport barriers.

Particles and LCSs have been computed independent of each other. Particles have been advected forward in time from $t = 0$, and their new positions at the next time step are dependent on their positions at the previous time step. Meanwhile, the LCSs have been computed by advecting a grid of particles backwards in time and LCSs at one time step are independent of LCSs at different time steps. It is interesting to see that even though LCSs are changing drastically from one time to another, advected particle trajectories continue to be shaped by them.

4.1.2 Analytical System with Perturbed Parameters

An ensemble of an analytical double-gyre system has been produced, as described in Section 3.1.2. 25 values for the ϵ and ω parameters have been randomly selected with a Gaussian distribution and resulting values for both parameters are shown in Figure 14. The parameters are then randomly paired to create an ensemble of 24 analytical double-gyres. The velocity fields and computed LCSs for the ensemble at simulation time $t = 3$ are shown in Figure 15. The constants across the ensemble are the rotational velocity A, the system boundaries and the fact that there exists two separate gyres .

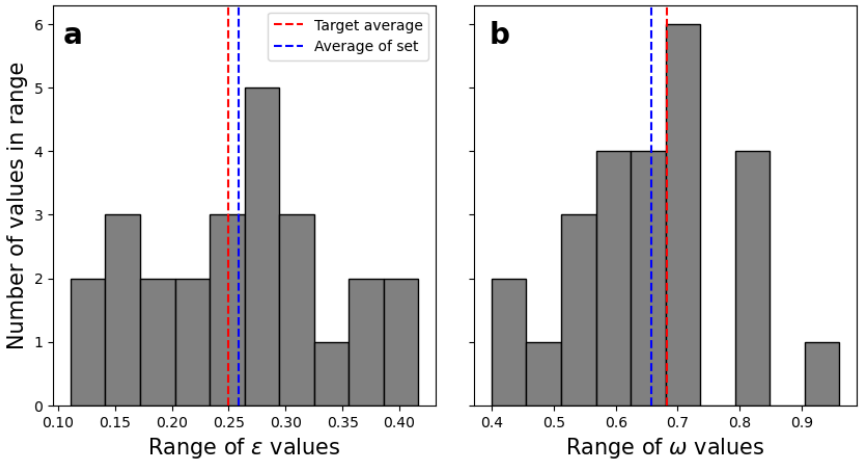

Figure 14: Spread of 25 randomly Gaussian distributed a) ϵ and b) ω values around the average values $\overline{\epsilon} = 0.25$, $\overline{\omega} = 0.682$ and standard deviation $\sigma_\epsilon = 0.1$, $\sigma_\omega = 0.15$. The red line in indicates the inputted target average, $\overline{\epsilon}$ and $\overline{\omega}$, while the blue line indicates the average value of the randomly distributed sets, which is $\overline{\epsilon}_{set} \approx 0.259$ for ϵ and $\overline{\omega}_{set} \approx 0.658$ for ω. The standard deviations of the randomly distributed set are $\sigma_{\epsilon_{set}} \approx 0.084$ and $\sigma_{\omega_{set}} \approx 0.129$

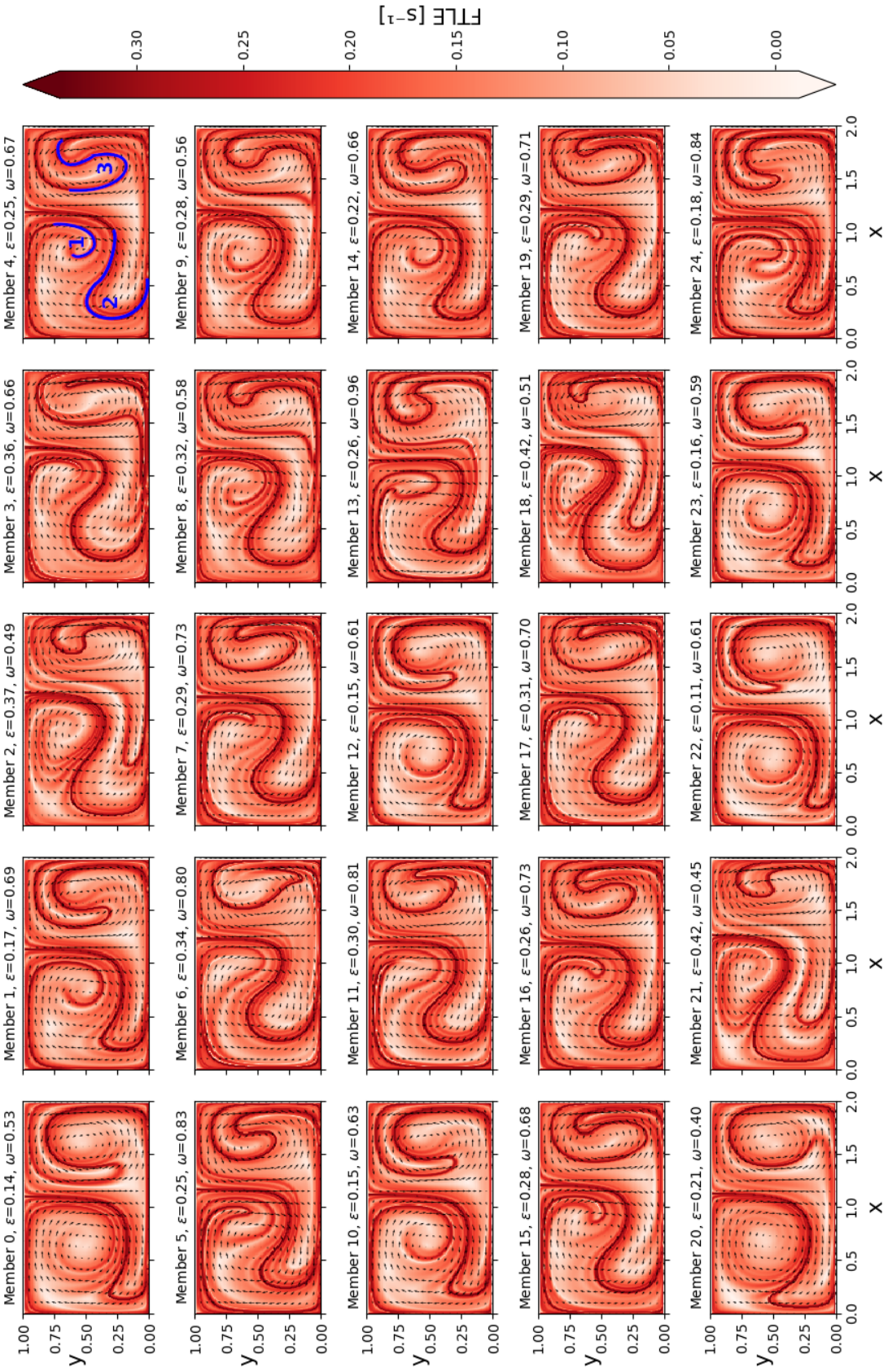

Figure 15: An ensemble of an analytical double-gyre system. Produced by perturbing the ϵ and ω parameters with a Gaussian distribution and keeping A constant. Attracting LCSs have been computed for simulation time $t = 3$ and are seen in red. The velocity field of the systems is shown with black arrows. Each ensemble member is marked by a number between 0-24, and the corresponding ϵ and ω is in their title. Blue lines in member four highlight three dominant LCSs of interest.

First investigating the velocity fields, the most notable difference between ensemble members is the location of the conflux along the x-axis. The position of the conflux is dependent on two factors: 1) how fast these two gyres propagate left and right and 2) how much the gyres contract and expand before bouncing off the wall and switching propagation direction. The former being described by ω and the latter described by ϵ. Increasing ω yields faster left-right propagation, whereas increasing ϵ increases the left-right distance the gyres can propagate. Other differences in the velocity field are marginal.

Shifting focus to the LCSs, each ensemble member contains an attracting LCS in the middle of the system. This specific LCS starts in the top-middle of each system and moves straight downward, effectively acting as a barrier between the two gyres. As the conflux moves, so does this LCS, thus its location is also dependent on ω and ϵ due to the aforementioned reasons. However, the length of this LCS along the y-axis before it curves towards the left is variable between ensemble members.

Three LCSs of interest have been highlighted and numbered in ensemble member four. Other than the conflux LCS, these three appear to be the most prominent LCSs in the system, but are seen to be highly variable across the ensemble. LCS 1 appears to be the most variable LCS in the ensemble, in the sense that it is not present/easily distinguishable in all ensemble members, e.g. 0 and 20. LCS 2 resembles a large tongue-like structure that stretches along the bottom part of the domain. The thickness of this tongue is its most notable difference across the ensemble. Furthermore, members 2, 18 and 21 show the existence of a smaller tongue inside LCS 2, that is not present in other members. Finally, LCS 3 is another tongue-like structure that stretches upwards along the right wall and curves around itself. The shape of its downwards curvature and the tongues thickness varies drastically across the ensemble.

Overall, it is shown in Figure 15 that there is a higher visible variation between LCSs than velocity fields in the ensemble. All ensemble members show a clear indication of the three highlighted LCSs, expect for some of the members which are missing LCS 1. As these three LCSs, in addition to the conflux LCS, are present in all ensemble members, it can be concluded that they are virtually certain to exists in some form or another. Their presence is therefore considered robust. However, the shape of the LCSs varies between ensemble members, where LCS 1 and LCS 3 show the largest variability. Additionally, all ensemble members show higher FTLE values along the boundaries.

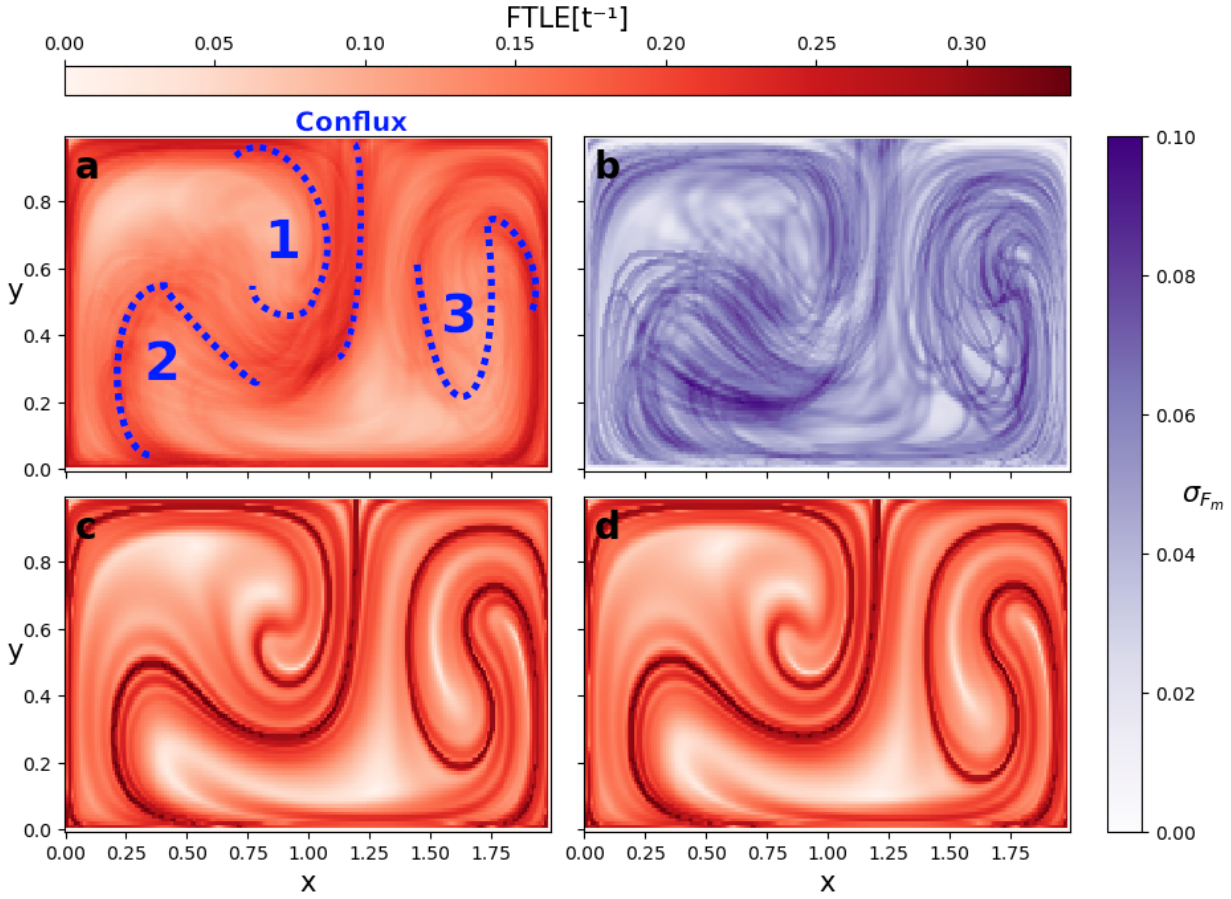

Figure 16: a) The average attracting LCSs $\overline{F}_m$ over ensemble members. Dashed blue lines indicate where LCS 1, 2, 3 and conflux LCS are usually positioned in the ensemble. b) The standard deviation σ_{F_m} over ensemble members. c) LCS computed with double-gyre parameters $\epsilon = 0.25$ and $\omega = 0.682$, which were the average values for the Gaussian distribution. d) LCS in a double-gyre with the ensemble average values for the two parameters, $\overline{\epsilon}_{set} \approx 0.259$ and $\overline{\omega}_{set} \approx 0.658$.

The average of attracting LCSs, $\overline{F}_m$, and its standard deviation, σ_{F_m}, have been computed for the double-gyre ensemble and are shown in Figure 16a and 16b respectively. Additionally, the LCSs for a double-gyre computed with the target values from Figure 14 and one computed using the average values of the ensemble are shown in Figures 16c and 16d. Immediately notice that $\overline{F}_m$ has smoothed the LCSs by a large degree. The highest $\overline{F}_m$ values are lower than the ones seen in Figures 16b and 16c, whereas the lowest values are higher. Therefore, the gradient between maximum and minimum values has decreased.

LCSs are no longer clearly defined in $\overline{F}_m$. Instead, stronger red regions signify locations where the LCSs are generally found across the ensemble. The conflux LCS, as well as LCS 2, are distinct characteristic LCSs found in all ensemble members. An indication of these two is seen in $\overline{F}_m$. It can be seen from Figure 15 that the conflux LCS is slightly perturbed along the x-axis across ensemble members. This is reflected in σ_{F_m}, which shows a small increase in σ_{F_m} in the general region where this LCS is usually positioned. However, the region covered by σ_{F_m} is small around the conflux, so that both the existence and position of this LCS is certain.

The numbered LCSs are seen to be more variable across the ensemble members in Figure 15. LCS 1 was seen to not be present in all ensemble members and its shape varies drastically.

Incidentally, there is no clear indication of LCS 1 in $\overline{F}_m$ and its existence can therefore not be ascertained from $\overline{F}_m$, even though it is seen in individual members. However, large σ_{F_m} values along the top wall to the left of the conflux indicate that there is LCS activity here.

Both LCSs 2 and 3 can be identified in $\overline{F}_m$. Large 2D fields of relatively high average FTLE values are present in Figure 16a where LCS 2 and 3 are usually positioned, thus their existence is virtually certain across the ensemble. However, because of their variability in the ensemble, their exact positions are uncertain. This is reflected in σ_{F_m}, which is large in both regions. σ_{F_m} indicates that although LCS 2 is virtually certain, it can be located practically anywhere in the bottom-left quarter of the domain.

A part of LCS 3 is always present along the right wall, which is indicated by high values in $\overline{F}_m$ in this region and along all other walls. Furthermore, σ_{F_m} is small along the domain boundaries, signifying that it is virtually certain that LCSs exist along the walls. This is not surprising, as particles are not able to pass through walls. Hence, particles which flow into a wall will accumulate here, as can be seen happening at $t = 9$ in Figure 13

However, the rest of LCS 3 is not as prominent in $\overline{F}_m$. The ensemble predicts that this LCS will curve downwards, but its downwards extent is highly variable. The downwards curve is therefore easily distinguishable in $\overline{F}_m$, but the rest of LCS 3 can be hard to spot. It no longer resembles a tongue. This is also reflected in the high values of σ_{F_m}, which span over a large portion of the right gyre. Therefore, it is known that LCS 3 will exist in the system in some form or another, but its position can be anywhere inside the right gyre.

In essence, it is shown here that $\overline{F}_m$ is able to indicate regions where LCSs are generally formed. The standard deviation, σ_{F_m}, then yields information about spacial spread of these LCSs and thus their certainty. This same method will now be applied to LCSs in the Barents-2.5 EPS, to check for robustness and persistence.

4.2 The Barents-2.5 EPS

4.2.1 Velocity fields in the Barents-2.5 EPS

Instantaneous absolute velocity fields from four ensemble members of the Barents-2.5 EPS are shown in Figures 17a-17d. It is evident that velocities in the model differ over ensemble members, although some similarities arise. Particularly, all four ensemble members predict high velocities in the upper part of the domain and along the bathymetry contours south of Vestfjorden. As discussed in Section 3.2, the NCC flows northwards along the coastline, and branches into two parts south of Vestfjorden. One part then flows into Vestfjorden, which is likely the high velocity seen here in Figure 17.

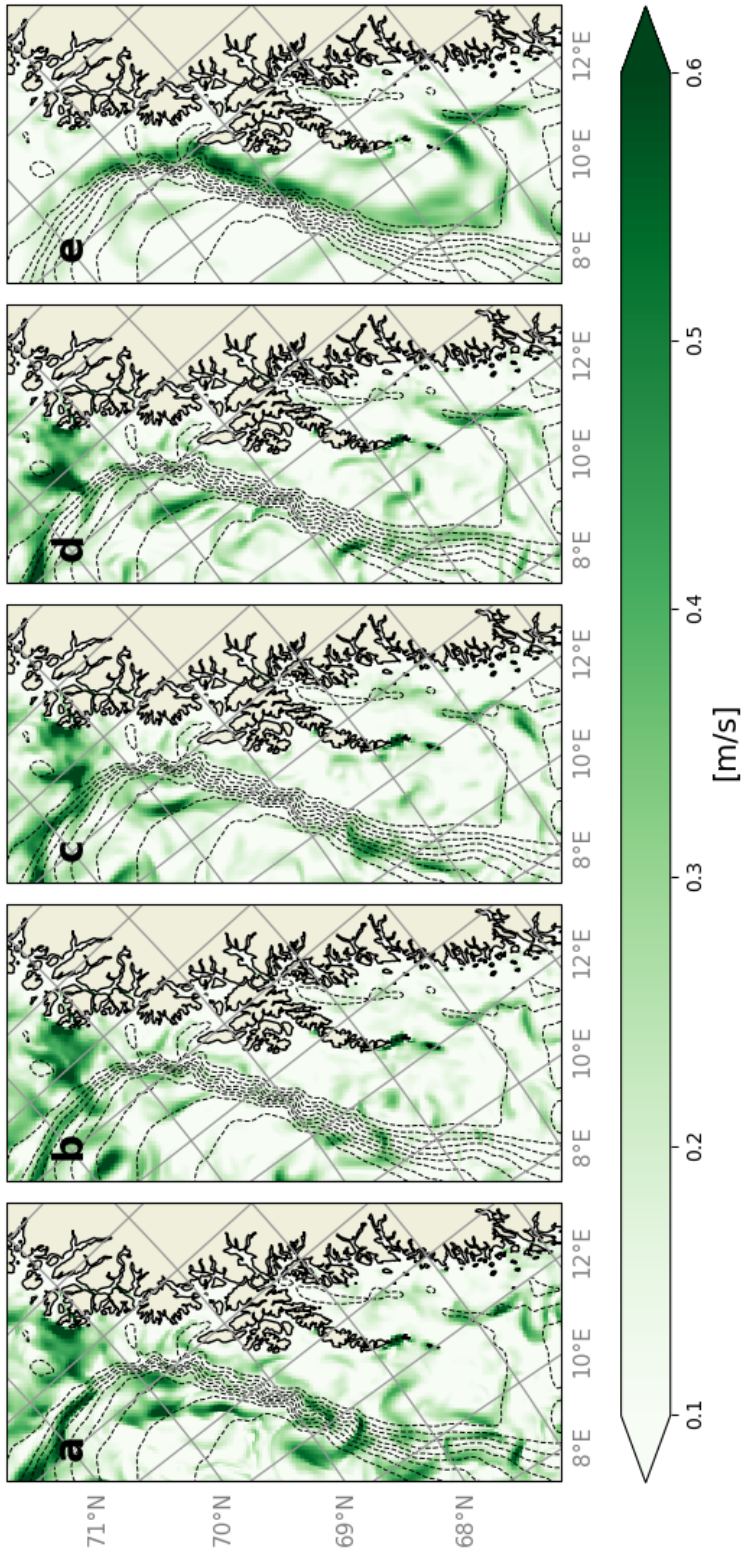

Figure 17: Instantaneous absolute velocity fields computed by $\sqrt{u^2 + v^2}$, where u and v are the longitudal and lateral components of the velocities respectively, for four members of the Barents-2.5 EPS model on April 4, 2022. These only show the magnitude of the velocity and not the direction. a) Member 0, b) member 1, c) member 2 and d) member 3. e) The average velocity field over April, averaged over all 24 ensemble members. The average absolute velocity field in e) has been multiplied by a factor of 2 to enchance visibility with regards to the other panels.

A major difference in velocity fields can be seen along the steep continental slope. Both the NwASC and NCC flow in this region, but only ensemble member 0 predicts particularly high velocities here. The velocities along the continental slope are inconspicuous compared to the surroundings in the three remaining ensemble members. As described in Section 3.3, member 0 is forced by AROME-Arctic, whereas the other member depicted in Figure 17 are forced by ECWF-ENS, which could be the reason for why only member 0 shows high velocities at the continental slope. Figure 17 is an example of the spread in the velocity fields between ensemble members.

The monthly and ensemble averaged velocity field is shown in Figure 17d. Note that this average is multiplied by a factor of 2, and as such, showcases lower absolute velocities than the individual instantaneous absolute velocity fields in Figures 17a-17d. This is due to the fact that the average smooths out the velocity field. The average current show stronger velocities south of Vestfjorden, where one part of the NCC flows. Furthermore, Figure 17d indicates prominent velocities along the continental slope. This implies that there is in fact a strong current in this region on average, even though the current itself might vary on hourly and between ensemble members.

4.2.2 Verification of Lagrangian Coherent Structures

A similar experiment to the one conducted in Figure 13 for the analytical double-gyre is shown in Figure 18, now for the Barents-2.5 model. A grid of particles has been released and advected forward in time to their final position after seven days. Figures 18a and 18b show the particles initial and final positions respectively. The LCSs in the background of these figures are the same and are computed for the final date. These LCSs are shown in Figure 18c without particles to enhance their visibility.

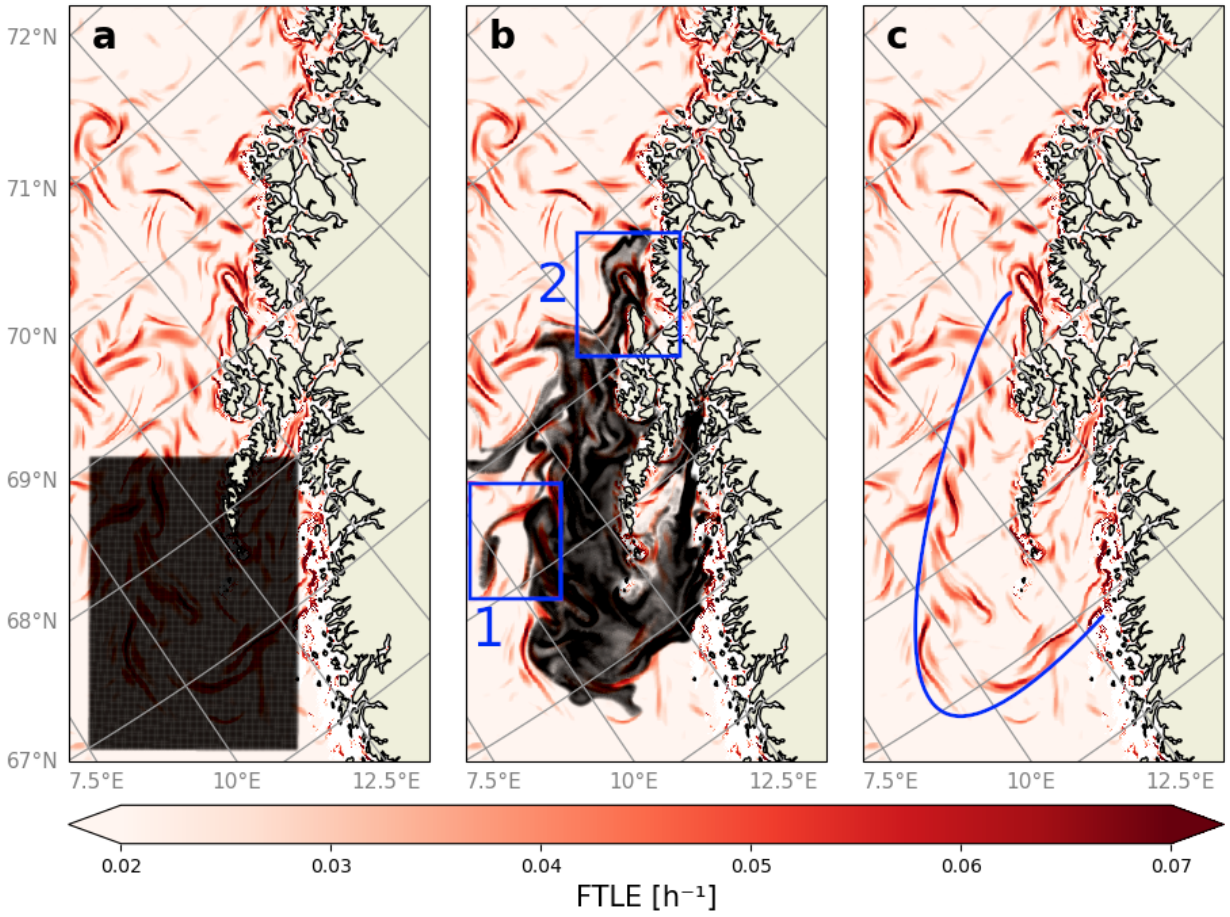

Figure 18: Particles in a field of attracting hyperbolic LCSs represented as FTLE field. Hyperbolic LCSs are the same for all panels, and computed for 2022.11.07. a) initial position of a grid of particles marked with black dots, at time 2022.11.01. The velocity field is used to integrate the particle transport seven days forward in time. b) Final positions of particles at 2022.11.07. Particles that collide with the coastline during the integration time are removed from the system. Blue boxes highlight two regions of interest. c) Hyperbolic LCSs for 2022.11.07, without the particles to enhance their visibility. The blue line outlines the general shape of underlying LCSs. Velocity fields are provided by the Barents-2.5 model.

The modelled Lagrangian particle trajectories have been affected by the LCSs. A blue line in Figure 18c traces a half elliptic shape of LCSs around LoVe, effectively tracing what appears to be a transport barrier around the islands. Albeit the traced LCSs seem to be disjointed, thus forming gaps in this transport barrier. Incidentally, the region inside the blue line is also the region where most of the particles are located at their final position, which indicates that the LCSs retain particles on the continental shelf for the simulation duration. Furthermore, the outline of the particle cluster at their final position is seen to approximately take the shape of the LCSs.

The two blue boxes in Figure 18b highlight two regions of interest. Box 1 highlights a trail of particles which flow westward away from the main particle cluster. It can be seen that this trail of particles is located on top of an attracting LCS and stretch alongside it, emphasizing the potential accumulation region property of attracting hyperbolic LCSs. Box 2 highlights a region where there are strong and clearly defined LCSs ordered in an elliptic pattern. Particles can be seen to follow this pattern quite accurately. There is a large concentration of particles seemingly close to the highlighted LCSs,and a low concentration

of particles inside the elliptic LCS pattern, thus the pattern attracts particles, but does not allow particles to propagate towards the center of the LCS. This indicates that particles are attracted towards the LCSs in the moment on small scales.

Finally, there is a large and thick trail of particles extending westward out of the main particle cluster directly north of box 1. At this time, there exist no obvious LCSs responsible for shaping this trail. However, the computed LCSs are just instantaneous fields and can differ drastically between time intervals. This particular trail of particles, seemingly positioned far away from any distinct LCS, can therefore have been shaped by LCSs which existed at this location at previous times.

It is interesting to see that even in model data, where the LCSs are prone to emerging and disappearing over short time intervals, instantaneous LCSs computed of a short time interval can describe the shape of a particle cluster computed with long Lagrangian particle trajectories over a seven day integration time.

4.2.3 Robustness of LCSs

Instantaneous LCSs are shown for eight ensemble members in Figure 19 over the LoVe region. As expected, there are differences in the predicted attracting LCSs due to differences in velocity fields between ensemble members. A notable feature of interest is the spiraling structure found in members 0 and 6 in the top of the domain, where the continental slope curves westward. This feature could potentially be describing an eddy formed in the NwASC, which, as mentioned in section 3.2, tend to break off from the NwASC and drift westwards (Søiland and Rossby, 2013), although investigating the velocity field itself would be necessary to confirm this. This feature is more pronounced in member 6 than in member 0 and is not found in any other ensemble member shown here, although a strong LCS which curves along the continental slope is present here in most members. This feature is therefore uncertain, as its only predicted by two of the eight ensemble members.

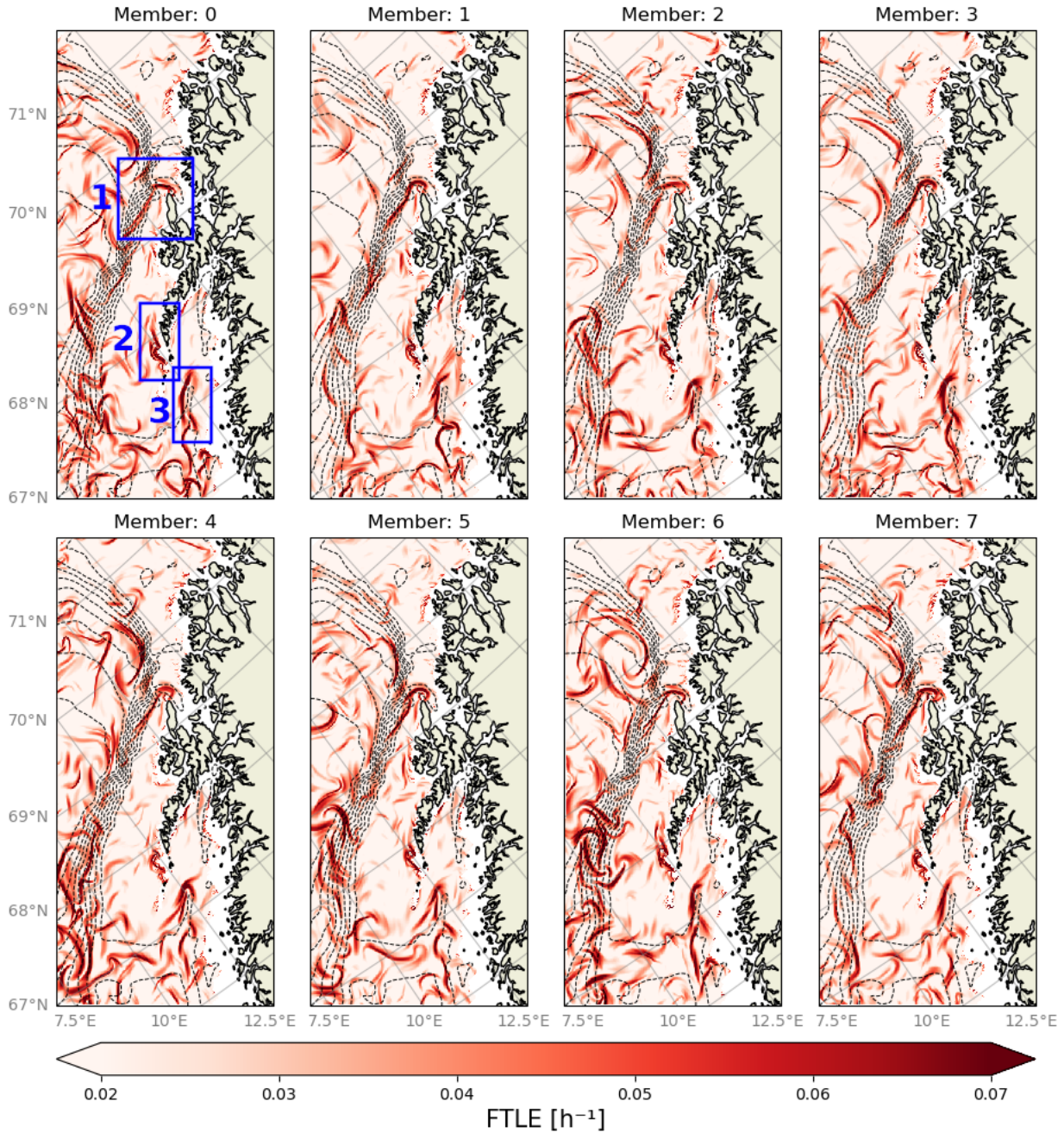

Figure 19: Attracting hyperbolic LCSs approximated with backwards FTLE over the Lofoten-Vesterålen region. Time interval has been chosen to be 24 hours, starting at 2022.04.09 00:00 and integrating backwards to 2022.04.08 00:00. Eight FTLE fields for this date computed using velocity fields from eight ensemble members of the Barents-2.5 EPS model are shown. Red regions symbolize higher FTLE values, therefore also stronger rate of attraction. Ocean bathymetry is indicated by dashed black lines. Blue boxes in member 0 mark three locations where FTLE structures are similar over all members.

Another difference between the ensemble members can be found along the lower part of the continental slope. Here, half of the members predict multiple pronounced attracting LCSs, whereas the other half predicts less activity. As expected, LCSs found in one member are generally different/not present in any other member.

However, some similarities among ensemble members are present. All ensemble members

predict a strong surface current along the continental slope on average and the coastline is constant over ensemble members. Although the exact positions and number of LCSs is different in the ensemble, all members predict more activity along the continental slope. Additionally, there are three features which are almost exactly the same in all members at this particular time. These are highlighted with blue boxes in member 0.

In box 1, all ensemble members predict a pronounced LCS which follows the continental slope and curves around the northern tip of LoVe. The LCS highlighted by box 2 extends along the western coast of the southern tip of LoVe. All ensemble members predict that this LCS starts at the southern tip of LoVe and the shape of it appears to be similar across the ensemble, although its length in the north-east direction along the coastline varies. Box 3 highlights an attracting LCS located south of Vestfjorden, where the NCC flows as discussed in Section 3.2. This LCS is different from the other two in the way that it does not directly interact with the coast, indicating that there can be similarities between ensemble members away from the coast as well.

LCSs are shown to be highly variable across ensemble members. These differences are more immediately noticeable than in the ocean currents from Figure 17. However, the highlighted regions show the existence of locations where LCSs are predicted similarly across the ensemble, which in Figure 19 are regions where the current is steered by geomorphology. Thus these regions are potentially robust.

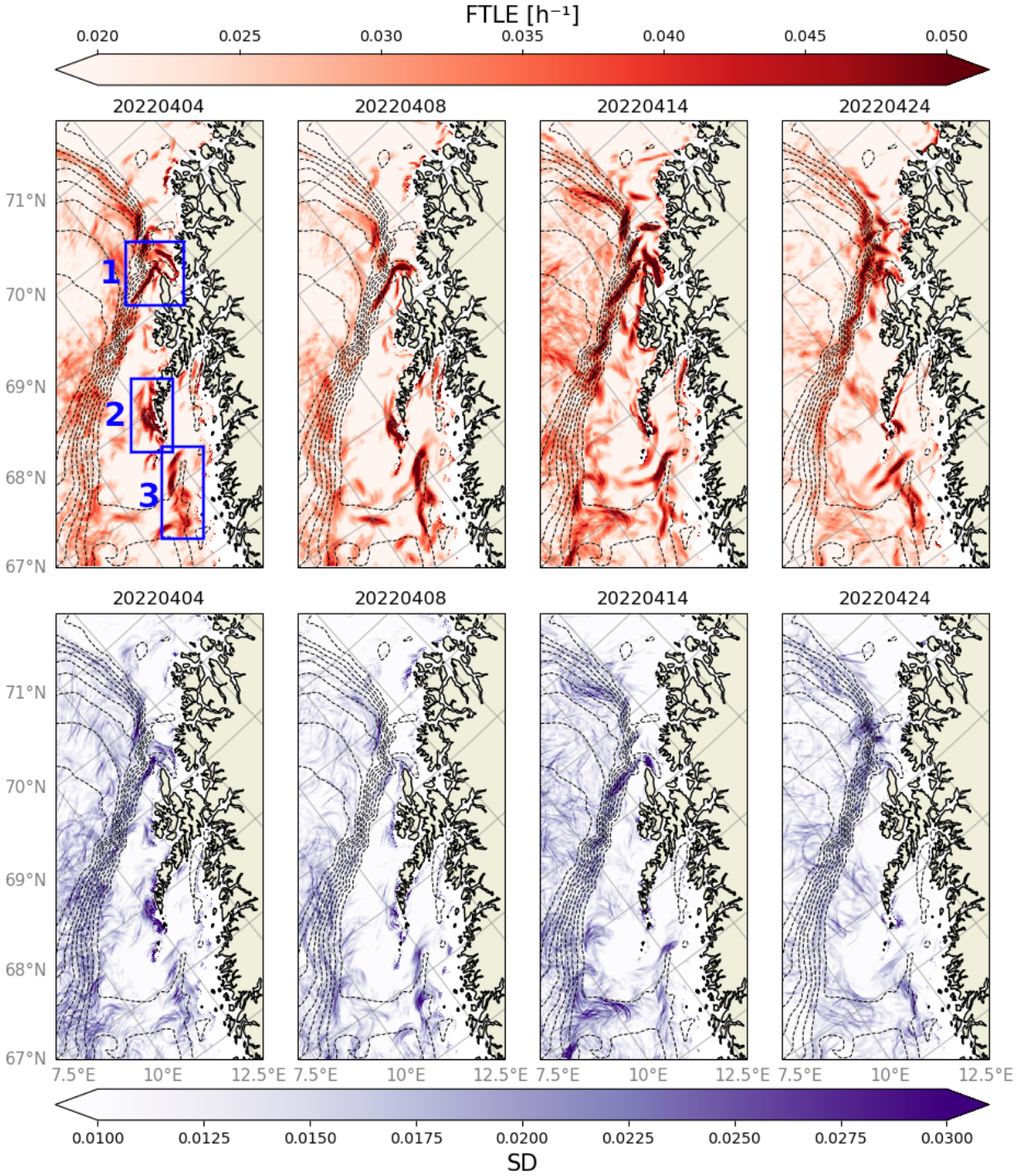

Figure 20: Average attracting LCSs over ensemble members $\overline{F}_m$ (top row) and their standard deviation σ_{F_m} (bottom row) of LCSs over ensemble members for four days in April 2022. $\overline{F}_m$ is colored in red, whereas σ_{F_m} is colored in purple. Bathymetry is visualized with dashed black contours. Blue boxes in the top right panel highlight three regions of interest.

The average attracting LCSs, $\overline{F}_m$, and their standard deviation, σ_{F_m}, over ensemble members are shown for four days in April 2022 in Figure 20. Note that the range of $\overline{F}_m$ is shown from $0.02h^{-1}$ to $0.05h^{-1}$, as to enhance visibility of higher values. The average smooths out the attracting LCSs. This smoothing is seen to transform the LCSs from the simple curves shown in Figure 19 into 2D fields, as discussed in Section 3.7.

The ensemble average, $\overline{F}_m$, shows high average FTLE values directly on top of the steep continental slope for all dates. This signifies that the majority of ensemble members predict high LCS activity here. However, $\overline{F}_m$ is generally smooth over the continental slope west of LoVe, which indicates that ensemble members disagree on the exact positions of LCSs here. This is further emphasized by σ_{F_m}, which indicates large deviation around the continental slope.

The blue boxes in Figure 20 highlight regions which exhibit particularly high $\overline{F}_m$ values. Furthermore, $\overline{F}_m$ still resembles distinct curves inside these highlighted regions. Note that these regions are the same as the ones highlighted in Figure 19, which were considered to potentially contain robust LCSs.

First looking at the region highlighted by box 1 in Figure 20, a distinct LCS is found to curve around the northern tip of LoVe. This LCS is present for all dates, although it is seen to vary to a large degree between the dates. Figure 21 enlarges the region highlighted by box 1 to enhance visibility. On April 4, the distinct LCS can be seen to be surrounded by high FTLE values and is accompanied by a large σ_{F_m}. This signifies that although a distinct LCS is detected on April 4, individual ensemble members have predicted various additional LCSs in this region at this time. Furthermore, due to a large σ_{F_m} directly where the distinct LCS is located on April 4, it can be assumed that the exact location of this particular LCS is perturbed across the ensemble. The shape of this distinguishable LCS is similar on April 8, however, the surrounding high FTLE values has vanished and σ_{F_m} is low on April 8. This means that on April 8, this LCS is highly robust.

On April 18, more distinct LCSs have emerged, extending far north and south along the continental slope. These distinct lines have become thicker, meaning that ensemble members disagree on their exact position, which is reflected in the large σ_{F_m} on this date. Finally, on April 24, the LCS highlighted by box 1 has mostly been smoothed out and σ_{F_m} is large over a large region, signifying that the LCS has become less robust compared to previous dates.

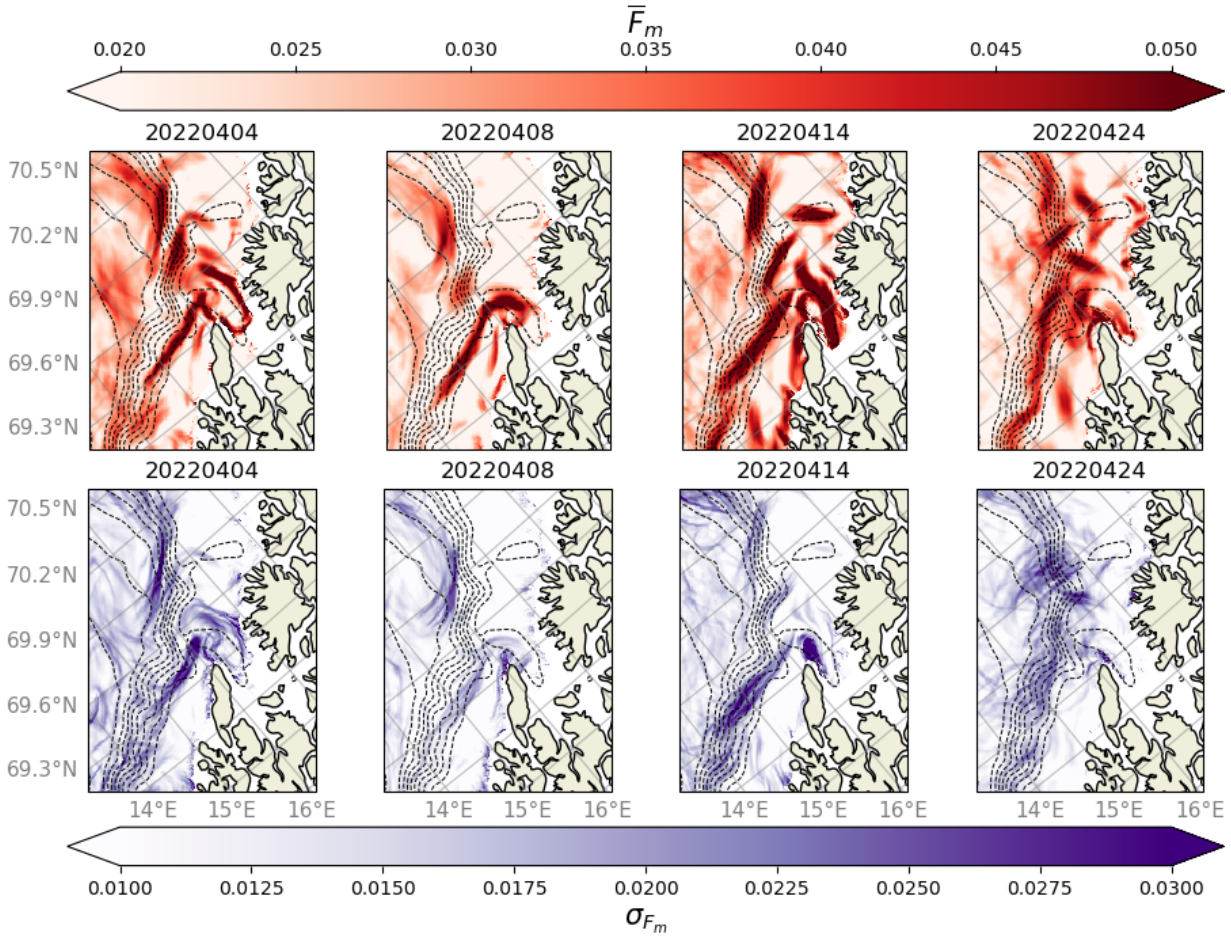

Figure 21: Zoom on the region highlighted by box 1 in Figure 20

The two highlighted regions in boxes 2 and 3 in Figure 20 also indicate distinguishable LCSs in the ensemble average. The extent of the LCSs in box 2 diminish over time, but is only accompanied by a high σ_{F_m} on April 4 which does not cover a larger region that $\overline{F}_m$. Therefore, the LCS in box 2 can be considered robust. The distinguishable LCS in box 3 appears to for the most part change shape between the dates, but all dates indicate large σ_{F_m} south of Vestfjorden, again signifying uncertainty in the position of this LCS across the ensemble.

The distinguishable nature of the LCSs highlighted in boxes 1-3 is a result of these being predicted similarly by the majority of ensemble members. The high σ_{F_m} in these regions for some dates is expected as even a slight perturbation in the LCSs between ensemble members can result in a high σ_{F_m}, as discussed in Section 3.7. It is therefore important to note that a high σ_{F_m} might not signify non-robust features if it covers a much smaller region than the average LCS itself, although a low σ_{F_m} indicates a high certainty. As such, the highlighted regions are considered to be robust for the particular dates.

4.2.4 Persistence of LCSs

The time-evolution of attracting hyperbolic LCSs is shown for ensemble member 0 in Figure 22. There are large changes over time in FTLE, both in the general amount of attracting LCSs and their position.

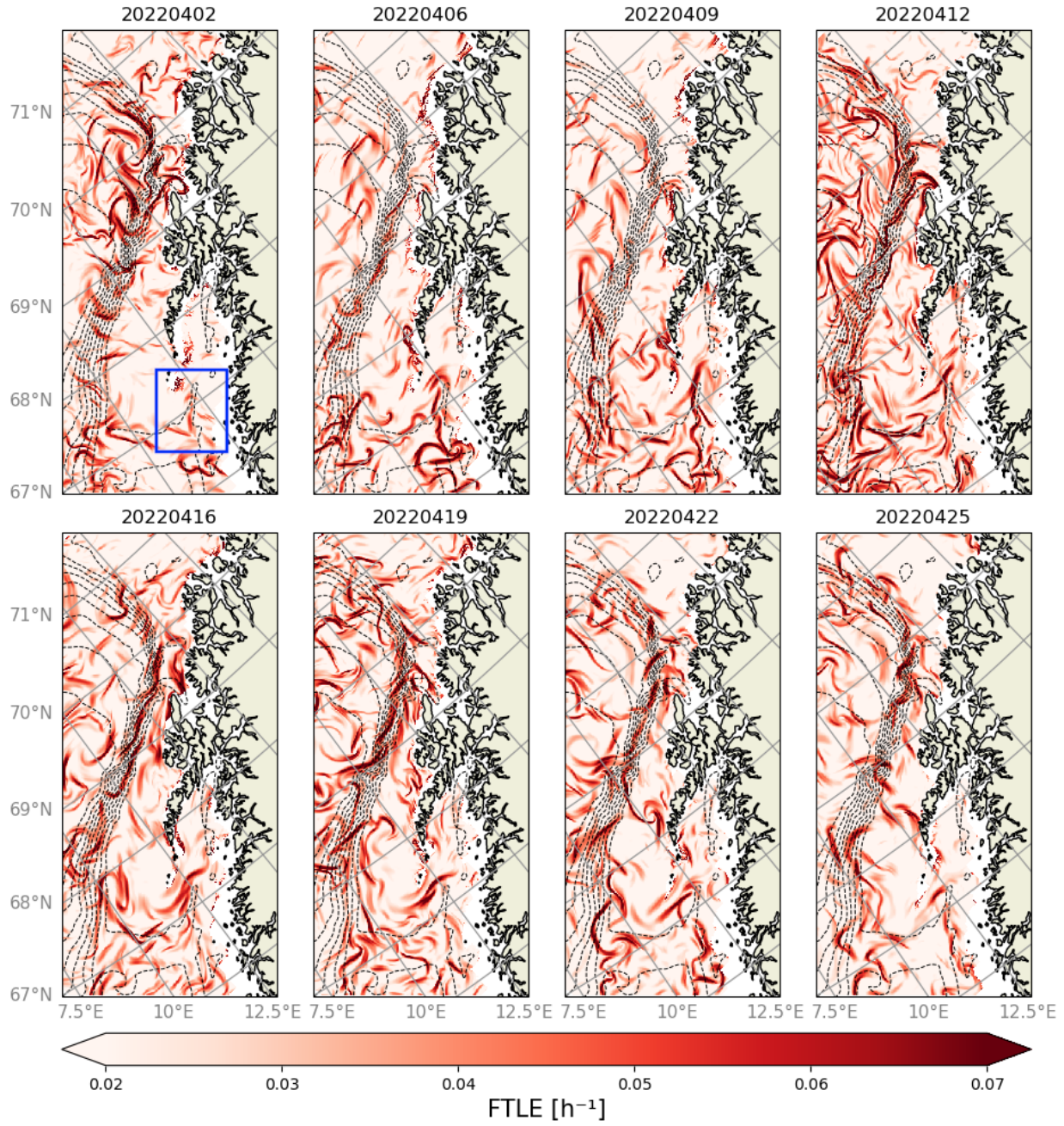

Figure 22: Attracting hyperbolic LCSs approximated with backwards FTLE over the Lofoten-Vesteråen region. High FTLE values are shown in red, whereas low FTLE values are show in white. The FTLE fields have been computed using velocity data from the first member of the Barents-2.5 EPS model, at eight different dates. Ocean bathymetry is indicated by dashed black lines. Blue box signifies a particular region of interest.

The first half of April shows the largest variability between the dates, where it can be seen that both the general position and number of LCSs is very variable over the first four dates, depicted in the top row of Figure 22. Most LCS activity is constrained to the northern part of the domain on April 2, but to the southern part of the domain on April 6 and 9. Then, LCS activity increases on April 12, where pronounced LCSs are seen to cover the whole domain. On the other hand, although LCSs change over the four dates in the second half of April, shown in the bottom row of Figure 22, their general positions appear to be similar over time.

Generally, LCSs can be seen to frequently form along the continental slope in April. Additionally, note the region south of Vestfjorden, highlighted by the blue box. Here, the LCSs appear to be similar to a certain degree over time and can potentially be persistent.

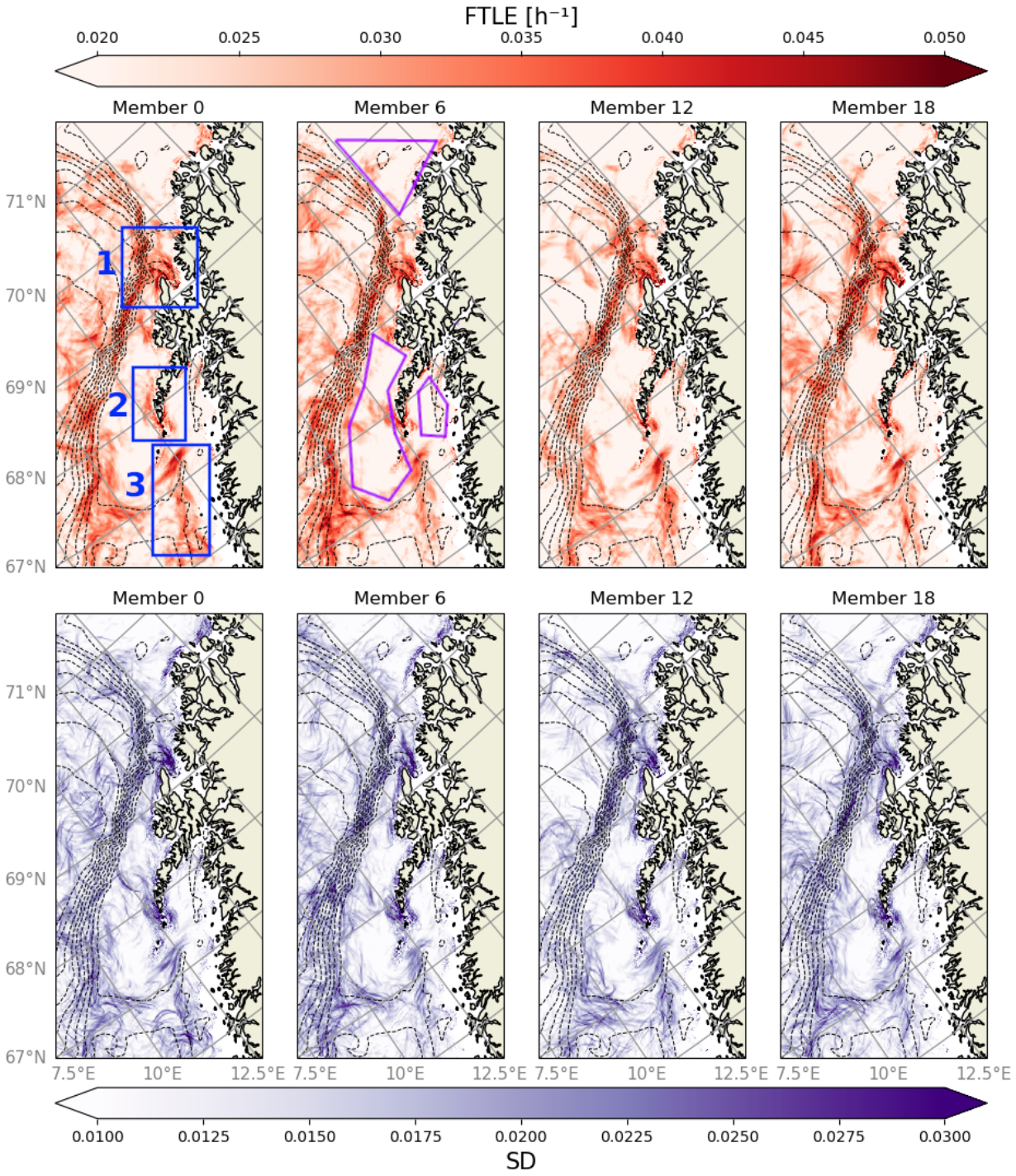

Figure 23: $\overline{F}_t$ (top row) and σ_{F_t} (bottom row) of LCSs over the month of April 2022, for four different members in the Barents-2.5 EPS model. $\overline{F}_t$ is colored in red, whereas σ_{F_t} is colored in purple. Bathymetry visualized with dashed black contours. Blue boxes highlight in member 0 highlight three regions of interest: 1) northern tip of LoVe, 2) southern tip of LoVe and 3) south of Vestfjord. Pink polygons in member 6 highlight three regions where there is little LCS formation.

The time averages $\overline{F}_t$ depicted in the top row of Figure 23 yields information about the persistence of LCSs in a complex dynamical system. The four top panels show that when averaging LCSs over a longer period of time, the position of $\overline{F}_t$ is very similar across ensemble members. Furthermore, immediately note that the smoothing of LCSs due to averaging is greater here than in the ensemble average. There are no clearly distinguishable LCSs in $\overline{F}_t$, as was the case for Figure 20 for the ensemble average.

There appears to be three distinct regions in the domain where $\overline{F}_t$ is small, highlighted with purple polygons in the panel of Figure 23 corresponding to member 6. These three regions signify locations where LCSs are less likely be formed over time. Furthermore, σ_{F_t} is small in these regions, indicating that it is virtually certain that there is little LCS activity inside the purple polygons over time.

From the figure it is clear that LCSs tend to form over the continental slope, where the surface current is strong on average and steered by bottom topography. Additionally, LCSs are shown to frequently form at the northern and southern tips of LoVe, as well as south of Vestfjorden. The coastline is always present, thus will have a similar influence on the currents over time and could influence LCSs similarly. However, the standard deviation σ_{F_m} is also shown to be large and cover a wide region over the continental slope and the highlighted regions. Any high $\overline{F}_t$ is accompanied by high σ_{F_t}, indicating that LCS positions are uncertain over time, although $\overline{F}_t$ indicates where they are most likely to exist.

4.2.5 LCS features generated by the deterministic tide

In Figure 24, the focus has been centered around the southern tip of LoVe, where the daily variability of LCSs is shown for ensemble member 0. To capture this variability, a data set containing LCSs with 2 hour integration times have been used, instead of the 24 hour integration time. Sea surface height (SSH) as a function of time on the same day is shown in Figure 24b. Tides are considered to be regular, in the sense that they can be modeled and predicted quite accurately.

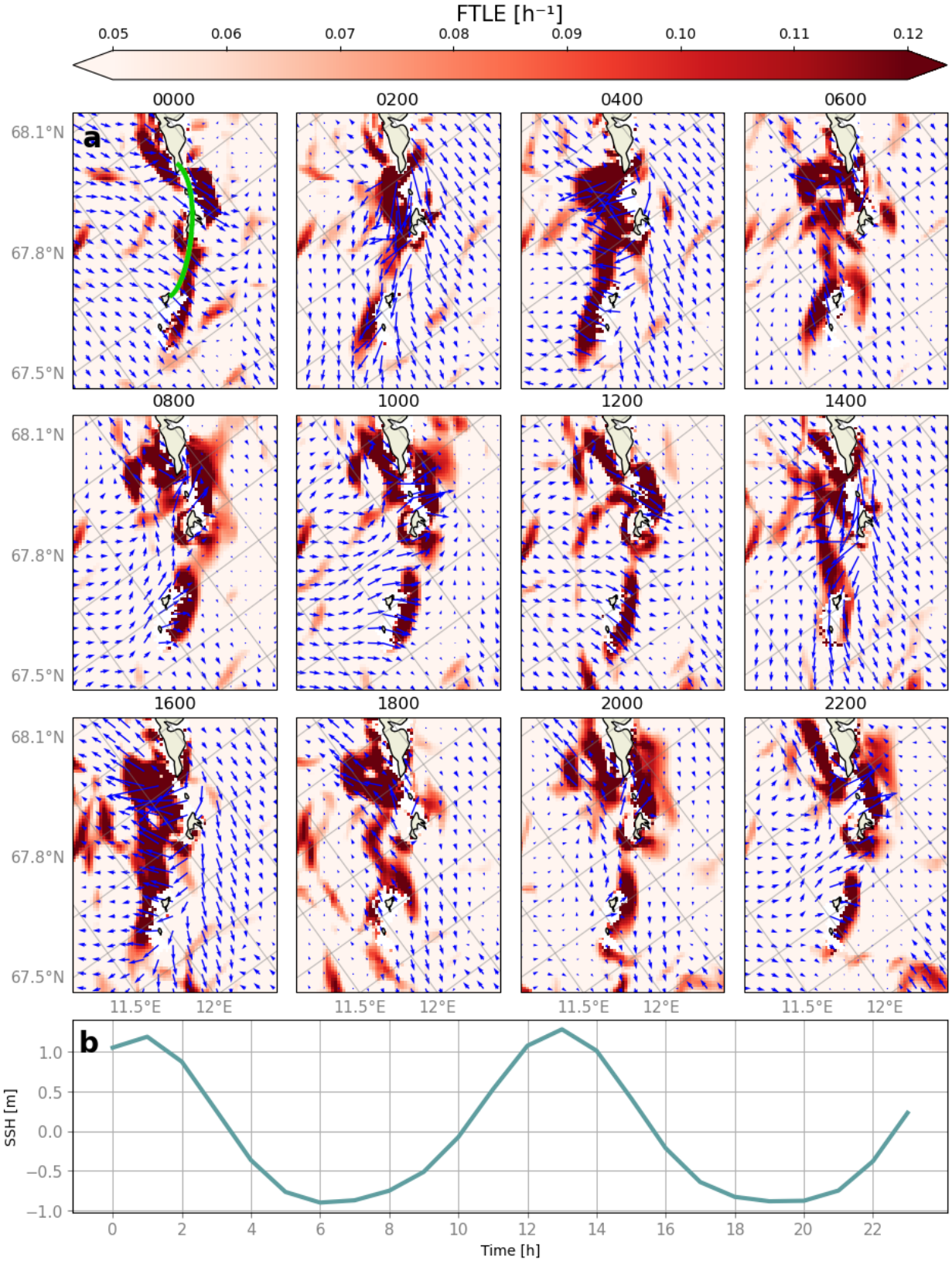

Figure 24: a) Attracting LCSs in red at 2 hour intervals on April 3, 2022, computed using the velocity field from Barents-2.5 EPS member 0. Green line represents an arbitrary line through the straits between the islands. Blue arrows represent the horizontal velocities. b) Time series of sea surface height for the regions, averaged over ensemble members.

The positions of LCSs in Figure 24a with regards to the islands indicate a clear response to SSH. The green line drawn represents an arbitrary line stretching through the straits between the islands. Ignoring the LCS to the left of the top island, which is always present in some sense or another, we focus on at which side of the green line LCSs generally tend to be found on. It can be seen that at 00 : 00, most LCSs are found on the eastern side of the green line. Then, between 02 : 00 and 06 : 00, LCSs are found on the western side. Every six hours, the LCSs appear to swap between east and west position with respect to the green line, coherent with SSH.

The horizontal velocities follow the same periodicity as the LCSs. It is seen in Figure 24a that the current periodically swap propagation direction through the straits on a six hour interval. LCSs are positioned on the east of the strait when currents propagate eastward and vice-versa. The current transports material from one side of the strait to the other, accumulating the material where the flow exits the strait. As such, material will converge around the strait exit, hence attracting LCSs will be predicted there.

Horizontal velocities and LCSs are shown to vary periodically. This periodicity is coherent with SSH. Figure 24 only show LCSs for one ensemble member, but a similar effect is seen in other ensemble members. Two different ensemble members are shown in Figures 33 and 34 in Appendix B. Thus it has been shown here that the tides can have an effect on LCS formation, at least around straits where the current propagation also depends on the tides.

4.2.6 Seasonality

Monthly average LCSs over all Barents-2.5 EPS ensemble members, as well as the corresponding density distributions, are shown for April and October 2022 in Figures 25a, 25b and 25e. In the northern section of the domain, north of LoVe, between the bathymetry contours and the coast, the April average predicts few LCSs. However, it appears that this same region is the most active region in the domain during October. From the distribution of FTLE values, it can be seen that the April average consists of higher values than the October average, but it seems that the few high FTLE values in October are mostly concentrated in the norther region.

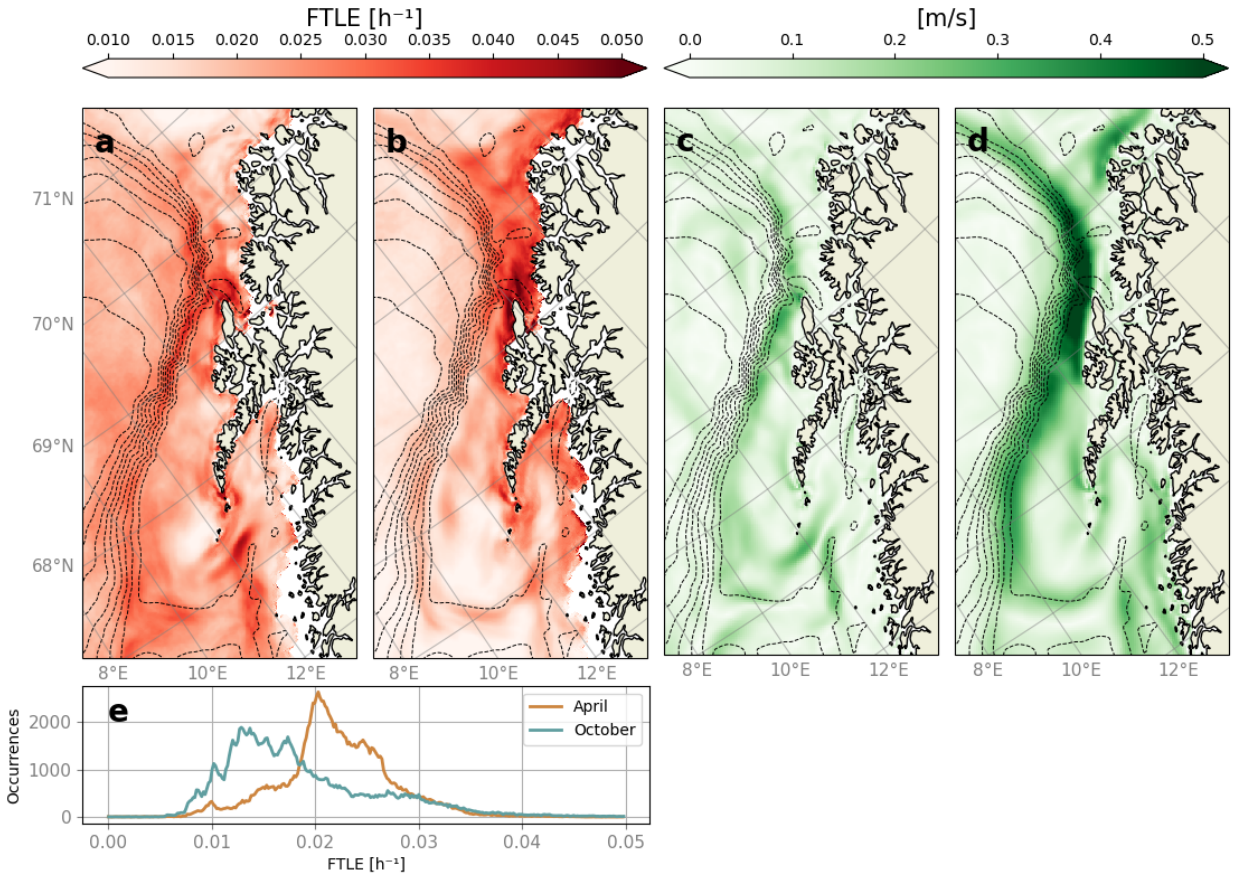

Figure 25: Attracting LCSs averaged over both time and ensemble members for a) April and b) October. Ensemble and monthly averaged absolute velocities, computed with $\sqrt{u^2+v^2}$ for c) April and d) October. Bathymetry indicated with black contours. e) The distribution of the FTLE values seen in a) and b).

The October average indicates that LCSs are for the most part only formed along the coastline. There is a small indication of LCS formation along the continental slope, but this is not a region where LCSs commonly form. On the contrary, the April average shows a smaller signal along the coastline, but much more frequent LCS formation over the continental slope. Additionally, October indicates almost no LCS formation to the west of the continental slope, whereas LCSs tend to form here regularly in April. Overall, it appears that LCSs form almost anywhere in the domain during April and only in concentrated regions close to the coast in October.

The FTLE distributions show that the April average has a sharp peek at 0.02h^{-1} and few values below this. On the other hand, October displays no sharp peek and most values are found in the range $\left[0.01\text{h}^{-1}, 0.018\text{h}^{-1}\right]$. At 0.03h^{-1}, the distributions appear to converge and the frequency of higher values than that appears to be approximately the same for both months. In general, the values seen in April are higher but the highest values, indicating locations where individual LCSs overlap often over time and ensemble members, are the same.

Monthly absolute velocity fields over all ensemble members for the two months are shown in Figures 25c and 25c. It can be seen that both months on average indicate strong currents along the continental slope. However, the currents appear to be stronger during October. Furthermore, the part of the NCC which flows into Vestfjorden appears to flow further into

Vestfjorden and closer to the coast in October. At the top of the domain, it can be seen that the current splits in October, indicating that the NwASC flows westward following the westward curvature of the continental slope, whereas the NCC continues flowing along the coastline. Finally, although there are stronger currents in October, April indicates a higher amount of weaker small-scale structures in the domain, especially west of the continental slope. Figures showing LCSs in different members and for different times, as well as $\overline{F}_m$ and $\overline{F}_t$ for October can be found in Appendix B.

5 Discussion

LCSs are seen to be highly variably across both ensemble members and time. However, potentially robust and persistent LCSs have been identified. In this section I will discuss the following: i) whether LCSs computed with my own detection software have an impact on particle trajectories, ii) whether the parameter choices I have made have drastic implications on computed LCSs, iii) potential causes for robustness and iv) potential causes for persistence.

5.1 Applicability of LCS detection method

The resulting LCSs of the analytical double-gyre system is well-studied in literature (Shadden et al., 2005). The quickest verification method for my LCS detection software is therefore to compare my double-gyre solutions to previous studies. Figure 3a of Froyland and Padberg-Gehle (2012) and Figure 3 of Fuchs et al. (2012) are two previous examples of double-gyre LCSs. Here, the authors also use the FTLE detection method, albeit they compute *repelling* hyperbolic LCSs, and use different parameters for the system itself. I have therefore computed repelling LCSs in the double-gyre system using the same parameters as the authors, which can be found in Figures 30 and 31 in Appendix A for the two studies respectively. As it can be seen, the results are fairly similar, thus my detection software is consistent with previous works.

Attracting hyperbolic LCSs act as transport barriers and accumulation regions for material transport. Experiments were conducted to verify these properties of LCS, which can be seen in Figures 13 and 18. Overall, particle trajectories show an overall agreement with LCSs. The largest difference between these two experiments is that the double-gyre system always contains two gyres which move periodically, whereas the Barents-2.5 velocity field is turbulent and chaotic. As previously mentioned, flow structures, such as eddies or fronts located in this region (see e.g. Koszalka et al. (2013); Isachsen (2015); Trodahl and Isachsen (2018)), constantly emerge and dissipate in Barents-2.5 and LCSs can do so just as quickly. Therefore, the LCSs detected in the Barents-2.5 experiment may all be fairly ephemeral and particles could have previously been affected by which existed at previous times.

Note that Barents-2.5 is a 3D model, whereas the double-gyre is strictly 2D. I used massles particles in these experiments and forced these to stay at the ocean surface in the Barents-2.5 velocity field. However, the model includes 3D velocities. Hence, the flow in Barents-2.5 is not 2D divergentless. Convergence or divergence of the surface flow will cause vertical velocities to conserve 3D volume transport. Assuming that a particular LCS transport barrier only exists at the surface, vertical motion could allow particles to simply flow beneath this transport barrier. As the double-gyre is strictly 2D, this is not an issue as mass is always conserved.

First looking at the experiment in the double-gyre system, it is apparent that particle trajectories are in fact shaped by the closest attracting LCS. Particles start off in a cluster and spread out along the underlying LCS without actually crossing it. LCSs are therefore seen to prevent mixing between the green and blue particles. In this system, the particle cluster acts exactly like in the simple schematic of attracting LCSs in Figure 2, in which the theorized properties of LCSs are shown. LCSs work well as a proxy for revealing dynamical constrains on the trajectories in the double-gyre and more prominent LCSs indicate locations

where particles are more likely to reside.

The experiment conducted using velocity fields from the Barents-2.5 model yielded a weaker indication of LCS influence on trajectories than the double-gyre experiment. The clusters edge takes the shape of the outlining prominent LCSs, whereas the inner particles which are positioned far away from any prominent LCS at the final date appear to be less influenced by them. Inner particles might simply exist too far away from any dominant LCSs for them to have any effect. More particle trajectories could potentially be shaped by the LCSs given a longer integration time. Some regions inside the particle cluster appear to have a higher particle concentration at the final time. There are no apparent underlying LCSs here at this time, but these higher concentration regions could be a result of LCSs which existed prior to this date.

The LCSs indicate a transport barrier along the continental slope. This transport barrier is constructed from multiple LCSs with some separation in between, thus gaps in the transport barrier are present which particles should be able to flow through. Even so, the particle positions indicate that the transport barrier have retained particles at the continental shelf.

5.2 Impact of parameter choice on FTLE computations

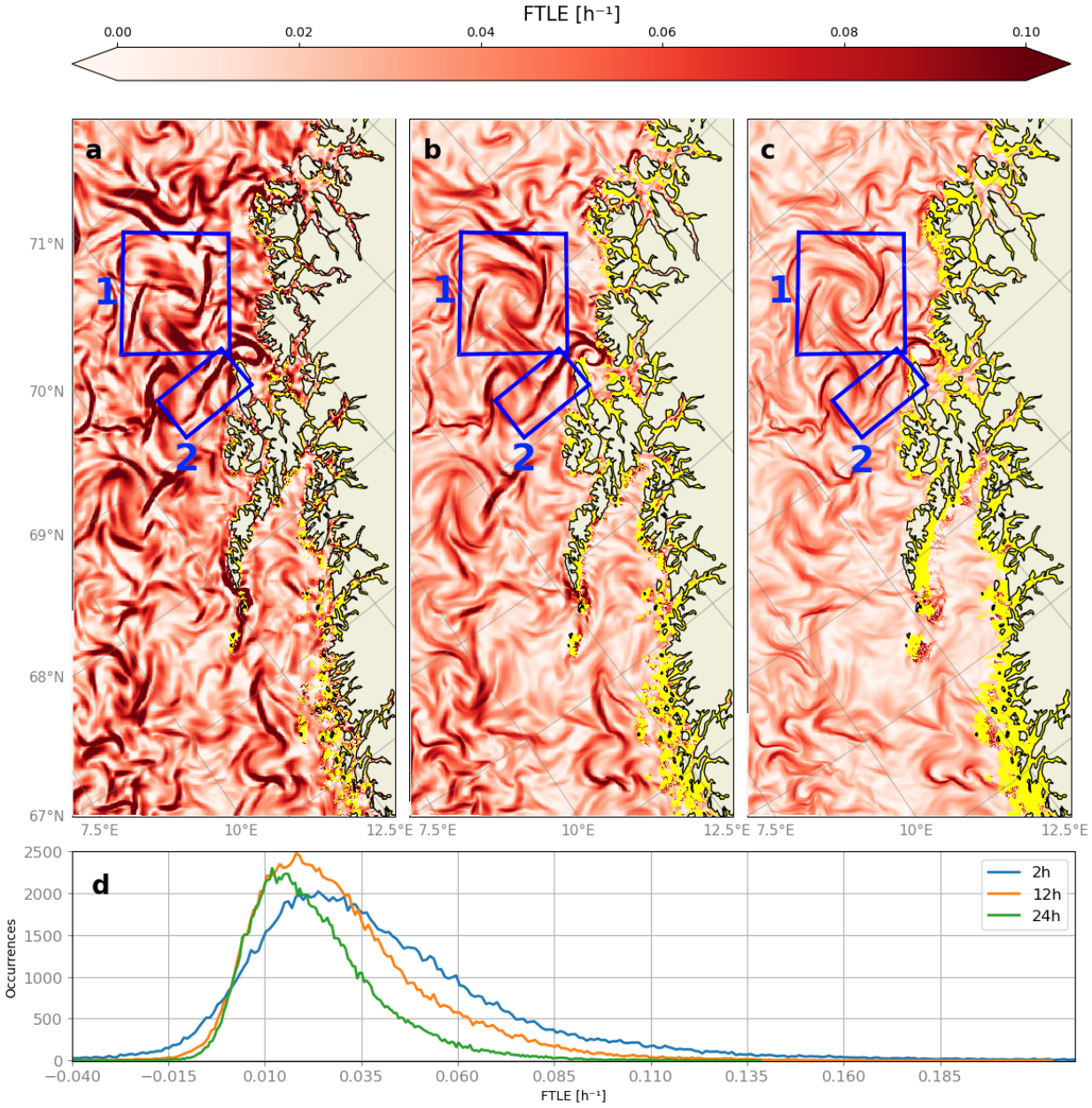

Figure 26: FTLE integrated over a) 2 hours, b) 12 hours and c) 24 hours. Three regions of interest are highlighted with blue boxes. Yellow regions near the coast signify grid cells without FTLE values. d) the distribution of FTLE values in the domain for the three integration times.

A choice was made regarding the time interval LCSs were computed over. This time interval is set to 24 hours in all results except for when studying daily variability, where it is set to 2 hours. Particles are integrated over this time interval by Eq. 26. The question is whether the choice of integration time significantly changes the resulting LCSs. LCSs computed for the same target time, but integrated over three different time intervals, are shown in Figure 26. An increase in integration time appears to lower FTLE values, which can be explained by Eq. 19, as there is a division over the integration time. This can be considered as a scaling factor which does not directly impact the shapes and positions of LCSs, however, for longer integrations the computations might be affected by short lived LCSs.

LCSs appear to be thinner and more defined for higher integration times. This is most likely due to the FTLE method aiming to approximate LCSs, which are really infinitesimally thin curves, with fields of attraction/repulsion around these thin curves. Increasing integration time allows the grid of particles used for the computations more time to spread into distinct structures. Take for instance the LCS inside box 2 in Figure 26, which appears to be one thick curve when integrating over 2 or 12 hours, but appear as two thinner curves when integrating over 24 hours. This shows that thick LCSs detected using the FTLE method could consist of multiple thin LCSs. Therefore, allowing the grid of particles to drift for longer can reveal a larger number of LCSs, which can have implications on my results. Additionally, as the field is thicker, it might cause two short LCSs to connect into one long. Thus creating a seemingly long transport barrier, when in reality there are gaps in this transport barrier, such as the LCS directly above the box 1. However, a longer integration time also makes the particle grid uneven.

The actual positioning and shape of LCSs appear to be mostly similar for the different integration times, although some discrepancies can be found. For example, note the circular shape of the LCS outlined by box 1 at integration time 12 and 24 hours. These resemble a vortex of some sort, similar to what can be seen in Figure 4. However, this circular shape is harder to distinguish at integration time 2 hours. Similarly to before, this can again be due to the grid of particles not having enough time to drift into the ordered patters they are supposed to end up in. This could cause errors in how the LCS and the flow field they describe are perceived.

Yellow regions near the coastline in Figure 26 highlight regions without FTLE values. It is apparent that the extent of missing values increases with increased integration time. The advection model described in Section 3.4 is set up so that advected grid particles which collide with the coastline are removed from the system. This conscious choice is made because there is no flow through land, thus allowing for particle propagation here is not realistic and could yield large errors near the coast. Subsequently, particles generally propagate a further distance with increased integration intervals, allowing more particles to collide with the coast. The missing values cause information to be lost along the coast, where there can potentially be high robust and persistent activity, but have no impact LCSs in the open ocean.

The distributions of FTLE values in the domain for each integration times are shown in Figure 26d. All three appear to be similar to Rayleigh distributions. The distributions show that there is a larger spread in FTLE values for shorter integration times. With increased integration times, both fewer high values and lower maxima are seen. Following the observation that FTLE values decrease with an increase in integration time, the peak of the distributions also shifts towards lower values with longer integration times.

The distributions show that there are more negative values for shortern integration times. A negative FTLE value over a region means that the dynamical system of this region is locally non-chaotic (Alimi et al., 2021). Furthermore, Eq. 18 implies that if the FTLE value is $0h^{-1}$, then $|\delta_t\| = \|\overline{\delta_0}\|$, and there is a steady state. As there are less negative values with higher integration times, the negative values that appear at 2 hours might not actually tell the whole picture. For backwards in time integrations, two particles can converge for a short time, which yields negative FTLE values forward in time. However, when integrating over a longer time period, it is revealed that the particles only converged initially and started separating afterwards, thus yielding positive FTLE values forward in time. Longer backwards in time integrations can integrate over these short backwards in time convergences

and particles diverge on average over backwards-time, yielding more positive FTLE values forward in time.

Increasing integration time allows for distinguishing separate attracting LCSs, as well as structures in the domain, although information along the coast is lost. An increase in integration times also yields less negative values, thus there are less non-chaotic regions in the system.

As stated in Section 3.3, the Barents 2.5 EPS has a 2.5 km$\times$2.5 km horizontal resolution. As a result, smaller structures are not predicted by the ensemble. This means that even though there exists a small eddy, which could potentially give rise to a prominent LCS, this eddy is not captured by Barents 2.5. EPS. An eddy of size 5 km would also just be represented by two grid cells, which would probably not result in significant LCSs. I made a conscious choice to interpolate the grid down to 1000m $\times$ 1000 m with linear interpolation. This still does not allow the model to detect structures lower than its original resolution. Instead, it smooths the velocity field, so the transitions between grid cells are more continuous, as required in section 2.1.1.

Finally, the FTLE detection method itself can have an effect on resulting LCSs. Multiple methods have previously been studied for detecting these structures and can yield different results. It is therefore not given that the FTLE method is the best for this particular study, even though this is one of the more common approaches in practical studies, alongside the Finite-Size Lyapunov Exponent. Furthermore, the software only visualizes the general strength of attraction using the largest eigenvalue of $\boldsymbol{C}_{t_0}^t$, and not the direction of said attraction. Another approach would be to compute strainlines from the largest eigenvector of $\boldsymbol{C}_{t_0}^t$ to solve for the direction of deformation (Farazmand and Haller, 2012).

5.3 Uncertainty of LCSs in flow field

5.3.1 Double-Gyre ensemble

Given the inherent velocity field uncertainty and the implications they have on other Lagrangian methods, LCS sensitivity to variations in the velocity field have been tested. A simple double-gyre ensemble has been computed and shown in Figure 15. This allowed for testing implementations in a fully controlled system and an ensemble average has been attempted as a method for detecting robust LCSs.

As shown in Figure 15, variations between the velocities are marginal in the double-gyre ensemble. The only visible difference in the velocity fields is the position of the conflux. However, LCSs immediately exhibit noticeable differences between the ensemble members. This tells us that LCSs are more sensitive to parameter perturbations.

As seen in Figure 13, LCSs do not form or dissipate in the system. Instead, the LCSs simply move around with the flow. It can therefore be assumed that the LCSs in the system are persistent, although they move around and change shape. However, if we would conduct a time average over the double-gyre system, we would most likely not detect any persistent features in $\overline{F}_t$, as the positions of LCSs constantly change.

Four distinct LCSs have been considered to be robust in the double-gyre ensemble, as they are present in all ensemble members. Particularly, the LCS located at the conflux appears to be the most robust feature of the system, only varying slightly in position and length.

The length of the conflux length dependent on the ϵ parameter and it is shown in Figure 32 the conflux LCS spans across the entire y-axis with $\epsilon = 0$, thus forming a complete transport barrier between the two gyres. The remaining three LCSs are seen to vary to a larger degree.

The ensemble average, $\overline{F}_m$ and standard deviation, σ_{F_m}, are shown in Figure 16. $\overline{F}_m$ has been able to indicate three of the four selected LCSs, although the LCSs have been smoothed. $\overline{F}_m$ now indicates regions where LCSs are generally formed. Furthermore, σ_{F_m} yields information about the spacial spread of LCSs. Higher and more concentrated values in $\overline{F}_m$ are most likely due to LCSs overlapping, which causes σ_{F_m} to be small. This signifies that both the existence and positions of LCSs are certain, and is seen to happen around the constant boundaries and at the conflux. $\overline{F}_m$ might show a strong indication of LCS formation, but σ_{F_m} can also be large in these regions. This means that there is a high certainty that there exist LCSs inside the region of $\overline{F}_m$ in question, but their exact position is unknown. It has also been shown that in some cases, LCSs are present in the ensemble, but not indicated by $\overline{F}_m$. It is still possible to reveal these LCSs them with σ_{F_m}. The ensemble average and standard deviation has proved useful in identifying robust features in the simple ensemble.

5.3.2 Ocean ensemble

Velocity fields in Barents-2.5 EPS indicate a more variable flow field than the double-gyre ensemble. This higher variability is reflected in the LCSs, where clearly distinguishable structures appear to vary to a large degree in both position and shape. This emphasizes the importance of an EPS. An LCS predicted by one member might not be present in any other member, thus making this LCS highly uncertain to exist.

Averaging over ensemble members has been conducted as a method for detecting robust features. As can be seen in Figure 20, $\overline{F}_m$ smooths out the LCSs, resulting in regions where LCSs are more likely to be formed, rather than thin curves. However, some LCSs are still clearly distinguishable, particularly around the northern and southern tips of LoVe and south of Vestfjorden, where currents are influenced by geomorphology.

Due to the averaging, the curves representing LCSs have become thicker. However, for them to still exist as distinguishable curves in $\overline{F}_m$, most ensemble members must have predicted LCSs at almost the same locations. This is further emphasized by σ_{F_m}, which indicates some variation between ensemble members where there are prominent $\overline{F}_m$ curves, but σ_{F_m} rarely covers a particularly larger region than $\overline{F}_m$.

Few pronounced LCSs are generally seen in $\overline{F}_m$ over the continental slope. Rather, smoothed regions in $\overline{F}$ appear here. σ_{F_m} also indicates high variability along the continental slope. This suggest that it is certain that LCSs are formed along the continental slope, but their exact positions here are highly uncertain between ensemble members.

Generally speaking, regions which indicate the highest LCS formation are situated where large scale geological features are present, i.e. along the continental slope and coastlines. As attracting LCSs indicate regions where convergence between particles is largest, LCS formation is less dependent on current strength, but rather the direction of the current. A homogeneous straight current will most likely not attract material in any particular location, no matter its strength, as all particles will flow in the same direction at the same rate. For distance between particles to change, the current needs to be variable, e.g. by curving or having flow structures break off the main current. Here, the importance of these geological

features with regards to robustness comes to light, as they will steer the current flow in a similar manner over ensemble members.

The robust LCS feature at the southern tip of LoVe is most likely formed due to the curvature of the NCC around the southern tip. It is well known that the NCC splits into two parts south of Vestfjord, where one part flows into Vestfjord and follows the coastline on its right side to a large degree, thus ends up curving around the southern tip. This apparently causes material to converge towards the southern tip of LoVe.

This current curving inside of Vestfjord could also explain the robust LCS directly south of Vestfjord. Here, the LCS is situated in a region where there is both a northward and southward flowing current. Therefore, any mixing and turbulent flow is bound to happen here. The currents then flow northwards alongside the LoVe coastline, but when this coastline suddenly disappears, a part of the current is steered eastward and curves around the northern tip. As there is bottom topography which curves around the northern tip, these most likely have an influence on the eastward steering of the current as well. Similarly to the reasoning for the southern tip, this curvature of the current along the northern tip could be a driving factor for enhanced LCS formation here. As this happens in all ensemble members in some form or another, these regions appear to be robust.

The reason for less positional certainty along the continental slope is most likely due to a more variable current in this location between ensemble members. The current is steered by the bottom topography, but not by the coastline. This bottom topography causes some curving and turning of the current, and small scale structures break off from the main current due to baroclinic instability. However, the chaotic baroclinic flow is most likely not as robust as the current steering along the coast of LoVe. This in turn causes more positional uncertainty in LCS formation here than along the coastline.

Because of the existence of clearly defined LCSs in $\overline{F}_m$, I can assume that averaging over ensemble members does yield and indication for robust LCSs. For some regions, where there is a large positional spread in LCSs, $\overline{F}_m$ can only indicate the approximate region where these are formed. This results in a smoothed region of higher FTLE values. In other regions, where the ensemble members agree to a larger degree, $\overline{F}_m$ takes the form of thick curves with high FTLE value, which in turn is where the most robust LCSs are found, as this is caused by ensemble members agreeing on the position of LCSs to a large degree. Certain robust LCSs can be distinguished.

5.4 Temporal variability of LCSs

Persistence is defined as LCSs which exist over a longer time period and can vary over different time-scales. A flow feature might be persistent over one month, but maybe not over the whole year. I divide this section into three parts: 1) daily persistence, 2) persistence over the month of April and 3) seasonal persistence.

5.4.1 Daily variability

A tidal dependency of LCSs has been investigated around the southern tip of LoVe, seen in Figure 24. This is where Moskstraumen is situated, which exhibits the regions strongest tidal pumping (see Figure 3) (Børve et al., 2021), along with other similar currents which

form in between straits. The east-west position of LCSs appear to be dependent on which direction these strait currents flow, i.e. if the current flows westward then LCSs are on the west side and vice versa. The periodic tidal pumping sets the current directions and causes material to be transported through the straits.

As the tidal pumping causes strong material transport through the straits, the particles advected to compute LCSs should also be transported through this strait. Therefore, particles should accumulate on either side of the straits, based on the current direction, which in turn results in detected LCSs. However, as this is a region close to the coastline, some of the grid particles will collide with the coast and result in some missing information. Furthermore, the distance between these islands is small compared to the resolution of the Barents-2.5 EPS model, thus there are only a couple of model grid cells in between each island. This, in addition to the 2 hour integration time which has been shown to cause thicker LCSs, result in LCSs in this region which are of low resolution. It is therefore almost impossible to distinguish any distinct turbulent flow structures from LCSs alone. The LCSs here tell more about the position of the accumulation zones with regards to the straits.

Nøst and Børve (2021) investigate the details of a tidal current as it passes through a strait. The authors state that as the current exits the strait, the pressure gradient force and friction from the coast will work in the opposite direction of the flow, decelerating the flow. This can cause flow separation and a vortex forms at the separation point. The flow can also separate at both sides of the strait exit and two vortices with opposite signs are formed, as seen in Figure 27. These two vortices can then form a self-propagating dipole.

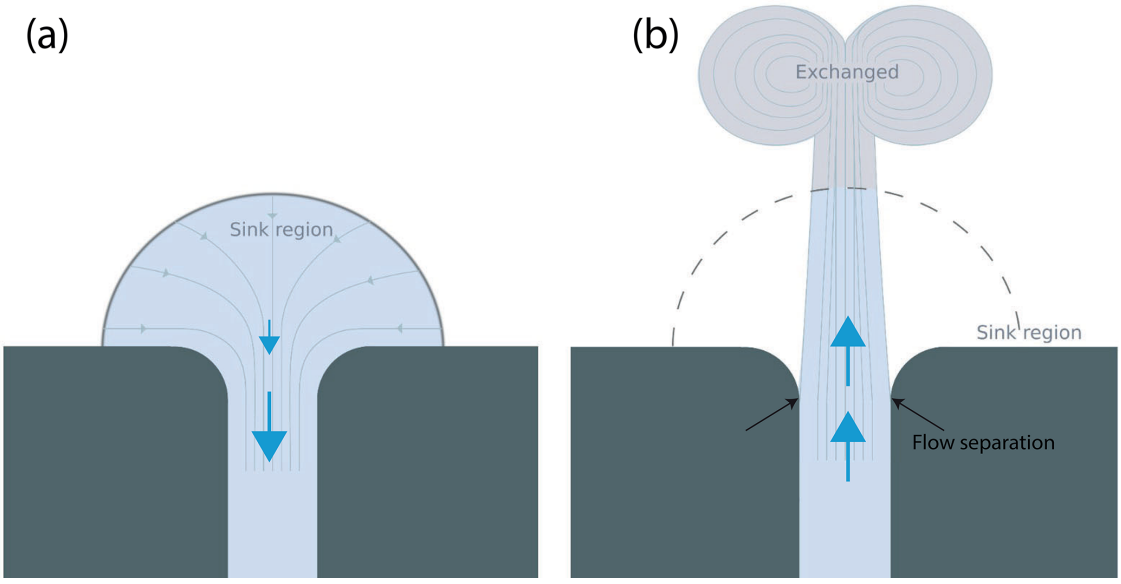

Figure 27: Figure 1 of Nøst and Børve (2021). A schematic of the current flow through a strait due to tidal pumping. a) flow into the strait. b) flow out of the strait.

This simplified description of the flow resembles the double-gyre system from Section 3.1. Similar LCSs as those seen in Figure 15 might therefore appear on around the straits. However, there is no indication of these in Figure 24. This could be because the double-gyre is a heavily simplified description of this flow, or that the resolution of the model is not high enough. Even so, there is a clear indication of periodicity of LCSs along the straits which is caused by tidal pumping.

5.4.2 Monthly variability

LCS variations in April 2022 can be seen for member 0 of the Barents-2.5 EPS in Figure 22, whereas the monthly time average, $\overline{F}_t$, can be seen for multiple ensemble members in Figure 23. It has been shown that there is a large variation over time in LCSs. This is further reflected in $\overline{F}_t$, where there are no clearly defined curves representing average LCSs. Rather, everything has been smoothed out. This means that there exists no LCSs in the domain which stay in one location for a longer time. This is expected, as the LCSs are time dependent and can either drift, emerge or dissipate over time.

One exception could be the LCS south of Vestfjorden, which resembles a smoothed out curve. Looking back at Figure 22, this LCS is present at almost all time steps and only indicates a small perturbation over time. This implies that the velocity field is rather persistent in this location over time. However, $\overline{F}_t$ still appear as a smoothed curve and not a very distinct curve, indicating variability. This is further reflected by σ_{F_t}, which indicate high positional variability south of Vestfjorden.

The southern tip of LoVe also showcase persistent LCS formation. However, σ_{F_t} surrounds the whole southern tip. As such, σ_{F_t} indicates that it is uncertain which side of the southern tip LCS are formed on. It almost appears as if LCSs can swap what side of this tip they are on. This variability can be caused by tides, as discussed in Section 5.4.1.

No clearly distinct persistent LCSs were detected by the monthly time average. However, $\overline{F}_t$ yields an indication over where LCSs frequently tend to form. Any high $\overline{F}_t$ is accompanied by a σ_{F_t}, thus the variability over time is large. A different approach for detecting persistence could be proposed, e.g. by selecting a particular LCS and studying how it evolves over time. The LCSs lifetime, propagation distance, growth/dissipation-rate and shape evolution can then be studied. There could be a connection between the size of an LCS and its longevity.

Dong et al. (2021) avoided averaging when studying the persistence of the transport barrier along the continental slope. Instead, the authors defined a set of criterion for the existence of this transport barrier and investigated the frequency of the criterion being fulfilled. I see frequent LCS formation along the continental slope in $\overline{F}_t$ that could be an indication of the transport barrier in Dong et al. (2021). It is therefore plausible for this transport barrier to exist in Barents-2.5 EPS as well, which had a finer spatial and temporal resolution than the geostrophic current product used by Dong et al. (2021). However, the authors computed *repelling* LCS using the Finite-Size Lyapunov Exponent, which generally do not coincide with LCSs from the FTLE method by Karrasch and Haller (2013). Hence, we are technically investigation different LCSs. Furthermore, separate LCSs are indistinguishable in $\overline{F}_t$. As discussed in Section 3.7, it is uncertain whether $\overline{F}_t$ consists of a few long, continuous and long-lived LCSs along the continental slope, forming a transport barrier, or many short and short-lived LCSs that material can drift between.

5.4.3 Seasonal variability

The seasonal differences between April and October are shown in Figure 25. Here, an average over both time and ensemble members has been conducted, hence the LCSs are smoothed out. LCSs are seen to form in very different locations for the two months.

The current velocities are shown to be higher in October, likely due to an increased baroclinic component of the flow as discussed in Section 3.2. Furthermore, Figures 25c and 25d

indicates that the part of the NCC that flows into Vestfjorden flows closer to the coastline during October. There is a correlation between the average monthly velocities in Vestfjorden and the average LCSs, as average LCSs south and inside of Vestfjorden lay practically on top of the average velocities for the two months.

The correlation between LCS and velocity field positions is not as apparent along the continental slope. It has been shown that there is a frequent LCS formation along the continental slope in April, where the NwASC flows. However, there is practically no LCS formation in the same region in October, even though the NwASC is still situated in the same location. The ocean experiences surface heating during summer, which in turn makes the ocean more stratified in October than in April, meaning that bottom topography has a larger impact on surface currents in April. This decreased topographical steering in October could yield less turbulent flows and small-scale flows which break off the main current, leading to less LCS formation along the continental slope.

The increased appearance of LCSs in October between the continental slope and mainland, north of LoVe, could be explained by the average current. There is a much more pronounced splitting of the current here in October than in April. A splitting of the current could potentially cause some turbulent flows which could give rise to LCSs, although this would have to be investigated further to ascertain. On the other hand, April indicates more LCS formation west the continental slope. Again, the currents shown in Figures 25c and 25d indicate more activity here during April, which could explain increased LCS formation.

Both months indicate high LCS activity along the northern and southern tip of LoVe. The currents should be affected similarly by the coastline for the two months. Thus the coastlines is important for LCS formation throughout the whole year.

The overall behaviour of LCSs depends on season. Driving factors could be different wind velocities, which exert different wind stress, current velocities and ocean stratification. Dong et al. (2021) showed that there is a persistent LCS which appeared in April over multiple years. As LCSs change depending on season, there could be an annual dependency on LCSs as well. LCSs should therefore be studied for other months over multiple years to investigate whether there is an annual trend in LCS formation for each month. Further investigation for seasonal dependency and causes could be addressed in future studies.

5.5 Robustness and persistence

Both $\overline{F}_t$ and $\overline{F}_m$ show enhanced LCS formation along the northern and southern tip of LoVe, south of Vestfjorden and along the continental slope, seen in Figures 20 and 23. As a result, these regions can be considered both robust and persistent. A common factor is that the flow in these regions is steered by geomorphological features. As these are constant over both ensemble members and time, it stands to reason that they exhibit both persistence and robustness.

The region on the continental shelf of LoVe is known for high nutrient concentrations (Sundby et al., 2013). LCSs are shown to frequently form along the continental slope, both over time and ensemble members, which could form a transport barrier. This could explain why nutrients are usually retained in this region.

Both averages also indicate that there are LCSs present in the deep ocean basin, west of the continental slope. This region exhibit a higher degree of smoothing than the four

aforementioned regions from the previous paragraph. This signifies that the LCSs here are neither robust nor persistent, therefore the position and shape of LCSs in the deep ocean basin are highly uncertain.

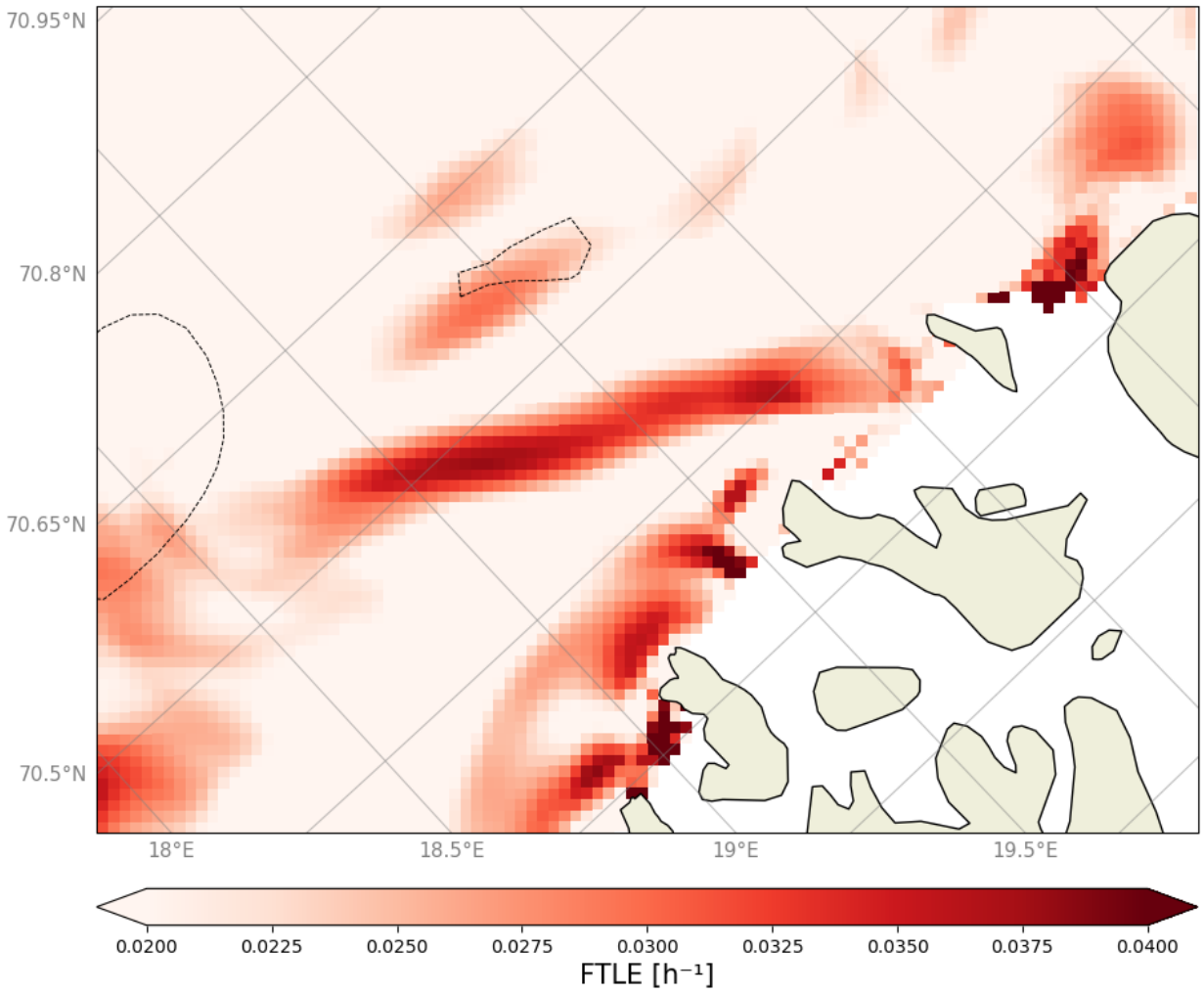

Figure 28: Zoom on the thin but distinguishable structure in $\overline{F}_m$ from Figure 20. This structure is found in the top region of the LoVe domain on April 14, 2022.

There are some features which appear to only be robust, not persistent. An example of one such feature is the thin LCS seen in the top of the domain on April 14, which has been enlarged in Figure 28. Here, a thin and distinguishable LCS is present in $\overline{F}_m$, which is not present on any of the other dates. The fact that this LCS is so thin, compared to many of the other thick LCSs in $\overline{F}_m$, signifies that most ensemble members predicted this particular LCS to exist at this exact location on this day. This is further confirmed by σ_{F_m}, which indicates little to none variability around this LCS. This LCS is completely gone in $\overline{F}_t$. Thus it is robust for the particular date, but not persistent.

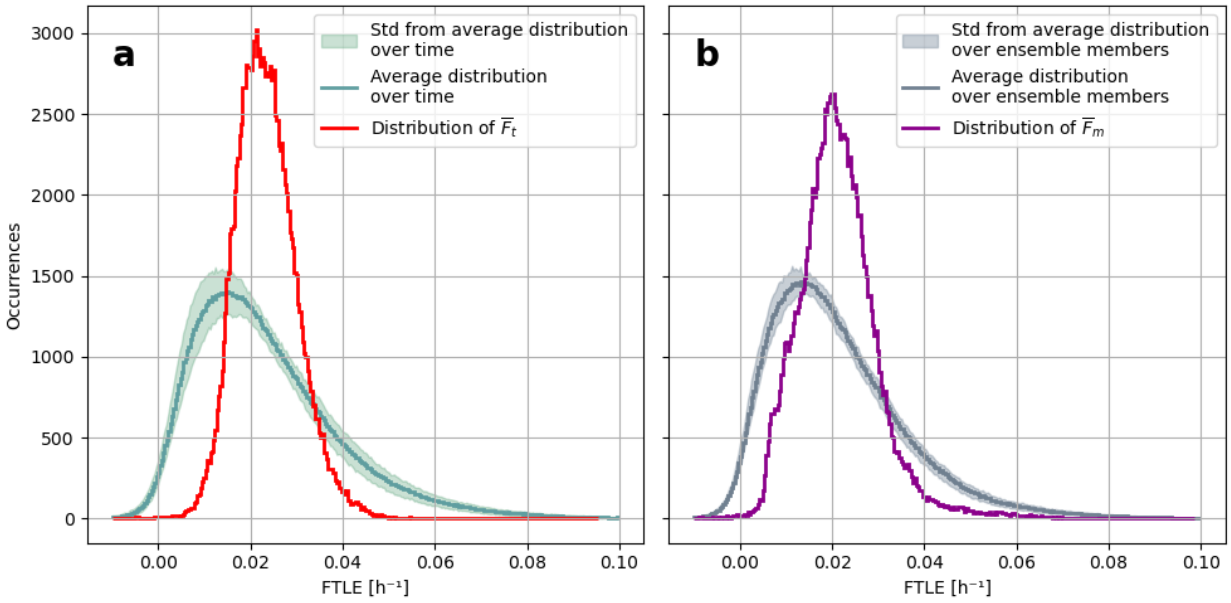

Figure 29: Distributions of FTLE values in the LoVe domain. a) distribution for ensemble member 18 in the Barents-2.5 EPS over time. Red graph is the distribution of $\overline{F}_t$, whereas the green graph depicts the average distribution in the domain over time. Green shaded region shows the standard deviation from the average over time. b) Distribution of FTLE values on April 4, 2022, for all ensemble members in the Barents-2.5 EPS. Purple graph is the distribution of $\overline{F}_m$ at this time, whereas the gray and light-gray show the average distribution over ensemble members and standard deviation from this average respectively.

Generally, the time average $\overline{F}_t$ is smoother than the ensemble average $\overline{F}_m$, as seen in Figures 20 and 23. This is also reflected in the standard deviations, where σ_{F_t} is larger and has a wider spatial extent than σ_{F_m}. This signifies that there is a larger variability over time than over ensemble members. Another way to look at this is through the distribution of FTLE values in the domain, shown in Figure 29. Here, the distributions in Figure 29a represent FTLE values at different times for ensemble member 18, whereas the distributions in Figure 29b are FTLE values for all ensemble member for a selected date. These distributions yield information about the FTLE values, but do not yield information about position of LCSs and the values are dependent on parameter choices as discussed in Section 5.2.

The most frequent FTLE values for the individual times and ensemble members are centered around $\approx 0.017h^{-1}$ in Figure 29. Attracting LCSs of interest in Figures 19 and 22 all have values higher than $0.05h^{-1}$. The central value in Figure 29 therefore signifies negligible LCSs or the space between two LCSs. From the distributions it can be concluded that higher FTLE values, therefore also more dominant LCSs, are less likely to occur in the system.

The individual distributions resemble some form of Rayleigh distributions. However, the distributions of $\overline{F}_m$ and $\overline{F}_t$ are Gaussian distributed. This transformation can be explained by the Central Limit Theorem, which states that given a sufficiently large sample of the population the distribution of the mean of the sample will converge towards a normal distribution (Kwak and Kim, 2017). The distributions of $\overline{F}_m$ and $\overline{F}_t$ indicate that the most frequent FTLE value has shifted higher, and the smoothing by the average has resulted in fewer negative and high FTLE values.

The standard deviation yields information about the robustness and persistence of LCSs.

This standard deviation is generally larger over time than over ensemble members in Figure 29. This emphasizes the notion that there is higher variability over time than across ensemble members, which is why $\overline{F}_t$ is smoother than $\overline{F}_m$ in Figures 20 and 23.

6 Summary and conclusions

LCSs provide a Lagrangian diagnostic tool for describing the properties of a velocity field. A solid mathematical LCS theory has been built in previous studies, and LCSs have previously been applied practically to understand fluid transport. However, it is well known that the ocean is a chaotic flow system, which has large implications on flow field uncertainty and thus also other Lagrangian methods. Uncertainty should therefore arise in LCSs as well.

Utilizing the FTLE method, I have developed a software for hyperbolic LCS detection. Attracting hyperbolic LCSs have then been computed and their influence on particle trajectories has been investigated, first in a simple analytical system, then in a realistic model. LCSs are known to only be valid for the time interval they are computed over, thus their influence on particle trajectories comes into question given their potentially short lifetime. LCSs are shown to affect particle trajectories in both systems, although having a more immediately apparent influence in the analytical system. The reason for this might be that flow structures, and thus also LCSs, are prone to emerging and disappearing in the realistic model but not in the simple analytical system. Particle trajectories could therefore have been affected by LCSs which existed at previous times.

Averaging over LCSs has been proposed as a method for assessing their robustness and persistence. LCSs are shown to be fairly robust in some parts of the region of study. Specifically, ensemble members predict similar LCSs in locations where the ocean current is steered by coastlines and bottom topography. These robust LCSs are therefore considered to be certain at that particular time. Locations where LCSs are predicted by the ensemble members, but the position and shape of these is uncertain, have also been shown. In such cases, averaging between ensemble members yields large regions where LCSs are more likely to exist.

Due to their time-dependent nature, as well formation and dissipation of flow structures in the turbulent ocean, LCSs have shown to have a smaller degree of persistence. Persistence of LCSs has been investigated in the realistic model over three timescales: daily, monthly and seasonal. A daily variation of LCSs has been shown to occur around the straits in the southern tip of LoVe. This daily LCS variation is periodic and is tightly dependent on the tidal phase. Tides cause tidal pumping through the straits, thus creating specific currents in this location which have large implications on LCSs. No clearly distinguishable monthly persistent LCSs have been detected, although the smooth average indicate that they form frequently along the continental slope, south of Vestfjorden and around the northern and southern tips of LoVe. Finally, it has been shown that large seasonal differences occur. This happens most likely due to differences in current strength, the currents location with regards to the coastline and the amount of bathymetry steering, which is more influential when the vertical water column is weakly stratified. Seasonal and annual persistence should be studied further.

The averaging conducted in this study was able to detect clearly distinguishable robust LCSs, as well as regions where LCSs are frequently form over the ensemble or time. This does not necessarily mean that LCSs are formed in regions indicated by the average at every time step. The smoothed time average makes sense, as LCSs are able to move around with the flow. Therefore it is possible that LCSs persist, but are not clearly distinguishable in the average because they drift. A method for selecting a particular LCS and following its time-evolution should therefore be considered, e.g. a similar criterion method as Dong

et al. (2021). Furthermore, future studies could investigate whether there is a connection between LCS size, shape and lifetime. Their lifetime, as well as distance propagated during the lifetime, could yield important information about LCS spatiotemporal persistence.

LCSs have proved effective at describing material propagation in a simple analytical system. In the turbulent ocean model, material is shown to generally be steered by LCSs as well. LCSs proved to be robust to a certain degree, meaning that models predict LCSs similarly, thus they are certain. However, there exists a multitude of non-robust LCSs as well. As such, LCSs do not circumvent the non-linearity and uncertainty issue, and an EPS should be used for an LCS forecast, similarly to other probabilistic forecasts.

Further studies on the persistence of LCSs are necessary and their evolution over time is uncertain. The accuracy of an LCS forecast is therefore uncertain. However, due to their effect on transport and their robustness, LCSs could be considered as a tool for now-casting, i.e. predicting where material is most likely located right now, when we do not care where it has been or will be in a couple of days. LCS now-casting could therefore prove useful in e.g. locating drifting debris, oil-spill and contamination.

References

Alimi, M., Rhif, A., Rebai, A., Vaidyanathan, S., and Azar, A. T. Chapter 13 - Optimal adaptive backstepping control for chaos synchronization of nonlinear dynamical systems. In Vaidyanathan, S. and Azar, A. T., editors, *Backstepping Control of Nonlinear Dynamical Systems*, Advances in Nonlinear Dynamics and Chaos (ANDC), pages 297–300. Academic Press, January 2021. ISBN 978-0-12-817582-8. doi: 10.1016/B978-0-12-817582-8.00020-9. URL https://www.sciencedirect.com/science/article/pii/B9780128175828000209.

Aurell, E., Boffetta, G., Crisanti, A., Paladin, G., and Vulpiani, A. Predictability in the large: an extension of the concept of Lyapunov exponent. *Journal of Physics A: Mathematical and General*, 30(1):1, January 1997. ISSN 0305-4470. doi: 10.1088/0305-4470/30/1/003. URL https://dx.doi.org/10.1088/0305-4470/30/1/003.

Badza, A., Mattner, T. W., and Balasuriya, S. How sensitive are Lagrangian coherent structures to uncertainties in data? *Physica D: Nonlinear Phenomena*, 444: 133580, February 2023. ISSN 0167-2789. doi: 10.1016/j.physd.2022.133580. URL https://www.sciencedirect.com/science/article/pii/S0167278922002846.

Beron-Vera, F. J., Olascoaga, M. J., Brown, M. G., Koçak, H., and Rypina, I. I. Invariant-tori-like Lagrangian coherent structures in geophysical flows. *Chaos: An Interdisciplinary Journal of Nonlinear Science*, 20(1):017514, March 2010. ISSN 1054-1500. doi: 10.1063/1.3271342. URL https://aip.scitation.org/doi/10.1063/1.3271342. Publisher: American Institute of Physics.

Bettencourt, J. H., López, C., and Hernández-García, E. Oceanic three-dimensional Lagrangian coherent structures: A study of a mesoscale eddy in the Benguela upwelling region. *Ocean Modelling*, 51:73–83, July 2012. ISSN 1463-5003. doi: 10.1016/j.ocemod.2012.04.004. URL https://www.sciencedirect.com/science/article/pii/S1463500312000649.

Blazevski, D. and Haller, G. Hyperbolic and elliptic transport barriers in three-dimensional unsteady flows. *Physica D: Nonlinear Phenomena*, 273-274:46–62, April 2014. ISSN 0167-2789. doi: 10.1016/j.physd.2014.01.007. URL https://www.sciencedirect.com/science/article/pii/S0167278914000165.

Bosse, A., Fer, I., Søiland, H., and Rossby, T. Atlantic Water Transformation Along Its Poleward Pathway Across the Nordic Seas. *Journal of Geophysical Research: Oceans*, 123(9):6428–6448, 2018. ISSN 2169-9291. doi: https://doi.org/10.1029/2018JC014147. URL https://agupubs.onlinelibrary.wiley.com/doi/abs/10.1029/2018JC014147. _eprint: https://agupubs.onlinelibrary.wiley.com/doi/pdf/10.1029/2018JC014147.

Børve, E., Isachsen, P. E., and Nøst, O. A. Rectified tidal transport in Lofoten–Vesterålen, northern Norway. *Ocean Science*, 17(6):1753–1773, December 2021. ISSN 1812-0784. doi: 10.5194/os-17-1753-2021. URL https://os.copernicus.org/articles/17/1753/2021/. Publisher: Copernicus GmbH.

Chen, G. and Han, G. Contrasting Short-Lived With Long-Lived Mesoscale Eddies in the Global Ocean. *Journal of Geophysical Research: Oceans*, 124 (5):3149–3167, 2019. ISSN 2169-9291. doi: 10.1029/2019JC014983. URL

https://onlinelibrary.wiley.com/doi/abs/10.1029/2019JC014983. _eprint: https://onlinelibrary.wiley.com/doi/pdf/10.1029/2019JC014983.

Chenillat, F., Blanke, B., Grima, N., Franks, P. J. S., Capet, X., and Rivière, P. Quantifying tracer dynamics in moving fluids: a combined Eulerian-Lagrangian approach. *Frontiers in Environmental Science*, 3, 2015. ISSN 2296-665X. URL https://www.frontiersin.org/articles/10.3389/fenvs.2015.00043.

Coulliette, C. and Wiggins, S. Intergyre transport in a wind-driven, quasigeostrophic double gyre: An application of lobe dynamics. *Nonlinear Processes in Geophysics*, 7 (1/2):59–85, June 2000. ISSN 1023-5809. doi: 10.5194/npg-7-59-2000. URL https://npg.copernicus.org/articles/7/59/2000/. Publisher: Copernicus GmbH.

Dagestad, K.-F., Röhrs, J., Breivik, , and Ådlandsvik, B. OpenDrift v1.0: a generic framework for trajectory modelling. *Geoscientific Model Development*, 11(4):1405–1420, April 2018. ISSN 1991-959X. doi: 10.5194/gmd-11-1405-2018. URL https://gmd.copernicus.org/articles/11/1405/2018/. Publisher: Copernicus GmbH.

Davis, R. E., Talley, L. D., Roemmich, D., Owens, W. B., Rudnick, D. L., Toole, J., Weller, R., McPhaden, M. J., and Barth, J. A. 100 Years of Progress in Ocean Observing Systems. *Meteorological Monographs*, 59(1):3.1–3.46, January 2019. doi: 10.1175/AMSMONOGRAPHS-D-18-0014.1. URL https://journals.ametsoc.org/view/journals/amsm/59/1/amsmonographs-d-18-0014.1.xml. Publisher: American Meteorological Society Section: Meteorological Monographs.

Dawoodian, M., Sau, A., and Dadvand, A. Paddling motion of a free-swimming jellyfish and Lagrangian coherent structure analysis. *Applied Mathematical Modelling*, 95: 244–278, July 2021. ISSN 0307-904X. doi: 10.1016/j.apm.2020.11.031. URL https://www.sciencedirect.com/science/article/pii/S0307904X20306831.

Dawson, M. N., Gupta, A. S., and England, M. H. Coupled biophysical global ocean model and molecular genetic analyses identify multiple introductions of cryptogenic species. *Proceedings of the National Academy of Sciences*, 102(34):11968–11973, August 2005. doi: 10.1073/pnas.0503811102. URL https://www.pnas.org/doi/abs/10.1073/pnas.0503811102. Publisher: Proceedings of the National Academy of Sciences.

Dingwell, J. B. Lyapunov Exponents. In *Wiley Encyclopedia of Biomedical Engineering*. John Wiley & Sons, Ltd, 2006. ISBN 978-0-471-74036-0. doi: 10.1002/9780471740360.ebs0702. URL https://onlinelibrary.wiley.com/doi/abs/10.1002/9780471740360.ebs0702. _eprint: https://onlinelibrary.wiley.com/doi/pdf/10.1002/9780471740360.ebs0702.

Dong, H., Zhou, M., Hu, Z., Zhang, Z., Zhong, Y., Basedow, S. L., and Smith Jr., W. O. Transport Barriers and the Retention of Calanus finmarchicus on the Lofoten Shelf in Early Spring. *Journal of Geophysical Research: Oceans*, 126(8):e2021JC017408, 2021. ISSN 2169-9291. doi: 10.1029/2021JC017408. URL https://onlinelibrary.wiley.com/doi/abs/10.1029/2021JC017408. _eprint: https://onlinelibrary.wiley.com/doi/pdf/10.1029/2021JC017408.

Duarte, P., Brændshøi, J., Shcherbin, D., Barras, P., Albretsen, J., Gusdal, Y., Szapiro, N., Martinsen, A., Samuelsen, A., Wang, K., and Debernard, J. B. Implementation and evaluation of open boundary conditions for sea ice in a regional coupled ocean (ROMS)

and sea ice (CICE) modeling system. *Geoscientific Model Development*, 15(11):4373–4392, June 2022. ISSN 1991-959X. doi: 10.5194/gmd-15-4373-2022. URL https://gmd.copernicus.org/articles/15/4373/2022/. Publisher: Copernicus GmbH.

Evensen, G. Inverse methods and data assimilation in nonlinear ocean models. *Physica D: Nonlinear Phenomena*, 77(1):108–129, October 1994. ISSN 0167-2789. doi: 10.1016/0167-2789(94)90130-9. URL https://www.sciencedirect.com/science/article/pii/0167278994901309.

Farazmand, M. and Haller, G. Computing Lagrangian coherent structures from their variational theory. *Chaos: An Interdisciplinary Journal of Nonlinear Science*, 22 (1):013128, March 2012. ISSN 1054-1500. doi: 10.1063/1.3690153. URL https://aip.scitation.org/doi/full/10.1063/1.3690153. Publisher: American Institute of Physics.

Fox-Kemper, B., Adcroft, A., Böning, C. W., Chassignet, E. P., Curchitser, E., Danabasoglu, G., Eden, C., England, M. H., Gerdes, R., Greatbatch, R. J., Griffies, S. M., Hallberg, R. W., Hanert, E., Heimbach, P., Hewitt, H. T., Hill, C. N., Komuro, Y., Legg, S., Le Sommer, J., Masina, S., Marsland, S. J., Penny, S. G., Qiao, F., Ringler, T. D., Treguier, A. M., Tsujino, H., Uotila, P., and Yeager, S. G. Challenges and Prospects in Ocean Circulation Models. *Frontiers in Marine Science*, 6, 2019. ISSN 2296-7745. URL https://www.frontiersin.org/articles/10.3389/fmars.2019.00065.

Fritzner, S. M., Graversen, R. G., Wang, K., and Christensen, K. H. Comparison between a multi-variate nudging method and the ensemble Kalman filter for sea-ice data assimilation. *Journal of Glaciology*, 64(245):387–396, June 2018. ISSN 0022-1430, 1727-5652. doi: 10.1017/jog.2018.33. URL https://www.cambridge.org/core/journals/journal-of-glaciology/article/comparison-between-a-multivariate-nudging-method-and-the-ensemble-kalman-filter-for-seaice-data-assimilation/6B5BAE0A22A5828F22402EDC7D3AC44A. Publisher: Cambridge University Press.

Froyland, G. and Padberg-Gehle, K. Finite-time entropy: A probabilistic approach for measuring nonlinear stretching. *Physica D: Nonlinear Phenomena*, 241(19):1612–1628, October 2012. ISSN 0167-2789. doi: 10.1016/j.physd.2012.06.010. URL https://www.sciencedirect.com/science/article/pii/S0167278912001741.

Fuchs, R., Schindler, B., and Peikert, R. Scale-Space Approaches to FTLE Ridges. In Peikert, R., Hauser, H., Carr, H., and Fuchs, R., editors, *Topological Methods in Data Analysis and Visualization II: Theory, Algorithms, and Applications*, Mathematics and Visualization, pages 283–296. Springer, Berlin, Heidelberg, 2012. ISBN 978-3-642-23175-9. doi: 10.1007/978-3-642-23175-9_19. URL https://doi.org/10.1007/978-3-642-23175-9_19.

Gascard, J.-C., Raisbeck, G., Sequeira, S., Yiou, F., and Mork, K. A. The Norwegian Atlantic Current in the Lofoten basin inferred from hydrological and tracer data (129I) and its interaction with the Norwegian Coastal Current. *Geophysical Research Letters*, 31(1), 2004. ISSN 1944-8007. doi: https://doi.org/10.1029/2003GL018303. URL https://agupubs.pericles-prod.literatumonline.com/doi/abs/10.1029/2003GL018303. _eprint: https://agupubs.onlinelibrary.wiley.com/doi/pdf/10.1029/2003GL018303.

Ghosh, A., Suara, K., McCue, S. W., and Brown, R. J. Sensitivity and robustness of Lagrangian coherent structures in coastal water systems. *Environmental Fluid Mechanics*, 21(3):667–691, June 2021. ISSN 1573-1510. doi: 10.1007/s10652-021-09792-8. URL https://doi.org/10.1007/s10652-021-09792-8.

Gille, S., Metzger, J., and Tokmakian, R. Seafloor Topography and Ocean Circulation. *Oceanography*, 17(1):47–54, March 2004. ISSN 10428275. doi: 10.5670/oceanog.2004.66. URL https://tos.org/oceanography/article/seafloor-topography-and-ocean-circulation.

Hadjighasem, A. and Haller, G. Geodesic Transport Barriers in Jupiter's Atmosphere: A Video-Based Analysis. *SIAM Review*, 58(1):69–89, January 2016. ISSN 0036-1445. doi: 10.1137/140983665. URL https://epubs.siam.org/doi/10.1137/140983665. Publisher: Society for Industrial and Applied Mathematics.

Haller, G. Distinguished material surfaces and coherent structures in three-dimensional fluid flows. *Physica D: Nonlinear Phenomena*, 149(4):248–277, March 2001. ISSN 0167-2789. doi: 10.1016/S0167-2789(00)00199-8. URL https://www.sciencedirect.com/science/article/pii/S0167278900001998.

Haller, G. and Yuan, G. Lagrangian coherent structures and mixing in two-dimensional turbulence. *Physica D: Nonlinear Phenomena*, 147(3):352–370, December 2000. ISSN 0167-2789. doi: 10.1016/S0167-2789(00)00142-1. URL https://www.sciencedirect.com/science/article/pii/S0167278900001421.

Haller, G. A variational theory of hyperbolic Lagrangian Coherent Structures. *Physica D: Nonlinear Phenomena*, 240(7):574–598, March 2011. ISSN 0167-2789. doi: 10.1016/j.physd.2010.11.010. URL https://www.sciencedirect.com/science/article/pii/S0167278910003143.

Haller, G. Lagrangian Coherent Structures. *Annual Review of Fluid Mechanics*, 47:137–162, January 2015. ISSN 0066-4189. doi: 10.1146/annurev-fluid-010313-141322. URL https://ui.adsabs.harvard.edu/abs/2015AnRFM..47..137H. ADS Bibcode: 2015AnRFM..47..137H.

Haller, G. and Sapsis, T. Lagrangian coherent structures and the smallest finite-time Lyapunov exponent. *Chaos: An Interdisciplinary Journal of Nonlinear Science*, 21(2):023115, June 2011. ISSN 1054-1500. doi: 10.1063/1.3579597. URL https://aip.scitation.org/doi/10.1063/1.3579597. Publisher: American Institute of Physics.

Harris, C. R., Millman, K. J., van der Walt, S. J., Gommers, R., Virtanen, P., Cournapeau, D., Wieser, E., Taylor, J., Berg, S., Smith, N. J., Kern, R., Picus, M., Hoyer, S., van Kerkwijk, M. H., Brett, M., Haldane, A., del Río, J. F., Wiebe, M., Peterson, P., Gérard-Marchant, P., Sheppard, K., Reddy, T., Weckesser, W., Abbasi, H., Gohlke, C., and Oliphant, T. E. Array programming with NumPy. *Nature*, 585(7825):357–362, September 2020. ISSN 1476-4687. doi: 10.1038/s41586-020-2649-2. URL https://www.nature.com/articles/s41586-020-2649-2. Number: 7825 Publisher: Nature Publishing Group.

Hjorth-Jensen, M. Partial Differential Equations. In *Computational Physics*, pages 243–270. Department of Physics, University of Oslo, Oslo, 2015. URL https://raw.githubusercontent.com/CompPhysics/ComputationalPhysics/master/doc/Lectures/lectures2015.pdf.

Idžanović, M., Rikardsen, E., and Röhrs, J. Forecast Uncertainty and Ensemble Spread in Surface Currents from a Regional Ocean Model. *In review for Frontiers in Marine Science*, 2023.

Isachsen, P. E. Baroclinic instability and the mesoscale eddy field around the Lofoten Basin. *Journal of Geophysical Research: Oceans*, 120(4): 2884–2903, 2015. ISSN 2169-9291. doi: 10.1002/2014JC010448. URL https://onlinelibrary.wiley.com/doi/abs/10.1002/2014JC010448. _eprint: https://onlinelibrary.wiley.com/doi/pdf/10.1002/2014JC010448.

Joseph, B. and Legras, B. Relation between Kinematic Boundaries, Stirring, and Barriers for the Antarctic Polar Vortex. *Journal of the Atmospheric Sciences*, 59(7):1198–1212, April 2002. ISSN 0022-4928, 1520-0469. doi: 10.1175/1520-0469(2002)059<1198:RBKBSA>2.0.CO;2. URL https://journals.ametsoc.org/view/journals/atsc/59/7/1520-0469_2002_059_1198_rbkbsa_2.0.co_2.xml. Publisher: American Meteorological Society Section: Journal of the Atmospheric Sciences.

Karrasch, D. and Haller, G. Do Finite-Size Lyapunov Exponents detect coherent structures? *Chaos: An Interdisciplinary Journal of Nonlinear Science*, 23(4):043126, December 2013. ISSN 1054-1500. doi: 10.1063/1.4837075. URL https://aip.scitation.org/doi/10.1063/1.4837075. Publisher: American Institute of Physics.

Koszalka, I., LaCasce, J. H., and Mauritzen, C. In pursuit of anomalies—Analyzing the poleward transport of Atlantic Water with surface drifters. *Deep Sea Research Part II: Topical Studies in Oceanography*, 85:96–108, January 2013. ISSN 0967-0645. doi: 10.1016/j.dsr2.2012.07.035. URL https://www.sciencedirect.com/science/article/pii/S096706451200121X.

Kwak, S. G. and Kim, J. H. Central limit theorem: the cornerstone of modern statistics. *Korean Journal of Anesthesiology*, 70(2):144–156, April 2017. ISSN 2005-6419. doi: 10.4097/kjae.2017.70.2.144. URL https://www.ncbi.nlm.nih.gov/pmc/articles/PMC5370305/.

Lekien, F., Coulliette, C., Mariano, A. J., Ryan, E. H., Shay, L. K., Haller, G., and Marsden, J. Pollution release tied to invariant manifolds: A case study for the coast of Florida. *Physica D: Nonlinear Phenomena*, 210(1):1–20, October 2005. ISSN 0167-2789. doi: 10.1016/j.physd.2005.06.023. URL https://www.sciencedirect.com/science/article/pii/S0167278905002502.

Leutbecher, M. Ensemble forecasting, 2007. URL https://www.ecmwf.int/en/elibrary/75394-ensemble-forecasting.

Marsh, R., Ivchenko, V. O., Skliris, N., Alderson, S., Bigg, G. R., Madec, G., Blaker, A. T., Aksenov, Y., Sinha, B., Coward, A. C., Le Sommer, J., Merino, N., and Zalesny, V. B. NEMO–ICB (v1.0): interactive icebergs in the NEMO ocean model globally configured at eddy-permitting resolution. *Geoscientific Model Development*, 8(5):1547–1562, May 2015. ISSN 1991-959X. doi: 10.5194/gmd-8-1547-2015. URL https://gmd.copernicus.org/articles/8/1547/2015/. Publisher: Copernicus GmbH.

Mitchelson-Jacob, G. and Sundby, S. Eddies of Vestfjorden, Norway. *Continental Shelf Research*, 21(16-17):1901–1918, November 2001. ISSN 0278-4343. doi: 10.1016/S0278-4343(01)00030-9. URL https://linkinghub.elsevier.com/retrieve/pii/S0278434301000309. Place: Oxford Publisher: Pergamon-Elsevier Science Ltd WOS:000172425900009.

Moe, H., Ommundsen, A., and Gjevik, B. A high resolution tidal model for the area around The Lofoten Islands, northern Norway. *Continental Shelf Research*, 22(3):485–504, February 2002. ISSN 0278-4343. doi: 10.1016/S0278-4343(01)00078-4. URL https://linkinghub.elsevier.com/retrieve/pii/S0278434301000784. Place: Oxford Publisher: Pergamon-Elsevier Science Ltd WOS:000174555500007.

Müller, M., Homleid, M., Ivarsson, K.-I., Køltzow, M. A. , Lindskog, M., Midtbø, K. H., Andrae, U., Aspelien, T., Berggren, L., Bjørge, D., Dahlgren, P., Kristiansen, J., Randriamampianina, R., Ridal, M., and Vignes, O. AROME-MetCoOp: A Nordic Convective-Scale Operational Weather Prediction Model. *Weather and Forecasting*, 32(2):609–627, April 2017. ISSN 1520-0434, 0882-8156. doi: 10.1175/WAF-D-16-0099.1. URL https://journals.ametsoc.org/view/journals/wefo/32/2/waf-d-16-0099_1.xml. Publisher: American Meteorological Society Section: Weather and Forecasting.

Nordam, T., Nepstad, R., Litzler, E., and Röhrs, J. On the use of random walk schemes in oil spill modelling. *Marine Pollution Bulletin*, 146:631–638, September 2019. ISSN 0025-326X. doi: 10.1016/j.marpolbul.2019.07.002. URL https://www.sciencedirect.com/science/article/pii/S0025326X19305338.

Nøst, O. A. and Børve, E. Flow separation, dipole formation, and water exchange through tidal straits. *Ocean Science*, 17(5):1403–1420, October 2021. ISSN 1812-0784. doi: 10.5194/os-17-1403-2021. URL https://os.copernicus.org/articles/17/1403/2021/. Publisher: Copernicus GmbH.

Paris, C. B., Cowen, R. K., Claro, R., and Lindeman, K. C. Larval transport pathways from Cuban snapper (Lutjanidae) spawning aggregations based on biophysical modeling. *Marine Ecology Progress Series*, 296:93–106, July 2005. ISSN 0171-8630, 1616-1599. doi: 10.3354/meps296093. URL https://www.int-res.com/abstracts/meps/v296/p93-106/.

Parker, W. S. Reanalyses and Observations: What's the Difference? *Bulletin of the American Meteorological Society*, 97(9):1565–1572, September 2016. ISSN 0003-0007, 1520-0477. doi: 10.1175/BAMS-D-14-00226.1. URL https://journals.ametsoc.org/view/journals/bams/97/9/bams-d-14-00226.1.xml. Publisher: American Meteorological Society Section: Bulletin of the American Meteorological Society.

Peacock, T. and Haller, G. Lagrangian coherent structures: The hidden skeleton of fluid flows. *Physics Today*, 66(2):41–47, February 2013. ISSN 0031-9228. doi: 10.1063/PT.3.1886. URL https://physicstoday.scitation.org/doi/10.1063/PT.3.1886. Publisher: American Institute of Physics.

Pierrehumbert, R. T. and Yang, H. Global Chaotic Mixing on Isentropic Surfaces. *Journal of the Atmospheric Sciences*, 50(15):2462–2480, August 1993. ISSN 0022-4928, 1520-0469. doi: 10.1175/1520-0469(1993)050<2462:GCMOIS>2.0.CO;2. URL https://journals.ametsoc.org/view/journals/atsc/50/15/1520-0469_1993_050_2462_gcmois_2_0_co_2.xml. Publisher: American Meteorological Society Section: Journal of the Atmospheric Sciences.

Rosenstein, M. T., Collins, J. J., and De Luca, C. J. A practical method for calculating largest Lyapunov exponents from small data sets. *Physica D: Nonlinear Phenomena*, 65(1):117–134, May 1993. ISSN 0167-2789. doi: 10.1016/0167-2789(93)90009-P. URL https://www.sciencedirect.com/science/article/pii/016727899390009P.

Rossby, T., Ozhigin, V., Ivshin, V., and Bacon, S. An isopycnal view of the Nordic Seas hydrography with focus on properties of the Lofoten Basin. *Deep Sea Research Part I: Oceanographic Research Papers*, 56(11):1955–1971, November 2009. ISSN 0967-0637. doi: 10.1016/j.dsr.2009.07.005. URL https://www.sciencedirect.com/science/article/pii/S096706370900154X.

Roy-Barman, M. and Jeandel, C. Advection–Diffusion Models. In Roy-Barman, M. and Jeandel, C., editors, *Marine Geochemistry: Ocean Circulation, Carbon Cycle and Climate Change*, page 0. Oxford University Press, September 2016. ISBN 978-0-19-878749-5. doi: 10.1093/acprof:oso/9780198787495.003.0006. URL https://doi.org/10.1093/acprof:oso/9780198787495.003.0006.

Röhrs, J., Christensen, K. H., Vikebø, F., Sundby, S., Saetra, , and Broström, G. Wave-induced transport and vertical mixing of pelagic eggs and larvae. *Limnology and Oceanography*, 59(4):1213–1227, 2014. ISSN 1939-5590. doi: 10.4319/lo.2014.59.4.1213. URL https://onlinelibrary.wiley.com/doi/abs/10.4319/lo.2014.59.4.1213. _eprint: https://onlinelibrary.wiley.com/doi/pdf/10.4319/lo.2014.59.4.1213.

Röhrs, J., Gusdal, Y., Rikardsen, E., Duran Moro, M., Brændshøi, J., Kristensen, N. M., Fritzner, S., Wang, K., Sperrevik, A. K., Idžanović, M., Lavergne, T., Debernard, J., and Christensen, K. H. Barents-2.5km v2.0: An operational data-assimilative coupled ocean and sea ice ensemble prediction model for the Barents Sea and Svalbard. *Geoscientific Model Development Discussions*, pages 1–31, March 2023. doi: 10.5194/gmd-2023-20. URL https://gmd.copernicus.org/preprints/gmd-2023-20/. Publisher: Copernicus GmbH.

Shadden, S. C. and Taylor, C. A. Characterization of Coherent Structures in the Cardiovascular System. *Annals of Biomedical Engineering*, 36(7):1152–1162, July 2008. ISSN 1573-9686. doi: 10.1007/s10439-008-9502-3. URL https://doi.org/10.1007/s10439-008-9502-3.

Shadden, S. C., Lekien, F., and Marsden, J. E. Definition and properties of Lagrangian coherent structures from finite-time Lyapunov exponents in two-dimensional aperiodic flows. *Physica D: Nonlinear Phenomena*, 212(3):271–304, December 2005. ISSN 0167-2789. doi: 10.1016/j.physd.2005.10.007. URL https://www.sciencedirect.com/science/article/pii/S0167278905004446.

Stevens, J. and Dauphin, S. Summer blooms in the Baltic, June 2018. URL https://climate.nasa.gov/climate_resources/170/summer-blooms-in-the-baltic.

Strogatz, S. H. In *Nonlinear Dynamics and Chaos: With Applications to Physics, Biology, Chemistry, and Engineering*, pages 320–322. CRC Press, Boca Raton, 2 edition, May 2019. ISBN 978-0-429-49256-3. doi: 10.1201/9780429492563.

Sundby, S. Influence of bottom topography on the circulation at the continental shelf off northern Norway. 1984. Publisher: [Fiskeridirektoratets havforskningsinstitutt].

Sundby, S., Fossum, P., Sandvik, A. D., Vikebø, F., Aglen, A., Buhl-Mortensen, L., Folkvord, A., Bakkeplass, K., Buhl-Mortensen, P., Johannessen, M., Jørgensen, M. S., Kristiansen, T., Landra, C. S., Myksvoll, M. S., and Nash, R. D. M. KunnskapsInnhenting Barentshavet–Lofoten–Vesterålen (KILO). *188 s.*, March 2013. ISSN 0071-5638. URL https://imr.brage.unit.no/imr-xmlui/handle/11250/113923. Accepted: 2013-04-12T07:54:52Z Publisher: Havforskningsinstituttet.

Søiland, H. and Rossby, T. On the structure of the Lofoten Basin Eddy. *Journal of Geophysical Research: Oceans*, 118(9):4201–4212, 2013. ISSN 2169-9291. doi: 10.1002/jgrc.20301. URL https://onlinelibrary.wiley.com/doi/abs/10.1002/jgrc.20301. _eprint: https://onlinelibrary.wiley.com/doi/pdf/10.1002/jgrc.20301.

Trodahl, M. and Isachsen, P. E. Topographic Influence on Baroclinic Instability and the Mesoscale Eddy Field in the Northern North Atlantic Ocean and the Nordic Seas. *Journal of Physical Oceanography*, 48(11):2593–2607, November 2018. ISSN 0022-3670, 1520-0485. doi: 10.1175/JPO-D-17-0220.1. URL https://journals.ametsoc.org/view/journals/phoc/48/11/jpo-d-17-0220.1.xml. Publisher: American Meteorological Society Section: Journal of Physical Oceanography.

Truesdell, C. and Noll, W. The Non-Linear Field Theories of Mechanics. In Truesdell, C., Noll, W., and Antman, S. S., editors, *The Non-Linear Field Theories of Mechanics*, pages 57–73. Springer, Berlin, Heidelberg, 2004. ISBN 978-3-662-10388-3. doi: 10.1007/978-3-662-10388-3_1. URL https://doi.org/10.1007/978-3-662-10388-3_1.

US EPA, O. Deepwater Horizon – BP Gulf of Mexico Oil Spill, September 2013. URL https://www.epa.gov/enforcement/deepwater-horizon-bp-gulf-mexico-oil-spill.

van Sebille, E., Griffies, S. M., Abernathey, R., Adams, T. P., Berloff, P., Biastoch, A., Blanke, B., Chassignet, E. P., Cheng, Y., Cotter, C. J., Deleersnijder, E., Döös, K., Drake, H. F., Drijfhout, S., Gary, S. F., Heemink, A. W., Kjellsson, J., Koszalka, I. M., Lange, M., Lique, C., MacGilchrist, G. A., Marsh, R., Mayorga Adame, C. G., McAdam, R., Nencioli, F., Paris, C. B., Piggott, M. D., Polton, J. A., Rühs, S., Shah, S. H. A. M., Thomas, M. D., Wang, J., Wolfram, P. J., Zanna, L., and Zika, J. D. Lagrangian ocean analysis: Fundamentals and practices. *Ocean Modelling*, 121:49–75, January 2018. ISSN 1463-5003. doi: 10.1016/j.ocemod.2017.11.008. URL https://www.sciencedirect.com/science/article/pii/S1463500317301853.

A Appendix A: Double-Gyre

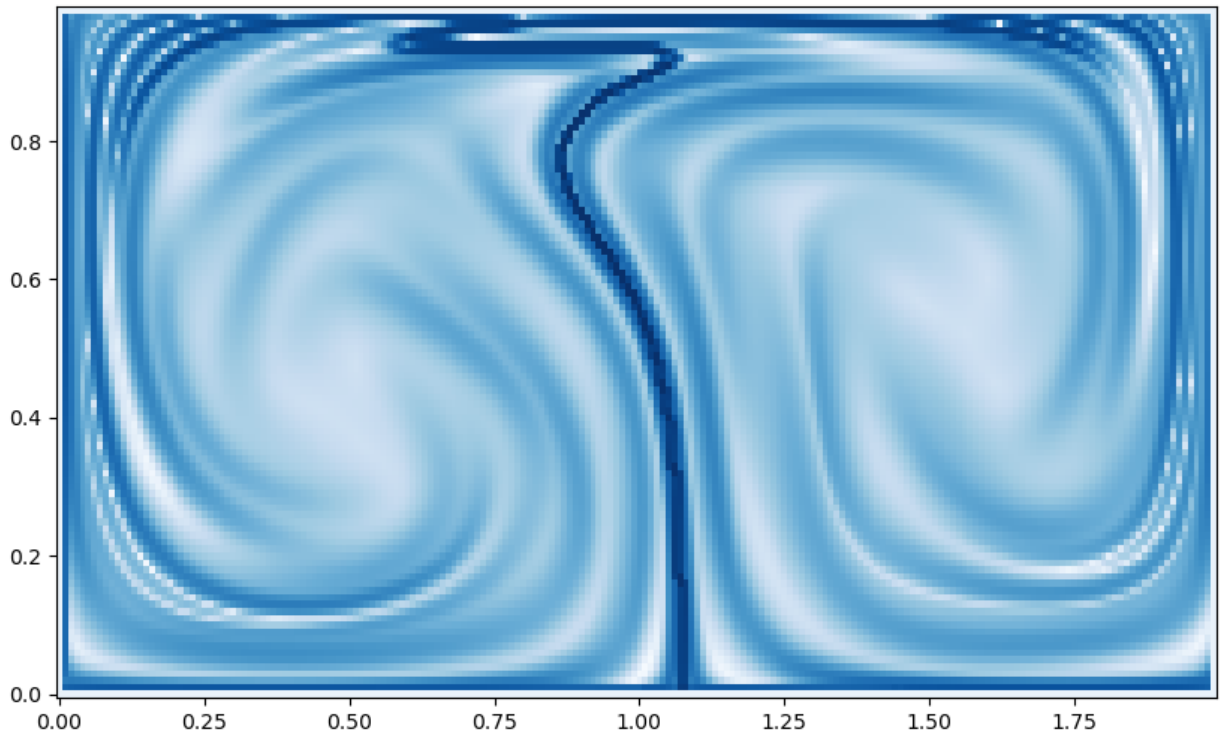

Figure 30: Repelling hyperbolic LCSs in double-gyre system. Computed for $t = 0$ over a time interval $T = 5$, with parameters $A = 0.25$, $\epsilon = 0.25$ and $\omega = 2\pi$

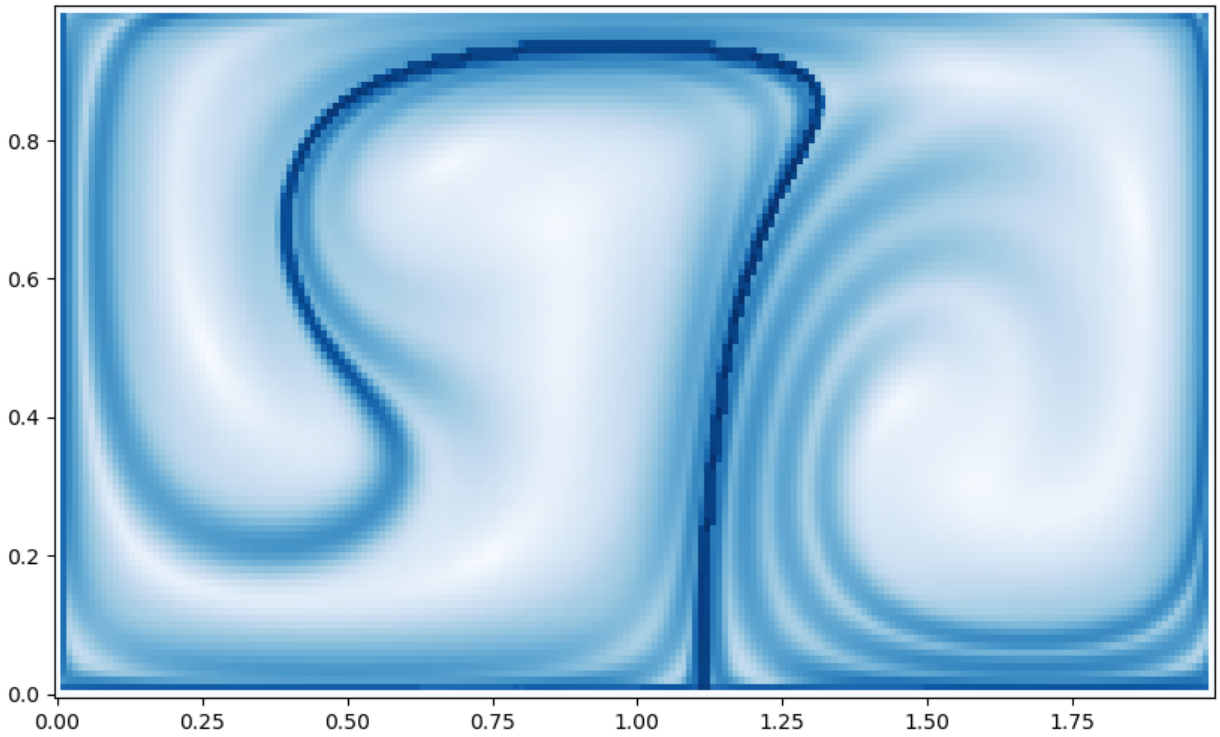

Figure 31: Repelling hyperbolic LCSs in double-gyre system. Computed for $t = 0$ over a time interval $T = 10$, with parameters $A = 0.1$, $\epsilon = 0.25$ and $\omega = 2\pi/10$.

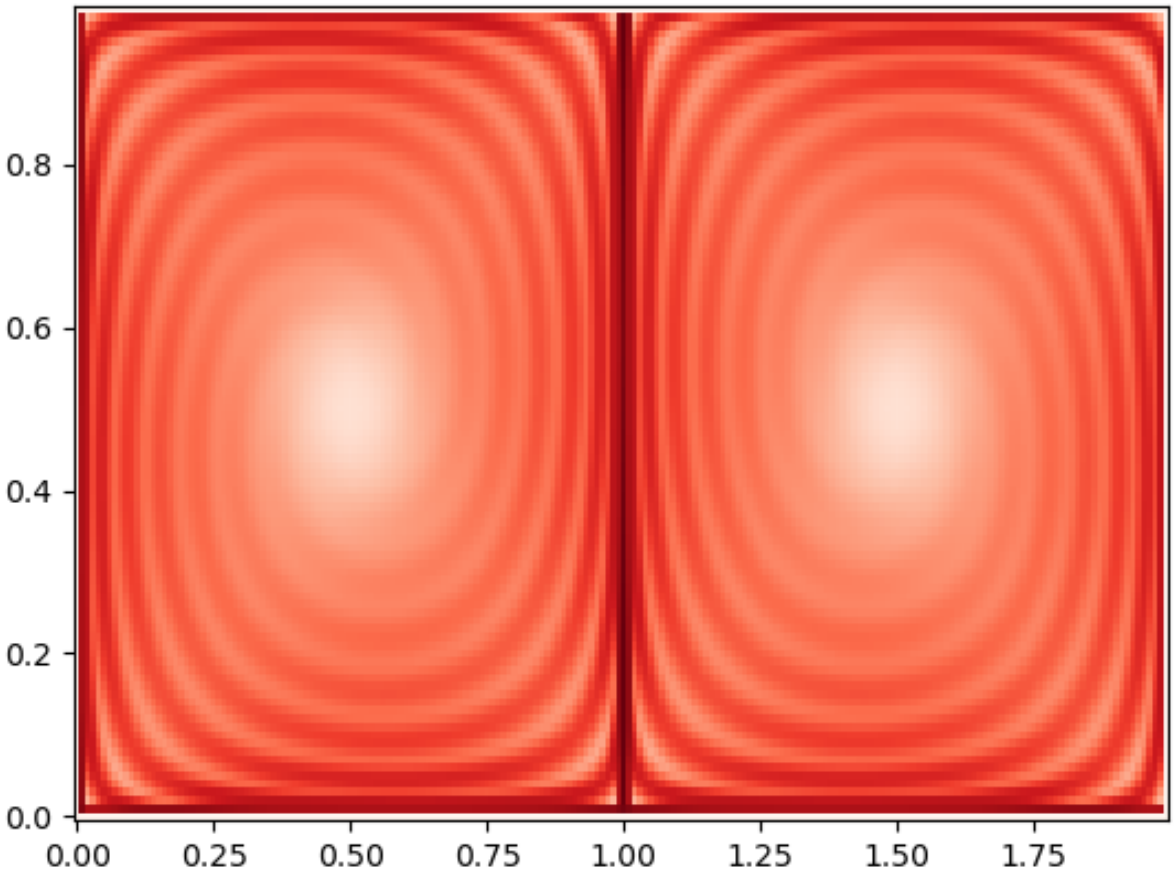

Figure 32: Attracting hyperbolic LCSs in time-independent double-gyre system, with $\epsilon = 0$.

B Appendix B: Barents-2.5 EPS

B.1 Tidal effect

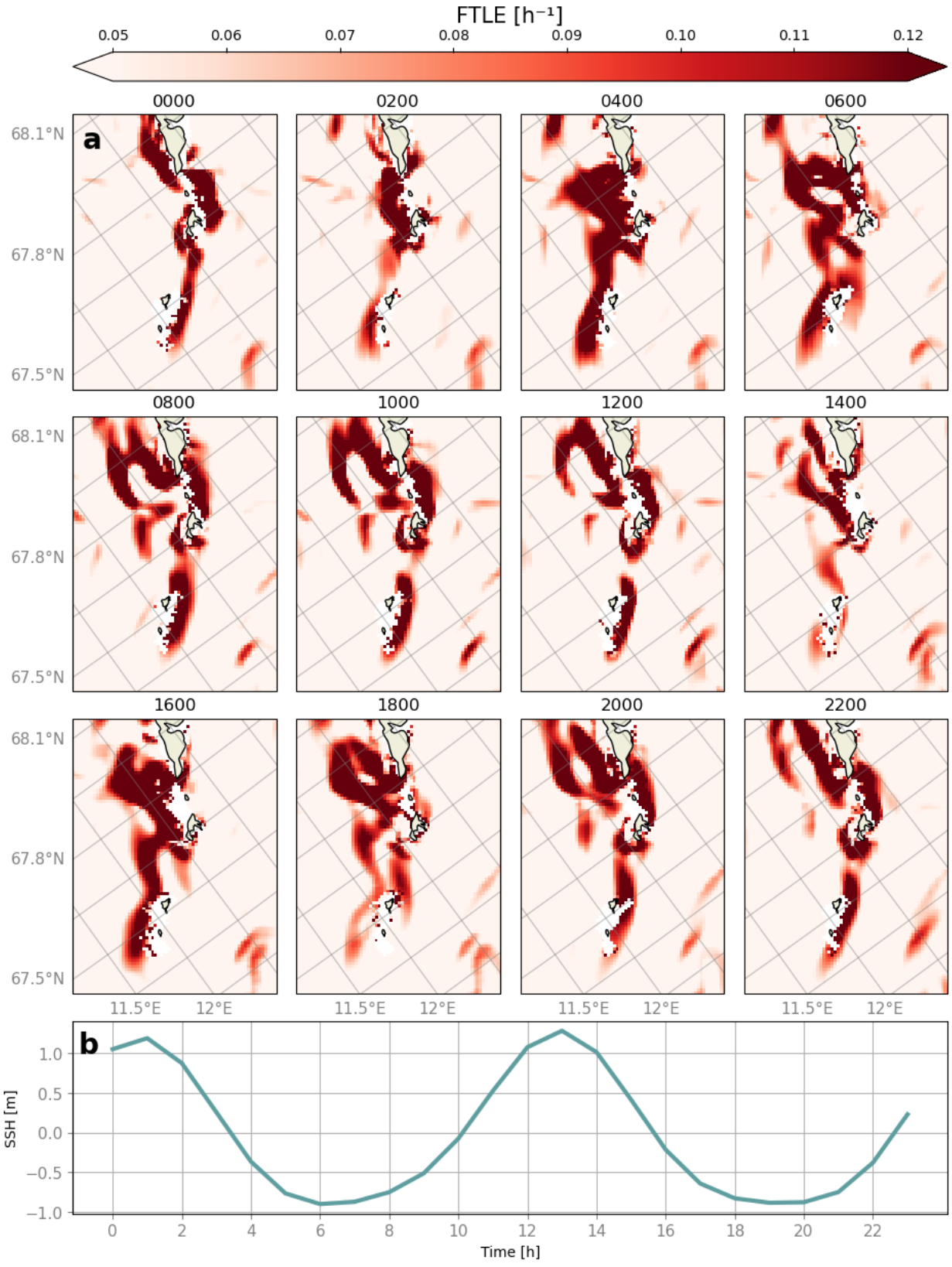

Figure 33: Daily variability of LCSs around the southern tip of LoVe for member 2.

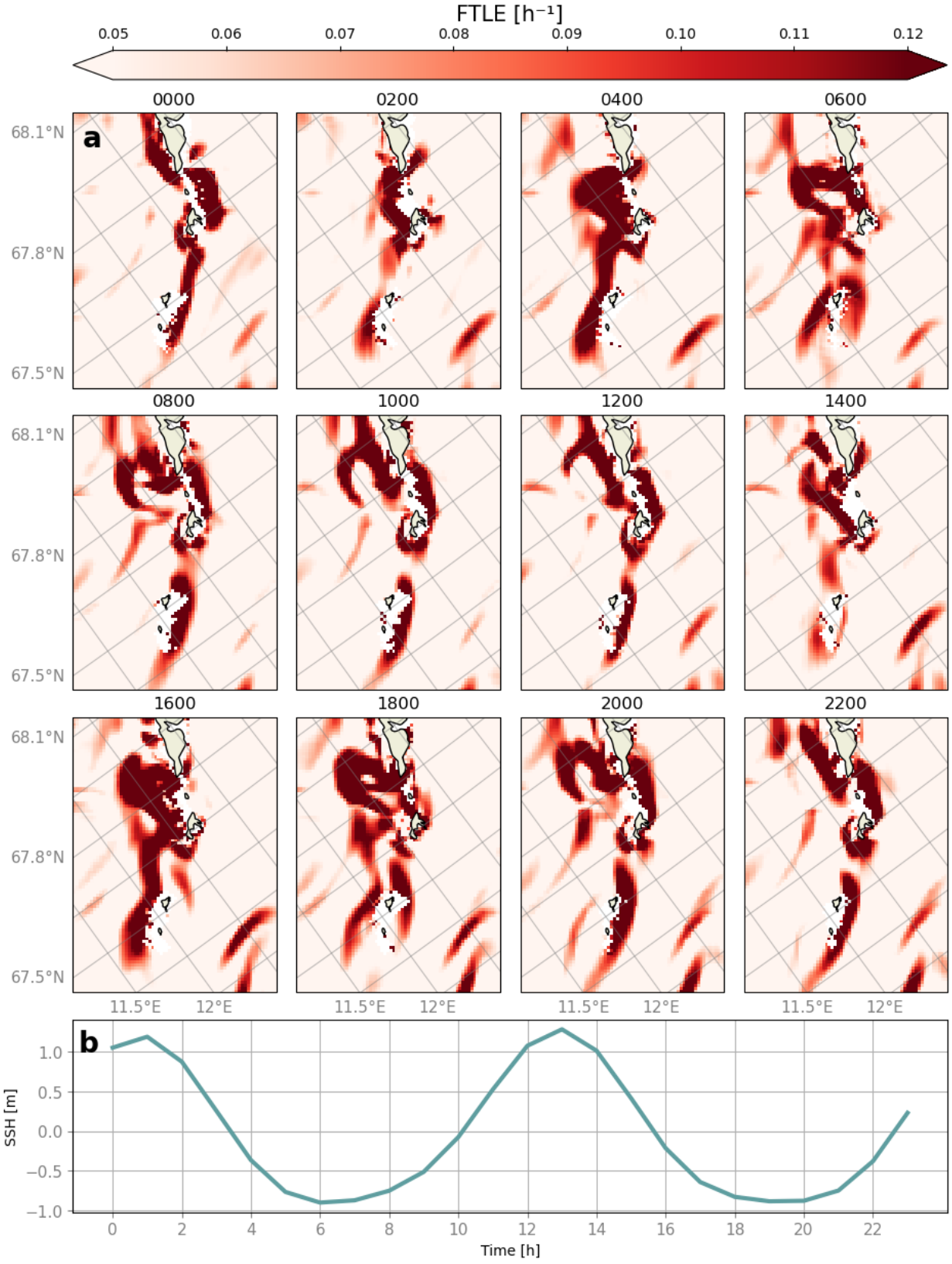

Figure 34: Daily variability of LCSs around the southern tip of LoVe for member 3.

B.2 Attracting hyperbolic LCSs for October

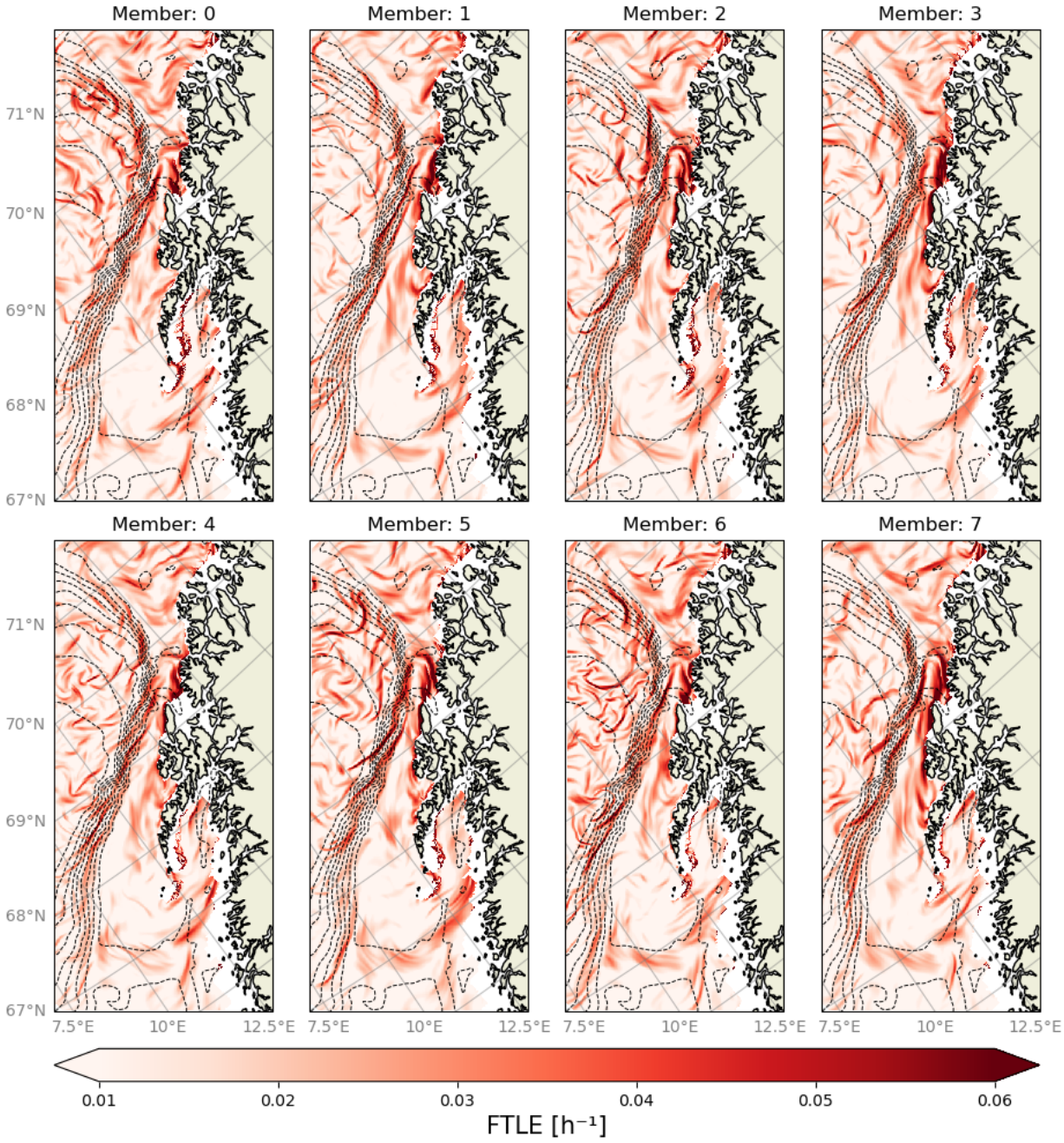

Figure 35: Attracting LCSs for October 6. 2022 using velocity fields from the eight first members of the Barents-2.5 EPS.

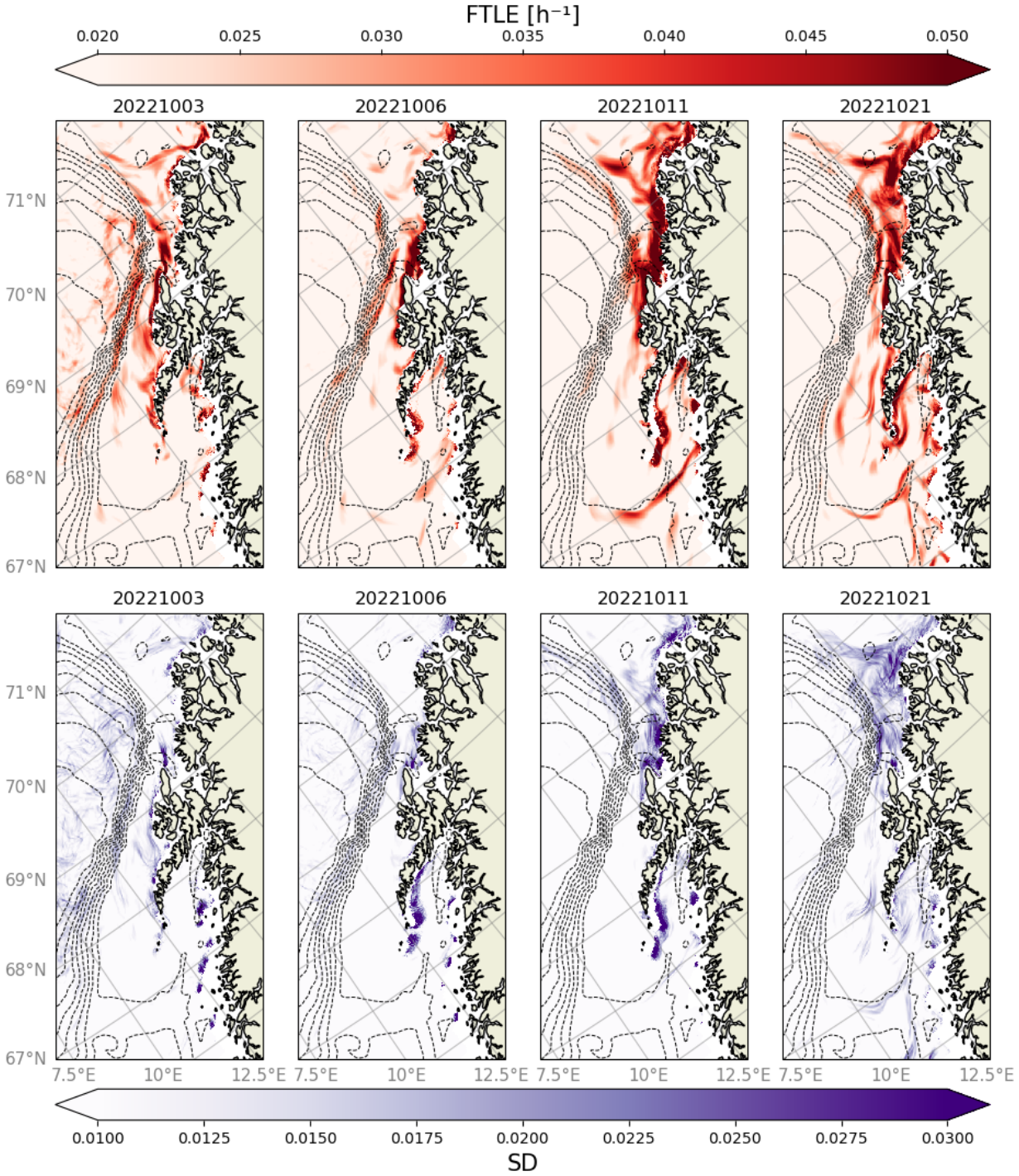

Figure 36: $\overline{F}_m$ for four dates in October 2022, and corresponding σ_{F_m}.

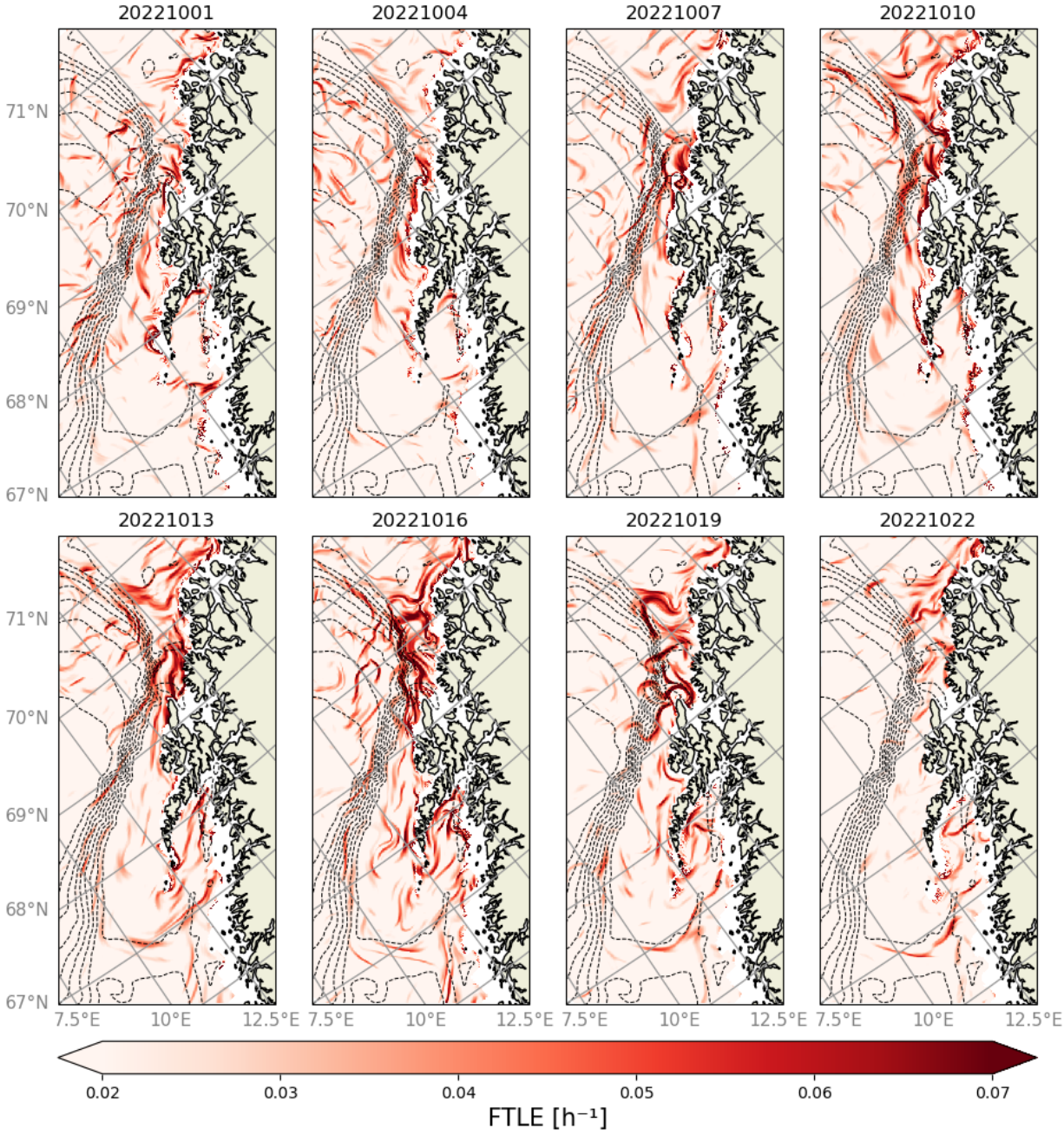

Figure 37: Attracting LCSs for eight dates for member 0 of the Barents-2.5 EPS for October.

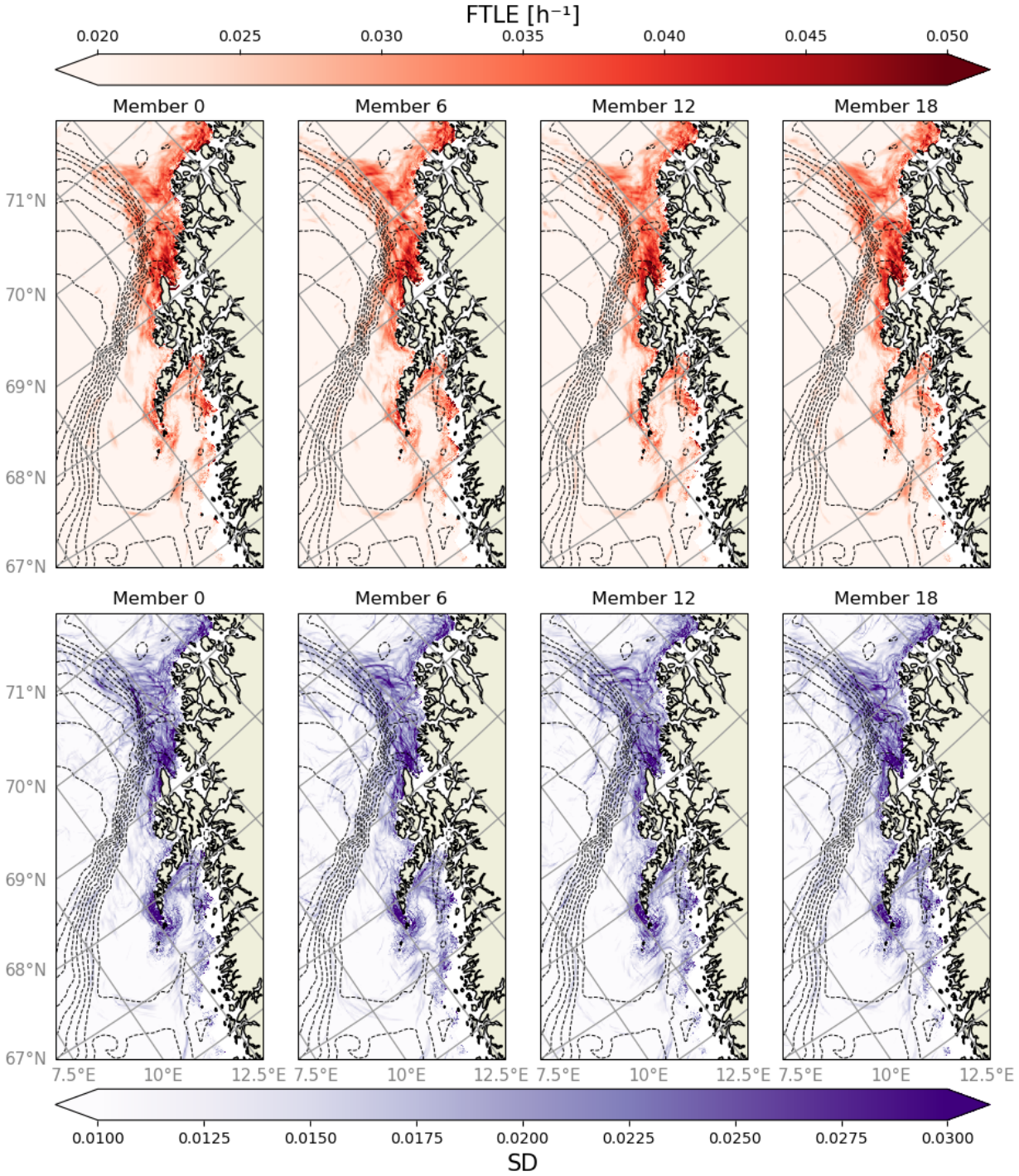

Figure 38: $\overline{F}_t$ over October for four members in the Barents-2.5 EPS, and corresponding σ_{F_t}.

C Appendix C: GitHub Link

The software developed for computing LCSs in this thesis is available on https://github.com/mateuszmatu/LCS.

D Parabolic and Elliptic LCSs

Parabolic LCSs in atmosphere of Jupiter: https://epubs.siam.org/doi/suppl/10.1137/140983665/suppl_file/chevron_movie.mov

Elliptic LCSs in atmosphere of Jupiter: https://epubs.siam.org/doi/suppl/10.1137/140983665/suppl_file/grs_movie.mov

Both LCSs computed and videos created by Hadjighasem and Haller (2016).